THE UNIVERSITY
of EDINBURGH

Shaping drops with magnetic fields

Jennifer Dodoo

The University of Edinburgh

School of Engineering

Institute for Integrated Micro and Nano Systems

The Centre for Doctoral Training

Intelligent Sensing and Measurement

Supervised by:

Adam A. Stokes

A Thesis Submitted for the Degree of

Doctor of Philosophy

2019

Lay Summary of Thesis

The lay summary is a brief summary intended to facilitate knowledge transfer and enhance accessibility, therefore the language used should be non-technical and suitable for a general audience. (See the Degree Regulations and Programmes of Study, General Postgraduate Degree Programme Regulations. These regulations are available via: www.drps.ed.ac.uk.)

Name of student:	Jennifer Dodoo		UUN	S1576937
University email:	j.dodoo@ed.ac.uk			
Degree sought:	Doctor of Philosophy	No. of words in the main text of thesis:	45000	
Title of thesis:	Shaping drops with magnetic fields			

Drops, or small volumes of liquids, are important in our everyday life. From rain drops, that soak through our waterproof coats after too many uses; over blood drops, that a person suffering from diabetes extracts from their finger to measure their blood sugar level with a point-of-care test; to inkjet printing, where drops of print are ejected by a printer nozzle onto a sheet of paper. Covering such a wide range of everyday and industrial problems, it is understandable that much research goes into understanding and controlling drops. There are many opportunities to further develop the applications of drops, such as in medical and food research.

A common technique to control drops uses electric fields that change the shape of a drop or even move the drop. Electric fields are generated by an electric power source, such as a battery or a voltage supply. These power sources can be miniaturised and built into point-of-care tests and printers, where they control drops of blood or ink.

While electric control techniques are widely used to solve some challenges, there are cases where a different approach, such as the use of magnetic fields, is required. Magnetic fields are generated by a permanent magnet, such as a horseshoe or bar magnet, or by an electromagnet, which consists of a coil wound from conducting wire. Some liquids react more strongly to magnetic fields than others. The fluids that react most strongly to magnetic fields are ferromagnetic, meaning they contain many permanent magnets, which align in a magnetic field. This effect is similar to the alignment of iron filings on a sheet of paper when a magnet is placed beneath the paper.

Most fluids that we come across in our everyday lives are not permanently magnetic, but all fluids have some reaction to magnetic fields. Fluids are either paramagnetic, in which case they are attracted by a magnet, or diamagnetic, in which case they are repelled by a magnet. Para- and diamagnetic fluids are less often studied than ferromagnetic fluids, because their interaction with a magnetic field is much weaker than that of a ferromagnetic fluid and a magnetic field.

In my thesis I investigate how exactly the shape of paramagnetic and diamagnetic drops changes in a magnetic field. I highlight the similarities between electric and magnetic fields, so that we can use some of the findings of controlling drops with the well-studied electric techniques on the less-well studied magnetic techniques. I also explore how the shaping of paramagnetic drops can be used to help solve problems in medical and food research.

Document control

K:\AAPS\D-AcademicAdministration\02-CodesOfPractice,Guidelines&Regulations\24-MainReferencesCopiesPolicies\01-Current\Assessment BOE SCC & Feedback\Forms\ThesisLaySummary	
If you require this document in an alternative format please email Academic.Services@ed.ac.uk or telephone 0131 651 4990.	Date last reviewed: 31.05.16

Abstract

The control of small volumes of fluids (or drops) is important for a wide range of applications, including lab-on-chip devices, where drops are transported and merged for sensing and chemical mixing; liquid lenses, where drops are shaped to set optical properties; and printing, where drops are generated by nozzles. Electric techniques are widely used to generate, transport, split and merge drops. Equivalent magnetic techniques are less well-known. Similarly to electric dipoles in electric fields, magnetic dipoles experience a force in magnetic fields. This effect, called magnetophoresis, is used to shape ferrofluids in magnetic valves and seals. Interest in shaping drops with magnetic fields for microfluidics has recently increased, and ferrofluids and paramagnetic salt solutions have been studied. The rich phenomenology of the interaction of magnetic fields and fluids offers ample opportunities for exploration. Diamagnetic fluids for example have no natural electric equivalent and are rarely studied as a tool for microfluidics.

In this thesis, I study the shaping of drops with magnetic fields. My research focus is on para- and diamagnetic salt solutions. Deformation of drops using external fields and induced magnetism has not been fully explored in the literature. I study here how induced magnetism can shape the liquid-vapour interface of drops and control solids that float on them. This thesis includes (i) an introduction to the background of the interaction of electromagnetic fields and fluids; (ii) a derivation of an expression for the shape of drops in electromagnetic fields; (iii) experimental validation of this expression through the measurement of the shape of para- and diamagnetic axisymmetric sessile drops in homogeneous magnetic fields; (iv) demonstration of the transport of para- and diamagnetic drops in magnetic field gradients; (v) explorations of the use of shaping drops with magnetic fields for rheological measurements, and for the controlled driving of objects floating on drops.

In summary, I explore how drops can be shaped in homogeneous magnetic fields, and how the drops can be transported by magnetic field gradients. These fundamental investigations may help stimulate novel applications of the controlled shaping of drops with magnetic fields. In particular, I explore how this technique can be used in rheology for food or medical research.

Declaration

I declare that this thesis has been composed solely by myself and that it has not been submitted, in whole or in part, in any previous application for a degree. Except where states otherwise in the text, the work presented is entirely my own. My contribution and those of colleagues to collaborative work have been explicitly indicated below. I confirm that appropriate credit has been given within this thesis where reference has been made to the work of others.

The data presented in Fig. 4.3 was obtained in an experiment carried out by Machiel G. Flokstra and myself in the School of Physics and Astronomy, University of St Andrews. I played a major role in the preparation and execution of the experiment, and the data analysis and interpretation are entirely by own work.

The work presented in Ch. 5 on paramagnetic drops was jointly conceived by myself, Glen McHale, and Adam A. Stokes. I was responsible for all experimental and analytical work and interpretation of the results. Glen McHale contributed to discussions. Adam A. Stokes provided project supervision.

The work presented on asymmetric objects in Sec. 6.3 was jointly conceived by myself, Paul Sullivan, Tushar Semwal and Adam A. Stokes. I was responsible for most experimental work and the analysis and interpretation of the results are entirely by my own work. Paul Sullivan and Tushar Semwal contributed to discussions and experiments. Adam A. Stokes provided project supervision.

Jennifer Dodoo

Edinburgh, United Kingdom

January 2020

Acknowledgements

Abbreviations

ADSA   Axisymmetric drop shape analysis
DEP   Dielectrophoresis
DMF   Digital microfluidics
EMST   Electromagnetic stress tensor
EWOD   Electrowetting-on-dielectric
MPMS   Magnetic Property Measurement System
MRI   Magnetic resonance imaging
MST   Magnetic stress tensor

Contents

List of Figures

List of Tables

List of QR Codes

Chapter 1

Introduction

1.1 Electromagnetic fields and fluids

The electromagnetic force belongs to the four fundamental forces (or interactions) in nature, along with the gravitational force, and the strong and weak forces (the nuclear forces that are extremely short-ranged and only relevant on a subatomic scale). The electromagnetic force is fundamental to our everyday experience: when we pick up a coffee mug it is the electron clouds of atoms in the mug and our hand that repel each other; when we read a piece of paper it is the scattering of electromagnetic waves (or their particle equivalent: photons), generated by a desk light or the sun and scattered of the paper, that convey the information written on the pages.

Clearly, electromagnetic interaction of fields and matter are of immense scientific interest. The fundamentals of electromagnetic field theory were laid in the late 19th century, in particular through the extensive experimental research into electricity and magnetism by Michael Faraday. His investigations explored the nature of electricity in an attempt to address the lack of an understanding of the fundamental principles governing the many known electric phenomena [1]. Faraday's concept of lines of forces traversing space stood in stark contrast to the widely accepted concept of attraction at a distance of mathematicians at the time [2]. Faraday was an exceptionally talented experimental scientist, but famously did not use any mathematical equations in his research [1, 3, 2]. A theoretical framework inspired by Faraday's researches was formulated a couple of decades later by James Clerk Maxwell. In "A treatise on electricity and magnetism" Maxwell developed a rigorous framework of the electromagnetic field theory. Maxwell himself saw his work as a translation of Faraday's ideas into the language of mathematics [2]. Through his formulation, he unified electricity and magnetism. The immense contribution of Maxwell's theories to our scientific understanding of the world and to the development of modern

technology is summarised by Richard Feynman: "From a long view of the history of mankind - seen from, say, ten thousand years from now - there can be little doubt that the most significant event of the 19th century will be judged as Maxwell's discovery of the laws of electrodynamics" [4].

Much of the findings of the research on electromagnetism of the 19th century is condensed in Maxwell's equations, which describe the origin and behaviour of electrostatic (Gauss's law of electric fields), magnetostatic (Gauss's law of magnetic fields) and induced electric (Faraday's law) and induced magnetic fields (Ampere-Maxwell law) [5]. Applying these fields to a volume induces an electromagnetic stress acting over its surface. If matter - for example water - fills the volume, the electromagnetic stress can be observed as an elongation or compression of the soft matter along the direction of the applied field lines. The electromagnetic stress tensor (EMST) captures this phenomenon and is derived from Maxwell's equations and the fundamental laws of thermodynamics and electromagnetism.

The EMST captures the forces acting on fluids in electric or magnetic fields -
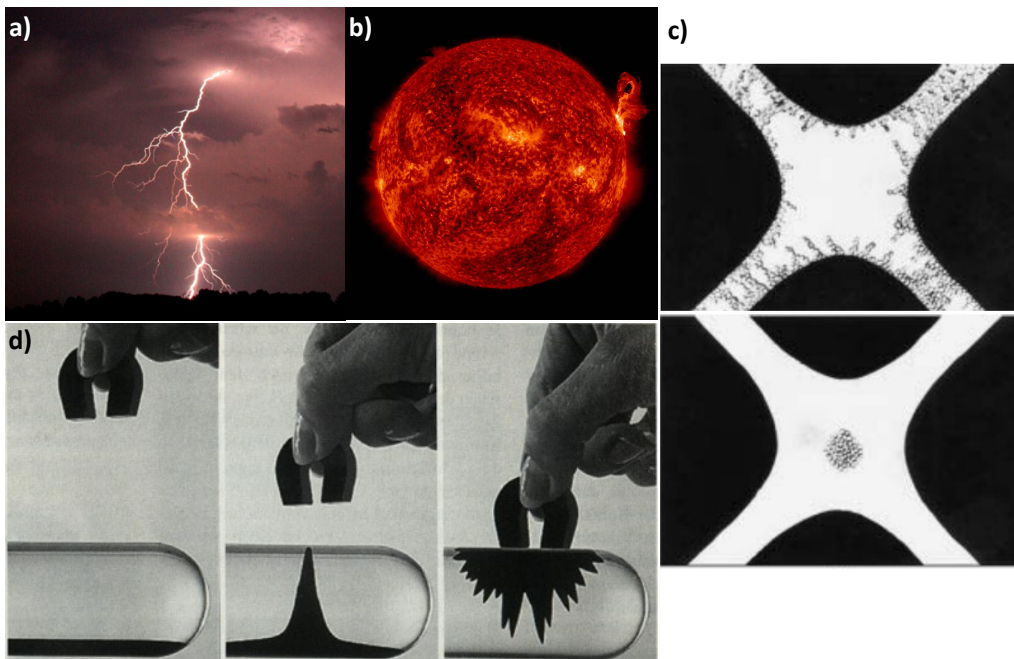
Figure 1.1: Examples of electro- and magnetohydrodynamic phenomena at the large and small scale. Electrodynamic effects include **a)** a lightning strike and **c)** the sorting of cells (grey circles) in the electric field of a quadrupole electrode (black shapes) due to positive (top) and negative (bottom) dielectrophoresis. **b)** The dynamics of the plasma of the sun and **d)** the attraction of a magnetic fluid containing iron compounds to a magnet are magnetohydrodynamic phenomena. I attached the details of the copyrights to a) and b) in Appendix A.1. The images in c) and d) are reproduced from Ref. [6] and [7] respectively, both with permission from John Wiley and Sons.

2

phenomena which are known as electro- and magnetohydrodynamics respectively. The fields interact with ions and electric and magnetic dipoles in the fluids. These interactions can deform or transport the fluid itself or affect particles suspended in the fluid with different electromagnetic properties than the fluid. Electro- and magnetohydrodynamic phenomena include:

- A lightning strike (Fig. 1.1a)), where a localized strong electric field causes the air to break down into a plasma and conduct electricity.

- The collection of cells at the points of highest and lowest field strength due to positive and negative dielectrophoresis respectively (Fig. 1.1c)), which depends on the electric properties of cells and suspending liquid, the electrode geometry and the frequency of the applied field.

- The interactions of the plasma of the sun and the magnetic field that is created by the flow of the plasma (Fig. 1.1b)).

- The attraction of a ferrofluid (a suspension of iron compounds) to a magnet (Fig. 1.1d)).

Consequently, by carefully choosing fluids based on their electromagnetic properties, and designing a suitable electromagnetic actuation mechanism, the movement of fluids can be controlled. This technique is particularly useful to microfluidics, where small volumes of fluids, or particles suspended in small volumes of fluids, are manipulated.

Microfluidics is both a science - attempting to answer questions regarding the behaviour and control of system comprised of small volumes of fluids - and a technology - utilising said behaviour and control for a broad range of applications, in particular in analysis [8]. Microfluidics needs to mature yet to fully appreciate its impact on industry and society. In the health sector in particular, it clearly has the potential to revolutionise applications such as drug development and point-of-care testing [8]. The actuation techniques implemented in microfluidics manipulate a small volume of fluid, such as a fluid meniscus or a drop, and include patterned surfaces, where the surface chemistry is modified to vary wettability and surface topology. Patterned surfaces have an intrinsic inflexibility due to their static nature, making an alternative, more flexible approach more desirable [9, 10]. These flexibility can be provided by disrupting the thermodynamic equilibrium of the system, such as through the introduction of thermal or concentration gradients, or the application of electromagnetic fields.

Electromagnetic microfluidic techniques have many industrial applications - to name but a few:

- biomedical, including sorting and transport of biomolecules in cell sorting, proteomics, immunoassays;

- printing, including drop ejection in inkjet printing;

- electrowetting and ferrofluidic displays;

- magnetic seals and valves, used in various applications such in pumps for fluids and pressure seals;

- liquid lenses, which have variable optical properties [11].

Typical electric actuation techniques used in these applications are dielectrophoresis, where bulk fluids or suspended particles are manipulated, and electrowetting, where a potential difference is applied across an interface. Magnetic actuation techniques implemented in these industries are largely based on magnetophoresis, where magnetic dipoles in solution or suspension are manipulated.

1.2   Motivation and problem definition

Electric actuation techniques in microfluidics are further developed and more widely implemented than magnetic actuation techniques. Magnetic actuation techniques are highly suitable for biomedical applications, due to the biocompatibility of many magnetic fluids and the possibility to apply large magnetic fields to the human body - as routinely done in Magnetic Resonance Imaging (MRI) - where contrasting agents contain gadolinium chloride, a paramagnetic salt.

Much of the rich phenomenology of interactions between magnetic fields and fluids remains to be explored. To enhance the control of magnetic fluids, magnetic particles are often used, for example in suspension in the fluid (ferrofluids). The interaction between the magnetic particles and an applied magnetic field is much stronger than the interaction between a fluid that does not contain these particles and a magnetic field. While magnetic particles are a good solution for some applications, they are not a representative model of many fluids that are common to everyday life and industrial applications. More often fluids are para- or diamagnetic rather than ferromagnetic. Magnetism is induced into these fluids by an applied field, opening ample opportunities for investigations. Induced magnetism holds information about the electronic structure of molecules in solution, and is versatile and tunable through the option of adjusting solute concentrations.

There are many parallels between the electric and magnetic actuation of fluids. The exclusive theoretical approaches to electromagnetic techniques inhibit the transfer of models and predictions from electric to magnetic fields and vice versa, and obscure fundamental differences. Diamagnetic fluids, having a negative magnetic susceptibility, offer in particular opportunities for investigation that have no natural electric equivalent.

1.3 Aims and objectives

The aim of this thesis is to explore the fundamental principles of shaping drops with magnetic fields, through experimental investigations and structured analysis.

1. The objectives of the theoretical analysis are:

   (a) to obtain an expression for the shape of a para- and diamagnetic drop in a magnetostatic field;

   (b) to predict the transport of drops in a magnetostatic field.

2. The objectives of the experimental investigations are:

   (a) to demonstrate and characterise shaping of drops in uniform magnetostatic fields;

   (b) to develop a computational package to measure and analyse the shape of a drop in uniform magnetostatic fields;

   (c) to demonstrate transport of drops in non-uniform magnetostatic fields.

   (d) to explore the application of shaping drops with magnetic fields to rheology and to controlled driving of objects.

Design criteria in meeting these objectives are:

- the computational analysis can be implemented in standard algorithms used in the field;

- the theoretical model is traceable to fundamental electromagnetism and thermodynamics;

- the transferability from magnetic to equivalent electric phenomena of the experimental and theoretical investigation is clarified.

By using a unified electromagnetic framework I hope to stimulate the development of industrial applications, such as novel designs of biomicrofluidic devices and rheological measurement tools, or tools for directed self-assembly.

1.4   Preview of contributions

The contributions of this thesis include:

- The derivation of an analytical expression for the shape of a drop in an electromagnetic field.

- The development of an experimental set-up to actuate magnetic drops.

- The development of a computational package to measure the shape of drops and analyse the shape in uniform magnetostatic fields.

- The experimental demonstration of shaping and transporting para- and diamagnetic drops with magnetic fields.

- The experimental exploration of shaping drops with magnetic fields for rheological measurements.

- The experimental exploration of controlled driving of diamagnetic floating objects on paramagnetic drops.

1.5 Publications

The original work presented in this thesis has led to two journal publications and seven conference contributions.

Peer-reviewed journal publications

- **Jennifer Dodoo** and Adam A. Stokes, **Shaping and transporting diamagnetic sessile drops**, *Biomicrofluidics*, vol. 13, pp. 064110-1-064110-6, 2019. Attached in Appendix C.

Other publications

- **Jennifer Dodoo**, Glen McHale, and Adam A. Stokes, **Shaping of sessile magnetic drops due to electromagnetic stress**; Preprint published at arXiv:1908.05193. Attached in Appendix B.

Peer-reviewed conference contributions

- **Droplets 2019**, Durham, Oral presentation titled *Controlled shaping of sessile magnetic droplets.*

- **International Soft Matter Conference 2019**, Edinburgh, Poster presentation titled *Stressed Magnetic Droplets.*

- **Electrowetting 2018**, Enschede, Poster presentation titled *A Holistic Review of Wetting of Droplets.*

- **Bioelectronics Workshop 2017**, Berlin, Poster Presentation titled *A Holistic Review of Electrohydrodynamics.*

Non-peer-reviewed conference contributions

- **2nd UKFN ECR Event 2019**, Nottingham, (UK Fluids Network Early Career Researcher), Poster presentation titled *Stressed Magnetic Droplets.*

- **EPSRC CDT-ISM Annual Conference 2018**, Glasgow, Oral presentation titled *One more reason to love Maxwell's Equations.*

- **University of Edinburgh School of Engineering Research Conference 2018**, Edinburgh, Oral presentation and poster titled *A Holistic Review of Electrohydrodynamics.*

During the course of my doctoral studies, I was awarded awards and grants for my scientific and extracurricular work.

Awards

- **CR Barber Trust**, awarded by the IOP in support of my contribution to the Electrowetting 2018 conference in Twente.

- University of Edinburgh School of Engineering Research Conference 2018 **Best 2-min presentation**, awarded for *A Holistic Review of Electrohydrodynamics.*

- EPSRC CDT-ISM Annual Conference 2017 **Best Outreach**, awarded for participation at the Accenture Tech UK Girls in STEM event; the 3MT University of Edinburgh event; and the Edinburgh Science Festival (all 2017).

- **3MT 2017 University Finalist**, awarded for the presentation *A Nanotech Biosensor for Gout.*

- **3MT 2017 School of Engineering Heat Winner**, awarded for the presentation *A Nanotech Biosensor for Gout.*

Grants

- **Industry Placement Grant (£2000)** on *A Nanotech Biosensor for Gout* at NanoFlex, Daresbury, UK, by the EPSRC CDT-ISM.

1.6   Use of QR codes

Throughout this thesis I use QR codes to link content to videos. These videos can be accessed with a smart phone, by reading the QR code with the camera function or using a free QR code reader application, which can be downloaded from the Appstore (*QR reader for iPhone*) or Google Play Store (*QR Code Reader*).

Test your QR code reader - website of the Soft Systems Group

1.7 Thesis outline

This thesis is comprised of two overarching topics, namely (i) the analytical and (ii) experimental investigation into the fundamentals of shaping drops with magnetic fields. The thesis consists of six chapters in addition to the present chapter: an introductory chapter; a chapter on the theory; a chapter on the materials and methods; two experimental chapters; a concluding chapter. The chapter on the theory is dedicated to topic (i). The experimental chapters mainly focus on topic (ii), but draw on (i) to inform the experimental design and analysis.

- In **Chapter 2** I introduce the background concepts used in this thesis, including the electromagnetic actuation of fluids and digital microfluidics.

- In **Chapter 3** I discuss how the EMST captures the forces acting on a liquid-vapour interface in an electromagnetic field. From the EMST, I derive an expression of the shape of a drop in an electromagnetic field.

- In **Chapter 4** I describe the experimental methods and materials used in this thesis, including a description of the computational analysis software that I developed ('Axisymmetric Drop Shape Analysis in electromagnetic fields').

- In **Chapter 5** I experimentally validate the expression found in Chapter 3, through the measurement and analysis of the shape of para- and diamagnetic drops in a uniform magnetic field. I also demonstrate transporting drops with a non-uniform magnetic field.

- In **Chapter 6** I explore applications of shaping drops with magnetic fields, namely rheological measurements and controlled driving of diamagnetic objects floating on paramagnetic drops.

- In **Chapter 7** I summarise the content of this thesis and discuss the potential impact of the presented original work on microfluidics and beyond.

Chapter 2

Background to shaping drops with magnetic fields

2.1 Introduction

In this chapter I introduce the background to shaping drops with magnetic fields, which includes topics such as the electromagnetic actuation of fluids and digital microfluidics (DMF).

In Sec. 2.2 I review some of the defining experiments on the electromagnetic actuation of fluids from the 19th century and discuss how the phenomenological concepts behind these experiments are still exploited today for modern applications, including controlling floating objects, measuring rheological properties of cells, and actuating drops for DMF. In Sec. 2.3 I give an overview of DMF. In Sec. 2.4 I discuss the magnetic properties of fluids and their use for DMF in Sec. 2.5. In Sec. 2.6 I discuss the measurement and analysis of the shape of drops, which holds information about the stresses acting on the drop and is important to design and characterise actuation techniques.

To discuss the electric and magnetic properties of fluids I use the terms electric and magnetic susceptibility (χ_e and χ_m respectively), as well as electric permittivity ϵ and magnetic permeability μ. The relation between these quantities is $\epsilon = \epsilon_0(1 + \chi_e)$ and $\mu = \mu_0(1 + \chi_m)$, where ϵ_0 and μ_0 are the vacuum permittivity and permeability respectively.

13

2.2 Electromagnetic actuation of fluids

Some of the most defining electro- and magnetohydronamic research has been conducted in the 19th century and includes experiments on bulk electrowetting by Lippmann [12, 10], on bulk dielectrophoresis by Pellat [13].

Lippmann found that the height-of-rise of a column of mercury interfacing an electrolyte (ionic) solution depends on the voltage applied across the interface (see Fig. 2.1a)). A glass tube, filled with mercury (Hg), ends in a thin capillary, submerged in a beaker containing acid water (10% sulfuric acid by volume) (A) and mercury (Hg), which sits at the bottom of the beaker. The height of mercury in the capillary is observed through a microscope (M). Voltages are applied to copper wires connected to the mercury in the tube (V1) and in the beaker (V2). The height of rise of mercury in the capillary depends on the potential difference V1-V2.

Pellat showed that the column of dielectric liquid (non-volatile oil) rises in an alternating (at a frequency of 260 Hz) electric field. The height-of-rise of the liquid depends on the applied field strength and the electric susceptibility of the liquid (see
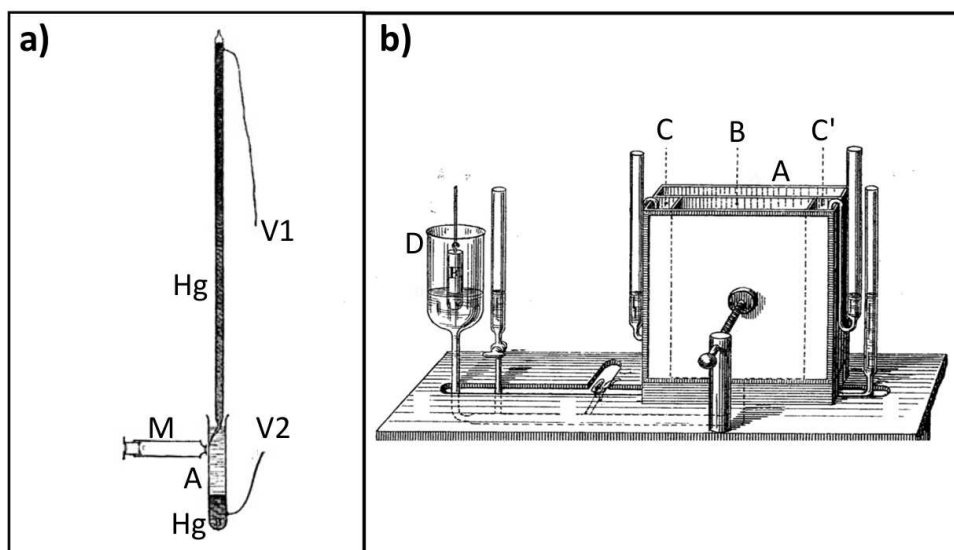
Figure 2.1: Electrohydrodynamic experiments of the 19th century. **a)** Illustration of Lippmann's experiment on electrocapillarity. The height of rise of mercury (Hg) in a tube, sitting in a bath of acid water (10% sulfuric acid by volume) (A), is measured using a microscope (M) as a function of the voltage applied across it (V1-V2). Reproduced from Ref. [12] with permission from the Bibliothèque nationale de France. **b)** Illustration of Pellat's experiment. A parallel plate capacitor (A) contains ebonite boxes (B, C and C') which are filled with non-volatile oil. B is connected to the beaker (D) in which the oil level is measured through a flotation device (F) as a function of the voltage applied to the capacitor. Reproduced from Ref. [13] with permission from the Bibliothèque nationale de France.

Fig. 2.1b)). A parallel plate capactior with outer walls (A) encloses boxes of ebonite (B, C and C′) containing oil. A beaker (D) contains non-volatile oil and is connected to an ebonite box (B). The level of oil in D is measured through a flotation device (F). The charge on the capacitor is rapidly alternated (260 times per second) resulting in a rise of liquid in the capacitor (measured as a lowering of liquid in D).

These height of rise experiments can be adapted to measure the magnetic susceptibility of fluids using the Quincke method, where the rise of a column of a paramagnetic or diamagnetic liquid in a magnetic field is studied [14, 15]. A column of liquid with an liquid-vapour interface is exposed to a magnetic field that is oriented perpendicular to the surface normal of the interface. The height of rise of the liquid is measured as a function of the applied field. A liquid with a positive magnetic susceptibility is pulled into the magnetic field applied to one end of the fluid column. The height-of-rise of the fluid depends on the value of the magnetic susceptibility and the strength of the magnetic fields applied.

There are several commonalities of note in these experiments: (1) an observable change occurs to a liquid upon application of an electromagnetic field; (2) the change is visible at the liquid-liquid or liquid-vapour interface; (3) the strength of the effect depends on the electromagnetic properties of the fluid and the applied field. Many of the electromagnetic actuation techniques of fluids that are applied in industry - such as electrowetting, dielectrophoresis, magnetowetting, and magnetophoresis - are based on the electro- and magnetohydrodynamic research of the 19th century.

Applications include:

- Cooling of equipment and space suits. Electrowetting can be used to spread liquid films on a surface where they evaporate, resulting in cooling (EHD conduction pumping). The cooling can be enhanced using a DEP force, generated by a localised nonuniform electric field, which extracts bubbles from the liquid [16].

- Sorting of cells. Time-dependent fields are widely applied in DEP of particles in suspension to utilise the frequency-dependence of electric permittivities. Dielectrophoresis of suspended particles has found many biomedical applications [17, 18], including sorting of cells as demonstrated by Pohl [19].

- Magnetic tweezers microrheology. A magnetic field gradient exerts a force on a para- or ferromagnetic particle, as shown by Fig. 2.2. The subsequent displacement of the particle is measured and holds information about the rheological properties of the material [20]. This is discussed in more detail in Ch. 6.

- Density measurements. Magnetophoresis of solids and liquids in suspension, can for example be used to sort scrap metal [7], or for density measurements [21, 22] (shown by Fig. 2.3a)). Diamagnetic objects can be driven on a liquid-vapour interface [23, 24], as shown by Fig. 2.3b), which is discussed in more detail in Ch. 6.

- Microfluidics. The control of small quantities of fluids is important in microfluidics [8] and DMF [25, 26, 27], where drops are manipulated; and is a key ingredient for liquid lenses to set optical properties [11]. DMF has strong biomedical applications, such as proteomics, imunoassays, and the study of cells [28, 29, 30]. I will discuss DMF in Sec. 2.3.
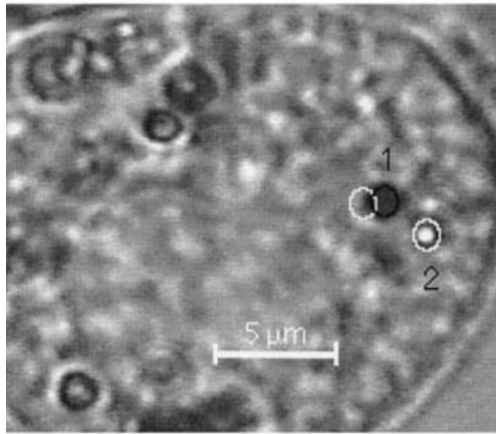
Figure 2.2: Magnetic tweezers are used to measure the rheological properties of the cytoplasm of a cell. A magnetic particle (1) is displaced by a magnetic field pulse, whereas a latex bead (2) remains stationary. The movement of the magnetic particle holds information about the rheological properties of the fluid. Reproduced from Ref. [20] with permission from Elsevier.
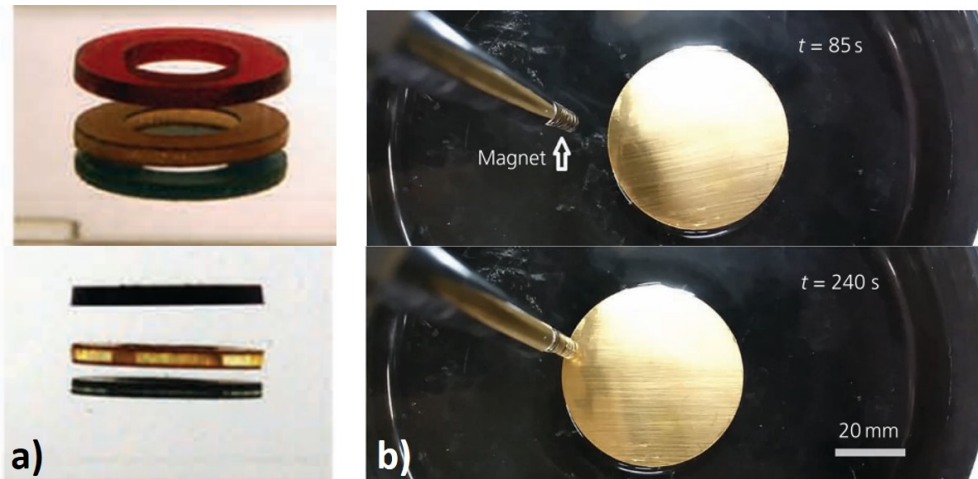
Figure 2.3: Organising and transporting solids with magnetic fields. **a)** Levitating polymer structures assemble such that their density increases from top to bottom. Reproduced from Ref. [22] with permission from John Wiley and Sons. **b)** A floating diamagnetic body (gold) is driven by a magnet. Reproduced from Ref. [24] with permission from ICE Publishing.

2.3 Digital microfluidics

In DMF small volumes of fluids are actuated and transported on designated platforms for mixing and sensing applications. Basic operations in DMF are drop generation, transport, splitting, merging. Actuation techniques include surface acoustic waves (SAW) [31, 32], and electric [25, 26, 27, 28, 29, 30] and magnetic [33, 34, 35, 36, 37, 38] fields.

Two examples of electric actuation techniques that are commonly used in DMF are Electrowetting-on-dielectric (EWOD) [39, 10, 40] and liquid dielectrophoresis [41, 42, 43, 44]. These techniques have been implemented in DMF devices for drop generation, transportion, splitting and merging [25, 26, 27, 28, 29, 30].
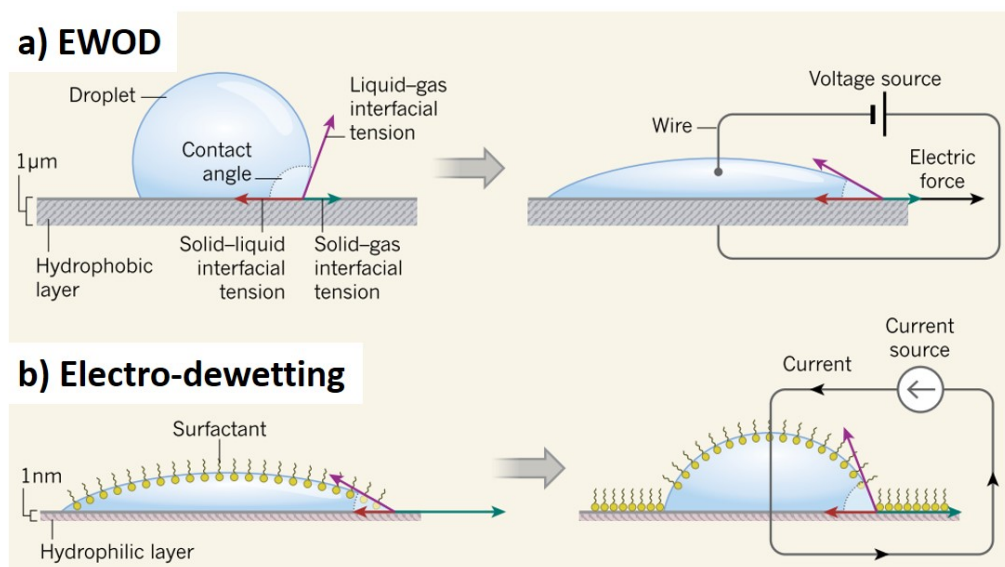
Figure 2.4: Illustration of electrowetting-on-dielectric (EWOD) and Electro-dewetting. **a)** In EWOD a drop sits on an electrode coated with a hydrophobic dielectric. In thermodynamic equilibrium, the forces due to interfacial tensions are balanced at the contact line. The solid-gas interfacial tension is smaller than the solid-liquid interfacial tension, which makes a minimisation of the solid-liquid interface energetically favourable. When a voltage is applied across the drop, the solid-liquid interfacial tension is reduced, forcing the drop to wet the surface. **b)** In Electro-dewetting, a drop sits on an electrode with a hydrophillic layer of ionic surfactant that envelopes the liquid-gas interface of the drop. Upon application of a voltage across the drop, the surfactant is forced towards the substrate of the electrode, minimising the solid-liquid interface of the drop, and therefore dewetting the drop. Reproduced from Ref. [45] with permission from Springer Nature.

EWOD is an electric actuation technique where the contact angle between a drop and an insulated electrode is altered through the application of a non-uniform electric field, as shown by Fig. 2.4a). A thin layer of hydrophobic dielectric has been introduced to Lippmann's experiment, between electrode and liquid to reduce the effects of electrolysis, a modification which was first introduced by Berge [46]. However, issues remain with the reliability of this technology. The actuation voltage needs to be increased when using a dielectric layer compared to using no dielectric layer and the surface may be compromised over time due to electric charging [47] and biofouling [48]. A recent publication on electrical dewetting (the reverse phenomenological effect to wetting) proposes to place drops on hydrophilic conductive substrates coated with ionic surfactants [49]. The wetting and dewetting of the drop is controlled by the interaction of the ionic surfactant with the applied electric field.

For actuation by liquid-dielectrophoresis, drops can be coated with hydrophobic particles to form a marble [50, 51]. An example of a dielectric marble in a uniform electric field is shown by Fig. 2.5. Dielectric drops (10 µl of water and of methylene iodide (MI)) are coated with hydrophobic particles. Upon application of a uniform electric field (with field strength $E = 7 \times 10^5$ V/m) the drops elongate along the field lines. The dielectric constant of water is an order of magnitude larger than that of MI ($\epsilon_{H_2O} = 79$, $\epsilon_{MI} = 5$), causing the water drop to elongate more strongly in the applied field than the MI drop.
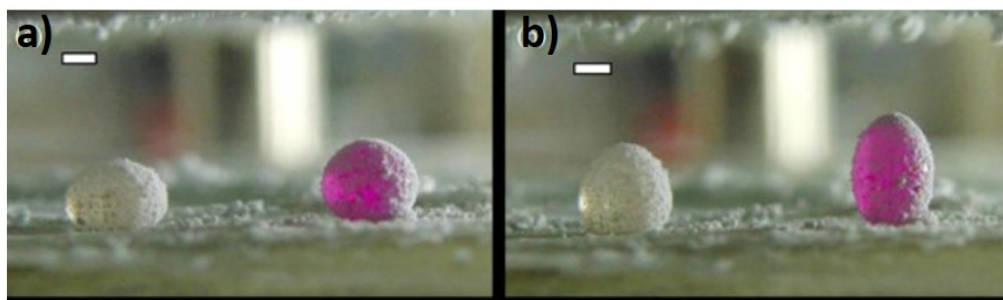
Figure 2.5: Dielectric drops coated with hydrophobic particles are elongated in a uniform electric field. The drops are 10 µl of water (red) and methylene iodide (white). The scale bar is 1 mm. **a)** The applied field is 0 V/m. **b)** The applied field is 7×10^5 V/m. The water drop deforms more strongly in the electric field because of its larger dielectric constant ($\epsilon_{H_2O} = 79$, $\epsilon_{MI} = 5$). Reproduced from Ref. [51] with permission from AIP Publishing.

Drops can also be controlled using magnetic phenomena. Magnetic actuation techniques are highly suitable for biomedical applications, due to the biocompatibility of many magnetic fluids and the possibility to apply large magnetic fields to the human body - as routinely done in Magnetic Resonance Imaging (MRI) - where contrasting agents contain gadolinium chloride, a paramagnetic salt. I discuss the magnetic properties of fluids in the following section, before discussing their use in magnetic DMF.

2.4   Magnetic properties of fluids

The magnetic properties of fluids can be classified as ferro-, para- or diamagnetic, depending on the magnetic susceptibility of the fluid. Fluids with a positive magnetic susceptibility, such as ferrofluids or paramagnetic salt solutions, are attracted into a magnetic field. Fluids with a negative magnetic susceptibility are diamagnetic, such as water and solutions of diamagnetic salts, and are repulsed from a magnetic field. The magnetic susceptibility of solutions can be measured using a variety of techniques, including nuclear magnetic resonance [52], where a shift in the resonance frequency of protons due to induced magnetism is measured; a SQUID magnetometer [53], where the induced magnetic field is measured with highly sensitive pick-up coils; or using the Quincke method [14], where the height-of-rise of a liquid in a magnetic field is measured.

Ferrofluids are suspensions of ferromagnetic particles - they are complex fluids. Ferromagnets contain magnetic dipoles which are aligned with their nearest neighbours. Upon application of a magnetic field, the dipoles align with the external field. Ferromagnetic materials include iron, cobalt, nickel, and compounds containing one or more of these elements. Ferrofluids are suspensions of iron compounds - such as magnetite (Fe_3O_4), a ferromagnetic rock mineral that can be found in beach sand - in water or oil. Upon application of a magnetic field, the ferrofluid forms cones directed along the field lines. The number and size of the increases with the applied field strength and decreases with surface tension [54].

An alternative to ferrofluids are paramagnetic salt solutions, which contain uniformly distributed, randomly oriented, weak magnetic dipoles. Upon application of a magnetic field, the dipoles align along the direction of the field lines. The magnetic susceptibility of paramagnetic materials ($0 < \chi << 1$) is orders of magnitude smaller than that of ferrofluids ($0 << \chi$). Generally, atoms with an unpaired electron are paramagnetic. There are some soluble paramagnetic salts with a relatively strong magnetic susceptibility, such as manganese chloride tetrahydrate ($MnCl_2 \cdot 4H_2O$) or gadolinium chloride hexahydrate ($GdCl_3 \cdot 6H_2O$).

Diamagnetic materials, such as water, have a weak negative magnetic susceptibility ($-1 << \chi < 0$). Many biological objects, such as frogs, consist mainly of water and are diamagnetic. Fig. 2.6a) shows a frog levitating in a strong magnetic field (16 T). The frog is diamagnetic, and therefore confined to the region of lowest magnetic field strength [56]. Due to their small magnetic susceptibility, the force on diamagnetic fluids is weak. To increase the magnitude of the force, diamagnetic materials are suspended in paramagnetic fluids [57] or ferrofluids [55]. The diamagnetic object is then repelled from the region of highest magnetic field strength. Fig. 2.6b)-c) shows an example of a microfluidic channel where this phenomenon is used to sort magnetic and diamagnetic particles. When suspended in a dilute aqueous ferrofluid, the magnetic particles are attracted to a magnet that is placed on one side of the channel. The diamagnetic particles are repelled from the magnet, which is not the case when they are suspended in water (Fig. 2.6c)). The particles can therefore be sorted into different channels, depending on their magnetisation. This suspension of diamagnetic particles or drops in magnetic or paramagnetic fluids increases their usability for microfluidic applications. In this case, the magnetic force on the dilute ferrofluid and magnetic particles dominates the interaction. Therefore, rather than studying the interaction between the magnetic field and the diamagnetic material,
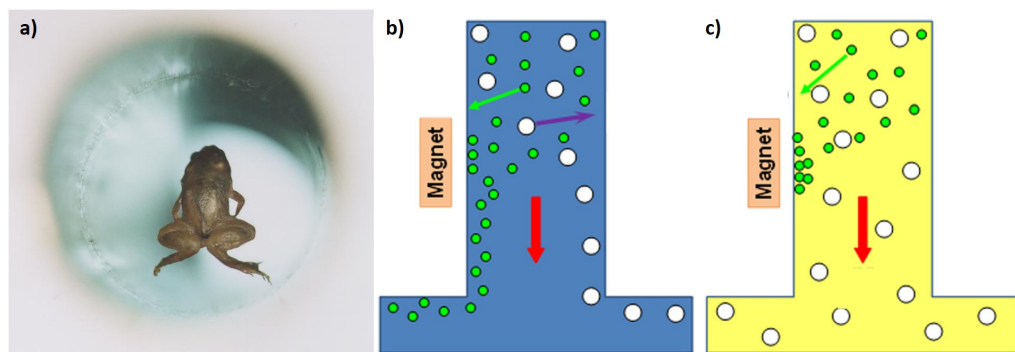
Figure 2.6: Examples of diamagnetic phenomena. **a)** A frog levitating in a magnetic field. The frog consists mainly of water, which is diamagnetic and confined to the region of smallest magnetic field strength. **b)** and **c)** are illustrations of a microchannel containing magnetic (green) and diamagnetic (white) particles. In **b)** the channel is filled with a dilute aqueous ferrofluid and the particles are sorted in a magnetic field into magnetic particles - which are attracted to the magnet - and diamagnetic particles - which are repelled from the magnet. In **c)** the channel is filled with water, respectively reducing and increasing the difference in magnetic susceptibility between the diamagnetic and magnetic particles and the fluid. The magnetic particles are so strongly attracted to the magnet that they are pulled out of the fluid flow, while the diamagnetic particles are not visibly repelled by the magnetic field. I attached the details of the copyright to a) in Appendix A.2. The images shown in b) and c) are reproduced from Ref. [55] with permission from AIP Publishing.

the interaction between the magnetic fluid and the magnetic field is studied. I highlight this distinction here, because paramagnetism and diamagnetism are separate physical phenomena, which I will discuss in more detail in Ch. 3. Since there is no electrical equivalent in natural materials (negative electric susceptibility), the study of diamagnetic materials is specific to magnetism. Diamagnetic materials offer therefore an opportunity for DMF that electric techniques do not. There is a lack of studies on the shaping of diamagnetic drops in air.

A recent review by Bormashenko [58] highlights the scientific interest and applications of bulk diamagnetism. Recent publications on this topic include work on the magnetic deformation of diamagnetic liquid-air interfaces ('Moses effect') [59] and on floating diamagnetic bodies [23, 24].

2.5   Magnetic digital microfluidics

In magnetic DMF drops containing magnetic dipoles are actuated using magnetic fields [36, 60, 37]. Magnetic techniques do not suffer the same disadvantages as electric techniques, such as a requirement for contact between the electrode and the drop, and electric charging of the substrate [36].

An overview of actuation techniques in magnetic DMF is presented by Fig. 2.7. The magnetic field is either generated by a permanent magnet, in which case the field strength is set by the properties of the magnet and the distance to the sample, or by an electromagnet, in which case the field strength is set by the properties of the electromagnet, the current going through the coils of the electromagnet, as well as the distance to the sample. Permanent magnets have a high magnetic flux density and even small magnets (button magnets commonly have 0.1-0.5 T) can be used to move drops. However, their permanent nature limits the range of field strengths that can be applied to a drop. Electromagnets are more flexible and can be integrated into lab-on-chip platforms using microfabrication tools [61, 35]. An example of integrated electromagnets is shown by Fig. 2.7b), where a 10 μl water drop containing magnetite particles sits on a teflon coated printed-electric circuit board (PCB). An external magnetic field is applied to the magnetic particles to magnetise them uniformly, and current is applied to the PCB to generate a magnetic field gradient that causes the particles to move [35].

Magnetic actuation can be classified into indirect techniques, where the applied magnetic field acts on a material - which in turn deforms and transports the drop - and direct techniques - where the applied field acts on the drop itself. I discuss magnetic actuation mechanisms in more detail in the following sections.
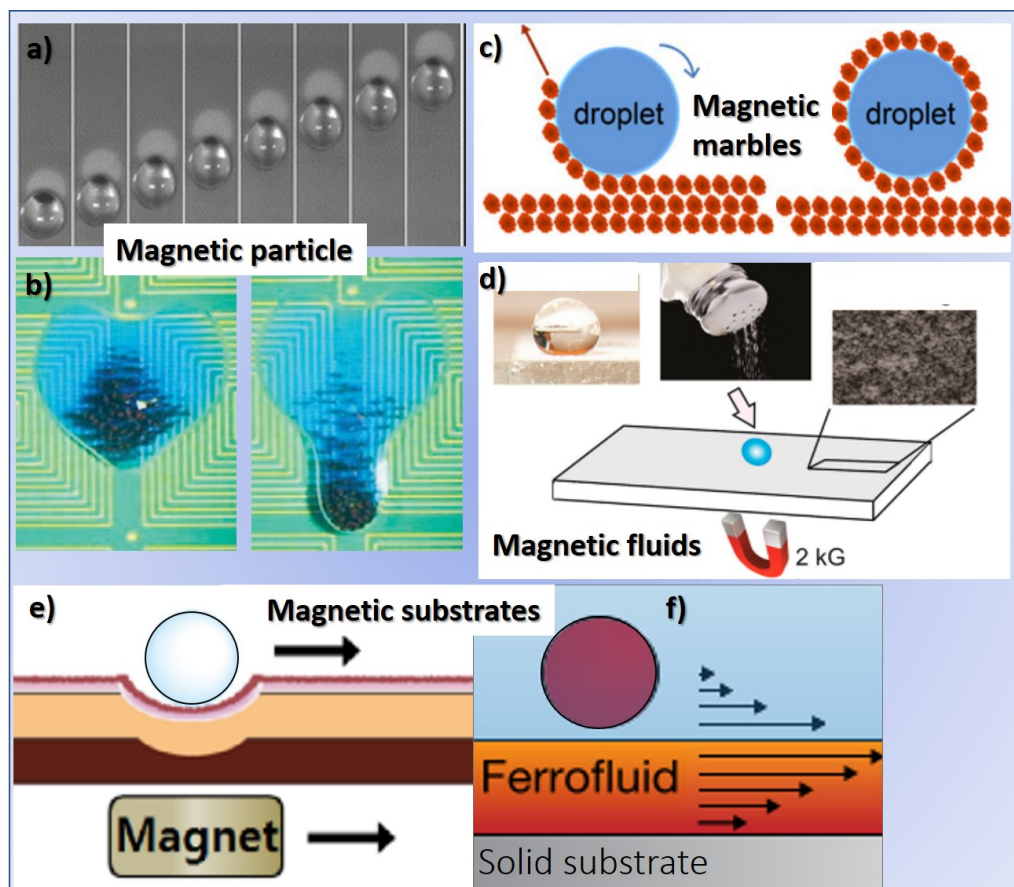
Figure 2.7: Overview of actuation techniques in magnetic digital microfluidics (magnetic DMF) where drops are actuated using magnetic fields. Drops can be actuated by added magnetic particles to them and moving them with **a)** a permanent magnet [62]; or **b)** an electromagnet, here integrated on a substrate using microfabrication [35]. Magnetic marbles can be constructed, where **c)** magnetic particles envelope a drop [63]. **d)** A drop can be actuated directly by a magnetic field, if the properties of the drop and field are chosen such that a large enough force can be generated. This may be achieved using paramagnetic salts [64]. Drops can also be indirectly actuated by deforming magnetic substrates, such as **e)** magnetic elastomers with superhydrophobic surfaces [65], or **f)** ferrofluid-containing liquid-infused porous surfaces (FLIPS) [66]. The images are reproduced from their respective references with permissions from the Royal Society of Chemistry (a), Elsevier (b), Springer Nature (c,f), American Chemical Society (d), and John Wiley and Sons (e).

2.5.1   Indirect actuation

Drops can be moved using magnetic particles, such as in the examples shown by Fig. 2.7a)-b), where a drop containing magnetic particles is moved by a) a permanent magnet [62] and b) an electromagnet [35]. The particles visibly drag the fluid along, which can lead to significant deformation of the drop, such as visible in Fig. 2.7 b).

23

In magnetic marbles, the force on the drop is more evenly distributed. An example of the construction of a magnetic marbles is shown by Fig. 2.7c). Magnetic marbles are either created using particles that are highly susceptible to a magnetic field to enclose a drop that is weakly susceptible to a magnetic field [63]; or vice versa [67]. An example of the first case is a water drop coated with superhydrophobic magnetite nanoparticles [63]. An example of the second case is a marble containing ferrofluid and coated with polyvinylidene fluoride (PVDF) nanobeads.

Another example of indirect actuation are magnetic substrates, where the drop sits on a substrate that deforms upon application of a magnetic field, subsequently actuating the drop. Those substrates generally consist of a deformable layer that is highly susceptible to magnetic fields and a modification to the contact area between drop and substrate that reduced adhesion. Examples of such substrates include magnetic elastomers which are either coated with a superhydrophobic layer [65] or modified with micro-pillars [38]; or ferrofluid-containing liquid-infused porous surfaces (FLIPS), where the ferrofluid envelopes the drop [66]. An example of a magnetic elastomer with a superhydrophobic surface [65] is shown by Fig. 2.7e). The substrate consists of three elastomer layers and a superhydrophobic layer on top. The second layer from the bottom is the magnetic elastomer, which consists of silicon mixed with iron particles. Upon application of a magnetic field, the elastic membrane is deformed, subsequently manipulating the drop. A schematic of a FLIPS is shown by Fig. 2.7f). FLIPS are solid substrates covered with ferrofluid. The drop is in contact with the ferrofluid which envelopes the drop. Upon application of a magnetic field, the ferrofluid is actuated, subsequently shaping and transporting the drop [66].

2.5.2 Direct actuation

A magnetic field can directly interact with a drop, as illustrated by Fig. 2.7d). To generate a large enough force on the drop, the fluid needs to have a suitable magnetic susceptibility. The force on the drop depends on the difference between the magnetic susceptibility of the drop and of the medium surrounding the drop. The larger the difference in magnetic susceptibility of the two media, the stronger the force on the drop upon application of a magnetic field.

Ferrofluids are highly susceptible to magnetic fields and can therefore be directly actuated with a magnetic field. Ferrofluidic drops can be used to transport drops of analyte or reagent on a magnetic DMF platform [68]. In this example, the ferrofluidic drop acts as an engine to drive a cargo drop that is attached to it.

Drops of aqueous solutions of paramagnetic salts have been actuated by on su-perhydrophobic surfaces [33]. In paramagnetic salt solutions, the magnetic suscep-tibility can be tuned through the concentration of salt. The relationship between salt concentration and ease of actuation has been studied [64] and implemented for electrochemical detection [34] and fluorescence measurements [64].

Diamagnetic fluids can also be directly actuated by magnetic fields. A microflu-idics platform has been designed where levitating pico- to femto-litre diamagnetic drops, such as glycerine-water solutions, and particles, such as polystyrene beads, are manipulated using a magnetic field [69].

A good understanding of the interaction between magnetic fields and drops helps to inform designs for drop manipulation in DMF. A common method to quantify the properties of a drop, such as volume and density, and the stress on a drop due to the application of a field, is to measure the shape of the drop. In the next section I discuss the measurement and analysis of the shape of drops.

2.6 Measurement and analysis of the shape of drops

The measurement of the shape of a drop is generally performed optically, by taking a photograph of the drop. For axisymmetric drops - drops with rotational symmetry around its mayor axis - the shape can be fully defined in 2D. When imaging the drop for a shape measurement it therefore only needs to show the interface of the liquid phase with surrounding phases. For drops that are attached to a surface, such as pendant or sessile drops, this image is a side-profile photograph of the drop showing the liquid-vapour and liquid-solid interface. To simplify the measurement of the shape of the drop, there should be a high contrast between the drop and the background, which can be achieved by placing a diffusive light source in the background. The shape of the drop is then generally measured computationally using the Axisymmetric Drop Shape Analysis (ADSA) [70] or a similar algorithm. In ADSA, the image is binarized - each pixel is either turned black or white depending on a predetermined threshold of the colour of the pixel. A suitable threshold for the conversion to binary causes the background on binary image to be white and the drop black or vice versa. The outline of the drop is then defined as the outline of the shape in the binary image. During this step there is usually an error introduced between the real shape of the drop and the identified shape, which depends on the random fluctuations in lighting.

To analyse the shape of the drop, the stresses acting on the drop need to be considered. A common approach to describe the shape of drops is by balancing the differences in stresses, such as stresses due to gravity and surface tension, across the liquid-vapour interface (Young-Laplace equation). The Young-Laplace equation can be adapted for electromagnetic fields by including in the stress balance the difference in electromagnetic stress - usually evaluated using the Maxwell stress tensor (MST). The Young-Laplace equation has been modified accordingly and applied to the deformation of drops in electromagnetic fields.

The shape of drops in electric fields has been studied, including the break-up of drops in electric (magnetic) fields [71]; the strong deformation and formation of conical ends of dielectric drops in electric fields [72]; the deformation of conducting drops in uniform electric fields [73]. The MST has also been applied to dielectrophoresis [74, 75, 76] and electrowetting [75, 77], highlighting the frequency-dependence between electrowetting and DEP.

The shape of ferrofluidic drops in magnetic fields has also been extensively studied [78, 79, 80, 81] and comprehensively reviewed [60]. Current research questions include topics such as the field dependence of the surface tension of the ferrofluidic drops. A study of the shape of suspended ferrofluidic drops in a magnetic field found a field-dependent surface tension of the drops, caused by field-induced structural

changes at the liquid-vapour interface [82]. A later study however suggests that the surface tension of the drops can remain field-independent if spherical instead of ellipsoidal coordinates are used to describe the outline of the drop [83].

The MST is only valid in vacuum, as it is a reduced form of the electromagnetic stress tensor (EMST). The EMST is universally valid for quasi-static non-dissipative processes [84] and generally depends on the thermodynamic potential of the system; the electric permittivity; the magnetic susceptibility; and the electromagnetic field applied. Rowghanian *et al.* [83] used the EMST to modify the Young-Laplace equation and describe the shape of a suspended ferrofluid drop in a magnetic field.

The classical derivation of the EMST derives the electric stress on a volume caused by the application of an electrostatic field that is generated by a simple plate capacitor [85]. The electric stress is then transformed to magnetic stress using the argument that electrostatics and magnetostatics are completely analogous. Several issues were highlighted with this derivation, namely that (i) owing to the simple geometry of the plate capacitor, the field gradient terms are neglected from the start of the derivation; (ii) the transformation to magnetic fields is not sufficiently justified [84]. More recently, Stierstadt and Liu addressed these issues in a more complete derivation and treatment of the EMST [84].

2.7 Summary and conclusion

This chapter introduced the background to shaping drops with magnetic fields. The fundamental principles of key historical experiments on the interaction of electromagnetic fields and fluids are still used in modern applications, such as magnetic tweezers for rheological measurements in cells; the organisation and control of diamagnetic solids in fluids; and DMF.

Common actuation techniques in DMF include electrowetting and liquid dielectrophoresis. Fluids can be classified as ferro-, para-, or diamagnetic, and these properties can be exploited for DMF. Drops can be indirectly actuated with magnetic fields, for example by using magnetically deformable substrates; or they can be directly actuated, by using magnetic liquids. In direct actuation, the drops are deformed by the magnetic field.

To understand the stresses acting on the drops, the shape of the drops can be studied. For this, the shape of the drops is measured on an image and analysed computationally. The mathematical expression for the stress balance of a drop in thermodynamic equilibrium is the Young-Laplace equation. Usually this equation includes the stresses due to gravity and surface tension, but can be modified for drops in electromagnetic fields using the EMST.

In this thesis I study the shape of para- and diamagnetic drops. The experimental work is inspired by the work of Mats *at al.* [64] who recently demonstrated the actuation of paramagnetic drops on superhydrophobic surfaces, combined with the detailed study of the shape of drops in magnetic fields as presented by Afkhami *et al.* [82] and Rowghanian *et al.* [83] who studied the shape of suspended ferromagnetic drops. My theoretical work is based on the work by Stierstadt and Liu [84] who discussed the application of the electromagnetic stress tensor to volumes of fluid in detail.

In the following chapter, I use the EMST to derive an expression for the shape of a paramagnetic sessile drop in a magnetostatic field.

Chapter 3

Theory of shaping drops with magnetic fields

3.1 Introduction

In this Chapter, starting from a discussion of the EMST which captures the forces acting on fluids at rest due to electromagnetic fields, I derive an expression for the shape of axisymmetric drops in magnetic fields.

In Sec. 3.2 I introduce the boundary conditions to the EMST. I define the stress tensor in a fluid at rest in Sec. 3.3. In Sec. 3.4 I simplify the EMST to the magnetic stress tensor and explicitly use the tensor to describe the shape of liquid-vapour interfaces in magnetic fields. In Sec.3.5 I derive a modified Young-Laplace equation for quasi-static drops in magnetostatic fields and compare this expression to characteristic expressions of other common electro- and magnetohydrodynamic phenomena. In Sec. 3.6 I summarise and conclude this chapter.

3.2 Boundary conditions of the electromagnetic stress tensor

As discussed in Ch. 2, the EMST is not as widely used as other tools to consider the manipulation of fluids in matter. In this section, I therefore provide a brief overview of the fundamental concepts on which the EMST is based. Explicit derivations of the EMST can be found in Ref. [85, 86]. The electromagnetic force belongs to the four fundamental forces (or interactions) in nature, along with the gravitational force, and the strong and weak forces (the nuclear forces that are extremely short-ranged and only relevant on a subatomic scale). The EMST captures the stress on a volume due

to the application of electromagnetic fields.

The road map in Fig. 3.1 highlights the path from the fundamental forces to the electromagnetic stress tensor for (1) macroscopic, (2) non-dissipative interactions of matter or vacuum and (3) static fields:

1. In **macroscopic** systems electromagnetic field strengths can take any positive value including zero, whereas at atomic or molecular scale - where quantum effects are relevant - the lowest allowed field strength is non-zero due to quantum fluctuations.

2. Non-dissipative systems do not exchange matter or energy with their environment and are therefore **thermodynamically closed systems** - the total momentum flux density of field and matter is conserved within the system.

3. In **static fields** - where there are no time-dependent interactions of electromagnetic fields and matter - electric permittivity and magnetic permeability simplify to frequency-independent values, and the moment flux transfer between field and matter is constant - the system is therefore in a quasi-static state.

In the following subsections I discuss these boundary conditions in more detail.

3.2.1 Closed thermodynamic system

A system in equilibrium can be described by properties such as its mass, pressure and volume. When a property of the system is altered, for example if the volume is increased, thermodynamic laws describe how the other properties will change to establish a new equilibrium of the system. To make such predictions about the behaviour of a system I need to understand how its properties are related. In this
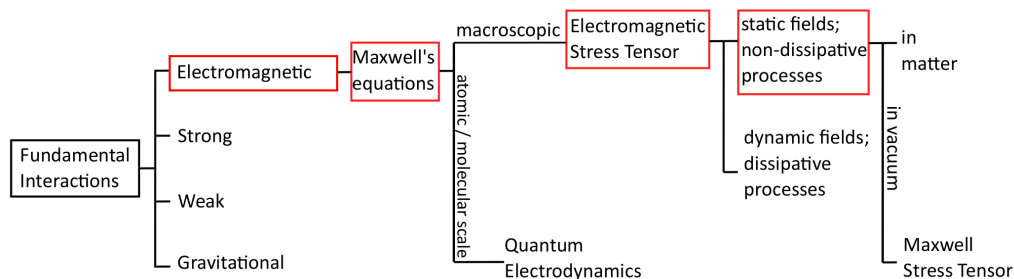
Figure 3.1: Road map from the fundamental forces to the electromagnetic stress tensor. Non-dissipative macroscopic interactions of matter and static electromagnetic fields are captured in the electromagnetic stress tensor (EMST). In vacuum, the electromagnetic stress tensor simplifies to the Maxwell stress tensor (MST).

thesis, I am particularly interested the interaction between a magnetic field and matter and therefore go on to define the thermodynamic potential of such a system. For this discussion I rely on Ref. [85, 78, 86, 84].

The thermodynamic potential U of a system represents its internal energy, which is the energy needed to create the system. The thermodynamic potential is a function of the entropy S and density ρ of the system:

$$dU = T dS + \xi_0 d\rho \tag{3.1}$$

where the temperature T and chemical potential ξ_0 are respectively defined as:

$$T = \frac{\delta U}{\delta S} \tag{3.2}$$

$$\xi_0 = \frac{\delta U}{\delta \rho} \tag{3.3}$$

The chemical potential of a material component is a measure of how the thermodynamic potential of the system changes through a change in the amount of that material component. The expression for the EMST considered in this thesis is valid in a closed thermodynamic system - this is a system that does not exchange energy or matter with its surroundings. The Helmholtz potential holds for closed thermodynamic systems:

$$a = U - TS \tag{3.4}$$

The mass density of the chemical potential of material component α in a closed thermodynamic system is therefore:

$$\xi_\alpha = \frac{\delta a}{\delta \rho_\alpha} \tag{3.5}$$

The thermodynamic potential (total energy) of a closed system is the sum of the energy of field and matter, and can therefore be separated into field-independent (a_0) and field-dependent (a_{em}) terms.

$$a = a_0 + a_{em} \tag{3.6}$$

In the closed system, conservation of total momentum holds, meaning that the sum of the momenta of the electromagnetic field and of the matter in the system is conserved. This law assures the validity of the assumption that the force on a finite volume can be expressed as the force acting on the surface of that volume (the stress on the volume), which is the fundamental concept of the EMST. The EMST is in fact the momentum flux between field and matter. This exchange of momentum causes deformation or transport of the matter - such as in the case of a volume of incompressible fluid in an electromagnetic field.

3.2.2 Macroscopic Maxwell's equations

Maxwell's equations describe static and induced electromagnetic fields and are universally valid - in vacuum and in matter, where bound charges and currents are polarised by the applied electromagnetic fields. Since these bound charge and currents may be difficult to determine, Maxwell's equations are commonly rewritten in terms of free charge and currents. These modified equations are known as macroscopic Maxwell's equations, or Maxwell's equations in matter and include the electric displacement field **D** and the magnetic auxiliary field **H**. The integral and differential forms of Maxwell's equations in matter provide different insights into the interaction of fields and matter. I therefore briefly summarise the two forms of Maxwell's equations below, where I relied on Ref. [4, 5, 85, 87].

Gauss's law states that electrostatic fields originate from electric charges, and the flux of these fields through any closed surface *S*, with surface vector **n** and surface area element *da*, is proportional to the enclosed free electric charge ($q_{f,enc}$).

$$\oint_S \mathbf{D} \cdot \mathbf{n} \, da = q_{f,enc} \tag{3.7}$$

The electric displacement field therefore diverges from positive charges and converges upon negative charges. The divergence of the displacement field is equal to the density of enclosed free electric charge (ρ_f):

$$\nabla \cdot \mathbf{D} = \rho_f \tag{3.8}$$

where the displacement field **D** is defined as the sum of the applied electric field and the polarisation **P** of the matter which it penetrates:

$$\mathbf{D} = \epsilon_0 \mathbf{E} + \mathbf{P} \tag{3.9}$$

While there are positive and electric charges, there are no magnetic monopoles. Gauss's law for magnetic fields therefore does not include free charges and does therefore not change from the definition in vacuum, which states in the integral form that the total magnetic flux passing through any closed surface is zero.

$$\oint_S \mathbf{B} \cdot \mathbf{n} \, da = 0 \tag{3.10}$$

The divergence of the magnetic field at any point is therefore zero.

$$\nabla \cdot \mathbf{B} = 0 \tag{3.11}$$

Faraday's law states that a time-dependent magnetic flux through a surface S, with surface vector $\mathbf{n}$ and surface area element da, induces an electric field along the boundary C, with line element $\mathbf{dl}$, of that surface.

$$\oint_C \mathbf{E} \cdot \mathbf{dl} = -\frac{d}{dt} \int_S \mathbf{B} \cdot \mathbf{n} da \tag{3.12}$$

The induced electric field therefore has a non-zero curl - it circulates back on itself. If the surrounding material is a conductor, then a current is generated by the induced electric field, which in its turn produces a magnetic field opposed to the applied magnetic field.

$$\nabla \times \mathbf{E} = -\frac{\delta \mathbf{B}}{\delta t} \tag{3.13}$$

The Ampere-Maxwell law states that a free electric current $I_{f,enc}$, or a time-dependent electric flux through a surface, induces a magnetic field along the boundary of that surface.

$$\oint_C \mathbf{H} \cdot \mathbf{dl} = I_{f,enc} + \frac{d}{dt} \int_S \mathbf{D} \cdot \mathbf{n} da \tag{3.14}$$

The induced magnetic field therefore has a non-zero curl.

$$\nabla \times \mathbf{H} = \mathbf{J}_{f,enc} + \frac{\delta \mathbf{D}}{\delta t} \tag{3.15}$$

where $J_{f,enc}$ is the current density through the surface S, and $\mathbf{H}$ is defined in terms of the applied field and the magnetisation $\mathbf{M}$, the magnetic dipole moment per unit volume, as:

$$\mathbf{H} = \frac{\mathbf{B}}{\mu_0} - \mathbf{M} \tag{3.16}$$

As mentioned above, the electric displacement field and magnetic auxiliary field are dependent on the polarisation and magnetisation of the material. In linear materials, where the polarisation and magnetisation is uniform, these properties are proportional to the applied field, where the proportionality constant is the electric and magnetic susceptibility of the material, χ_e and χ_m respectively:

$$\mathbf{P} = \epsilon_0 \chi_e \mathbf{E} \tag{3.17}$$

$$\mathbf{M} = \mu_0 \chi_m \mathbf{H} \tag{3.18}$$

Polarisation is an effect that occurs when electric charges are displaced in an electric field, for electric dipoles that align along the field lines of an applied field. Similarly, magnetisation is defined as the alignment of magnetic dipoles - these dipoles originate from the total angular momentum of the atoms (or molecules) composing the material. This thesis only considers materials with linear electromagnetic properties, such that Eq. 3.16 and 3.18 hold for magnetic fields, and Eq. 3.9 and 3.17 for electric

fields. In the following sections, I will briefly discuss the physical origin of magnetisation and polarisation - for a comprehensive treatment of magnetisation I refer the reader to Ref. [4, 87] and of polarisation to Ref. [4, 85].

3.2.3 Magnetisation

Magnetisation of real materials cannot be explained in a classical framework, since the Bohr-van Leeuwen theorem states that in classical systems there is no thermal equilibrium magnetisation [87]. Magnetisation of real materials must therefore be treated in a quantum mechanical framework. In quantum mechanics, the total angular momentum of an atom is the sum of the orbital and spin angular momentum of the electron cloud and the nuclear spin - a negligible contribution in this context. The orbital angular momentum of an electron determines its electronic state and therefore the electron shell it fills, while the spin angular momentum is commonly conceptualised as a rotation of the electron over its own axis.

In atoms that have no unfilled electronic shells the angular momenta cancel out - the atom is diamagnetic ($-1 << \chi_m < 0$), meaning that a magnetic field induces a magnetic moment that opposes the applied magnetic field. The full quantum mechanical argument (for which I refer the reader to Ref. [87]) considers the application of the magnetic field as a perturbation of the Hamiltonian - an expression of the energy of the atom - that includes a diamagnetic and a paramagnetic term - where the latter depends on the total angular momentum. Due to the electronic structure of the diamagnetic material - where the total angular momentum is zero - the paramagnetic term is zero, and only the diamagnetic perturbation remains. The diamagnetic term raises the ground state energy of the material and therefore increases its free energy. Consequently, a diamagnetic material will move out of a magnetic field to minimise its free energy again.

In paramagnetic atoms ($0 < \chi_m << 1$) an electron shell is unfilled, therefore the angular momenta do not cancel and a net magnetic moment remains. In a paramagnetic material, these magnetic moments are small and therefore largely independent - they are oriented in random directions resulting in no net magnetisation of the material. Upon application of a magnetic field however, the magnetic moments align with the applied field, resulting in a net magnetisation of the material which is oriented in the same direction as the applied field. As mentioned above, the amount of magnetisation is proportional to the applied field, and saturates once all angular momenta are aligned.

In ferromagnets ($0 << \chi_m$), magnetic moments are much stronger than in paramagnets and momenta of neighbouring atoms are aligned in parallel due to their interaction with each other. This alignment is usually present over spatial domains,

where atoms in close proximity share the same direction of magnetic moment, but there may be multiple domains present in a piece of material. Upon application of a magnetic field, the magnetic moments in the ferromagnet reorient along the direction of the field. The magnetisation of ferromagnets saturates when all domains are aligned.

The alignment of angular momenta in para- and ferromagnets is temperature dependent, since thermal motion randomises the magnetic moments again. Regarding the perturbation of the Hamiltonian of para- and ferromagnets in magnetic fields, both the diamagnetic and paramagentic terms are non-zero, due to filled and unfilled electron shells respectively. The paramagnetic terms dominate the perturbation, and the free energy of these materials is therefore reduced, leading the materials to move into the magnetic field. Note that the direction of movement of a material exposed to a magnetic field solely depends on the sign of its magnetic susceptibility, and not on the sign of the applied field.

3.2.4 Polarisation

Similarly to the reduction of free energy of para- and ferromagentic materials in magnetic fields, the perturbation of the Hamiltonian of dielectric materials ($0 < \chi_e$) in electric fields also reduces the dielectrics free energy. This reduction in free energy causes dielectrics to move into electric fields. Conceptually, the electron cloud of dielectric materials is polarised in electric fields. The induced dipoles align with the applied field, resulting in a net polarisation in the direction of the applied field. This polarisation is the source of an induced electric field, which opposes the applied field. As mentioned above, the polarisation is proportional to the applied field - the stronger the applied field, the more atoms are polarised. Once the applied field reaches a threshold voltage, known as breakdown voltage, the field ionises the material and the dielectric becomes conducting (such as in the case of a lightning strike, as shown in Fig. 3.4a)).

In conductors ($0 < \chi_e$), an applied electric field induces a current, where free charges move along the field lines to the edges of the conductor. Similarly to the dielectric case, an electric field is induced which opposes the applied electric field. As a result, there is no net electric field in the conductor.
It is noteworthy that while magnetostatic susceptibility can be negative or positive, electrostatic susceptibility in linear materials is always positive [85].

Electromagnetic susceptibilities have frequency-dependent components which are zero in static fields. In non-static fields, these components are non-zero, significantly varying the behaviour of materials in comparison to the static case. These frequency-dependent effects are exploited for many technical applications, such

as the sorting of cells using dielectrophoresis, which is shown in Fig. 3.4b). The utilisation of equivalent frequency-dependent magnetic effects offer a wealth of opportunities for exploration and application development, but exceed the scope of this thesis.

I have now discussed the interaction of electromagnetic fields and matter based on an electromagnetic and quantum dynamic approach. I will use these concepts in the next section to develop an understanding of the stresses acting on a fluid at rest.

3.3   Definition of the stress tensor in a fluid at rest

In the previous section I discussed the boundary conditions of the EMST, including a discussion of the electromagnetic force and how it acts on the volume of a fluid. Here I consider which other forces act on a fluid and express the balance of forces in a fluid at rest in the stress tensor.

3.3.1   Stress balance in a fluid at rest

In a fluid at rest, the forces acting on the fluid must cancel. There are two types of forces acting on a fluid, namely those acting on the volume of the fluid (body forces) and those acting on its surface (surface forces). Body forces include the gravitational and electromagnetic forces. Surface forces include the interfacial force, which arises from the surface tension of the fluid. Both types of forces can be expressed as stresses acting on the interfaces of the fluid, where they must balance is the fluid is at rest. Before discussing this stress balance here, for which I rely on Ref. [88, 89, 84], I briefly introduce some fundamental concepts on interfaces, for which I rely on the comprehensive treatments of this topic in Ref. [88, 90, 89].

Interfaces constitute the boundary between two media. These media may consist of different phases (liquid, gas, solid) or of different material compositions in the same phase. In thermodynamic equilibrium there is a constant and equal exchange of matter and energy between the media which I may ignore in this treatment of interfaces and assume instead, that the interface constitutes a discontinuity of material properties.

While interfaces between fluids and solids are fixed, the interfaces between two fluids can freely move and their shapes are determined by the stresses acting on them.

Using the divergence theorem, the total force F^{tot} acting on a volume V can be expressed as stresses σ_{ij} acting on the surface A of that volume:

$$F_i^{tot} = \oint \sigma_{ij} dA_j = \int \nabla_j \sigma_{ij} dV \tag{3.19}$$

where the force per unit area acting in direction i on a surface element normal to direction j is the stress tensor element σ_{ij}. Of course, since force is the temporal derivative of momentum, σ_{ij} equally describes the i-directed momentum flux through a surface element normal to direction j. In a fluid at rest, only the normal stresses, where $i = j$, are non-zero.

$$\begin{pmatrix} \sigma_{11} & 0 & 0 \\ 0 & \sigma_{22} & 0 \\ 0 & 0 & \sigma_{33} \end{pmatrix}$$

The non-diagonal components of the stress tensor are the tangential stresses, or shearing stresses. These stresses can occur between different layers of fluids in motion but must be zero for a fluid at rest.

In a fluid at rest, the normal stresses across a boundary must cancel:

$$0 = \Delta\sigma_{nn}^{em} + \Delta\sigma_{nn}^{grav} + \Delta\sigma_{nn}^{surf} \tag{3.20}$$

where $\Delta\sigma_{nn}^{em}$ is the electromagnetic, $\Delta\sigma_{nn}^{grav}$ the gravitational, and $\Delta\sigma_{nn}^{surf}$ the interfacial normal stress difference across the interface of a fluid. In the following section I will discuss these stresses.

3.3.2 Electromagnetic stress

Electromagnetic fields exert forces on ions and electric and magnetic dipoles in matter. The electromagnetic force is therefore a body force. Because I consider a closed thermodynamic system (see Sec. 3.2.1), the electromagnetic force can be expressed as a stress acting on the surface of the volume that is penetrated by the electromagnetic fields. The stress acting in direction i on a surface element with surface normal in direction j is the stress tensor element σ_{ij}.

In this thesis, I use the definition of the EMST by Stierstadt and Liu [84, 86], which is valid for time-independent (quasi-static), non-dissipative (closed system) processes:

$$\sigma_{ik} = (U - TS - \xi_\alpha \rho_\alpha - \mathbf{E} \cdot \mathbf{D} - \mathbf{H} \cdot \mathbf{B})\delta_{ik} + E_i D_k + H_i B_k \tag{3.21}$$

where U is the thermodynamic potential, which is the total energy density of matter and field (Jm^{-3}), T is temperature (K), S is the entropy of matter and field ($Jm^{-3}K^{-1}$), ξ_α is the mass density of the chemical potential ($J\,kg^{-1}$) of the material component α, ρ_α is the partial density of the material component α (the total density is $\rho^{tot} = \Sigma_\alpha \rho_\alpha$), **E** is the electric field strength, **D** is the electrical displacement, **H** is the applied (auxiliary) field, **B** is the magnetic flux density, and δ_{ik} is the Kronecker-Delta function.

The definition of the EMST in Eq. 3.21 agrees with the predictions made in the preceding sections, namely (1) the strength of momentum exchange between field and matter is determined by the electric and magnetic susceptibility of the matter and the strength of the applied field; (2) the direction of the stress is solely dependent on the sign of the susceptibility and independent on the sign of the field. The EMST can be adpated for use in a system that is not closed through the addition of dissipative terms [84].

In vacuum, the field-independent term of the thermodynamic potential and any material-dependent contributions in Eq. 3.21 vanish. The EMST reduces to the MST [84]:

$$\sigma_{ik}^{vac} = \epsilon_0 \left(E_i E_k - \frac{1}{2} E^2 \delta_{ik} \right) + \mu_0 \left(H_i H_k - \frac{1}{2} H^2 \delta_{ik} \right) \tag{3.22}$$

3.3.3 Gravitational stress

Gravity is a body force and in the context used here it is due to the gravitation field of the earth and is approximately uniform over the volume of the fluid. If the fluid is of uniform density ρ, then the normal stress $\sigma_n^g n$ on the fluid interface due to gravity increases proportionally with depth z of the fluid in the direction of the gravitational force:

$$\sigma_{nn}^g = -g\rho z \tag{3.23}$$

where g is the gravitational acceleration [84].

3.3.4 Interfacial stress

Interfacial stress is a surface force, which is associated with the surface free energy γ - the energy that is required to move molecules from the interior of a medium to its surface. In thermodynamic equilibrium, there is no excess of molecules at the surface of the medium and the excess free surface energy is therefore minimised. The term 'surface free energy' is commonly used interchangeably with 'surface tension', which is the tension between molecules at the surface of a medium.

Though the surface tension is tensile - it acts along the interface - it is equivalent to a pressure on the interface directed towards the center of curvature, namely the interfacial stress [88]:

$$\sigma_{ij} = \gamma \left(\frac{1}{R_1} + \frac{1}{R_2} \right) \tag{3.24}$$

where R_1 and R_2 are the principal radii of curvature of the interface, as illustrated in Fig. 3.2. The principal radii of curvature of an axisymmetric drop are commonly expressed as [71, 90, 89, 91]:

$$\left(\frac{1}{R_1} + \frac{1}{R_2} \right) = \frac{r''}{(1 + r'^2)^{3/2}} - \frac{1}{r(1 + r'^2)^{1/2}} \tag{3.25}$$

where r(z) is the outline of the interface in the r-z-plane, r' and r'' are the first and second derivatives of r with respect to z. A common example to illustrate this concept is a small water drop in air, where the effects of gravity on the shape of the drop can be neglected. In thermal equilibrium, the excess free surface energy of the drop is minimised when the surface area of the drop is minimised - the drop therefore assumes the shape of a sphere. Since water is an incompressible fluid, the volume of the sphere cannot be further reduced.

In equilibrium, the stress due to internal pressure must balance with interfacial
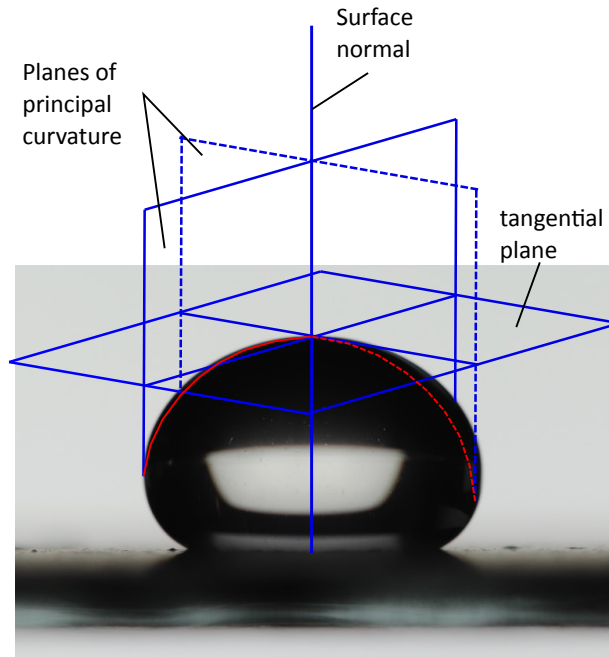
Figure 3.2: Illustration of the planes of principal curvature of a sessile drop. The principal curvatures are the intersections of the principal planes of curvature with the surface of the drop, as indicated in red. The radii associated with these curvatures are the principal radii of curvature which describe the shape of a drop.

stress. This balance is expressed in the Young-Laplace equation - the fundamental equation of capillarity [90]:

$$\Delta P = \gamma \left(\frac{1}{R_1} + \frac{1}{R_2} \right) \tag{3.26}$$

where ΔP is the difference in internal and external pressure and the radii of curvature always originate on the side of the interface with the higher pressure.

For axisymmetric fluid-fluid interfaces, the principal radii of curvature at the apex point must be equal. Eq. 3.26 then becomes:

$$\Delta P = \frac{2\gamma}{b} \tag{3.27}$$

where b is the radius of curvature at the apex point [89]. I have already encountered the stress due to internal pressure in Sec. 3.2.1: the field-independent Helmholtz potential a_0 in Eq. 3.6. I can therefore rewrite Eq. 3.27 as:

$$\Delta P = \Delta a_0 = \frac{2\gamma}{b} \tag{3.28}$$

Since the field-independent Helmholtz potential is included in the EMST, this difference in internal pressure is therefore already included in the electromagnetic normal stress difference across an interface.

3.4 Magnetic stress on a volume of fluid

In this section, I simplify the EMST to the magnetic stress tensor (in the absence of electric fields), and use this tensor to describe the shape of a liquid-vapour interface in a magnetic field.

3.4.1 Definition of the magnetic stress tensor

I simplify the EMST by considering a system in the absence of electric fields:

$$\mathbf{E} = \mathbf{D} = 0 \tag{3.29}$$

The field-dependent (a_{em}) term of the thermodynamic potential is:

$$a_{em} = \int \mathbf{H} \cdot d\mathbf{B} \tag{3.30}$$

$$= \frac{1}{2} \mu_r \mu_0 H^2 \tag{3.31}$$

Since the chemical potential is the derivative of the thermodynamic potential with respect to density, it can also be split into field-independent (ξ_0) and field-dependent (ξ_{em}) terms:

$$\xi_\alpha \rho_\alpha = (\xi_0 + \xi_{em})\rho_\alpha \tag{3.32}$$

$$= \xi_0 \rho_\alpha + \frac{1}{2}\mu_0 H^2 \rho_\alpha \frac{\delta\chi}{\delta\rho_\alpha} \tag{3.33}$$

where I have used the expression for the field-dependent thermodynamic potential in equation 3.31, and the fact that the applied magnetic field **H** is independent of the density of the medium (while the flux density **B** does depend on the density of the medium). Substituting equations 3.4, 3.31 and 3.33 into equation 3.41, I arrive at following expression for the magnetic stress tensor:

$$\sigma_{ij} = \left(a_0 - \xi_0 \rho_\alpha - \frac{1}{2}\mu_0\mu_r H^2 - \frac{1}{2}\mu_0 H^2 \rho_\alpha \frac{\delta\chi}{\delta\rho_\alpha} \right)\delta_{ik} + H_i B_k \tag{3.34}$$

The magnetic stress on a volume is therefore dependent on the magnetic properties of the material and on the shape and orientation (not direction) of the field with respect to the surface of the volume. Therefore, in order to evaluate the EMST acting on a volume, the shape of the surface of the volume needs to be well-defined.

3.4.2 Magnetic stress difference across the liquid-vapour interface

I consider a liquid-vapour interface in the presence of a magnetic field. The applied magnetic field is the vector sum of its normal and tangential components with respect to the surface over which $\Delta\sigma_{nn}^{EM}$ is resolved, $H^2 = H_n^2 + H_t^2$, as shown by Fig. 3.3. The normal component of the applied field is:

$$H_n = H\cos(\phi) \tag{3.35}$$

$$= H\cos\left(\text{atan}\left(\frac{1}{r'}\right)\right) \tag{3.36}$$

$$= H\frac{1}{\sqrt{1 + \frac{1}{r'}}} \tag{3.37}$$

where I used the mathematical identity $\cos(atan(x)) = (1 + x)^{-1/2}$.

In equilibrium, the stresses on the interface of two substances from inside and outside must be equal. I impose the standard boundary conditions for Maxwell's equations [84, 92]: (1) the difference in the magnetic field component tangential to the surface must vanish ($\Delta B_t = \Delta H_t = 0$) in the absence of surface charges or currents; (2) the stress components normal to the interface, σ_{nn}, must be continuous,
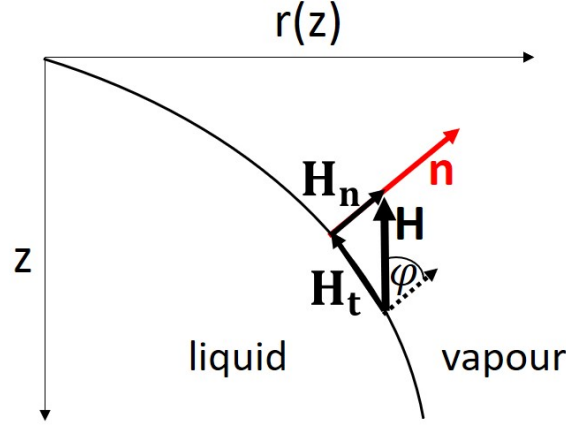
Figure 3.3: Magnetic field components on the liquid-vapour interface. The direction of the applied field H with respect to the liquid-vapour interface $r(z)$ with surface normal n can be defined through a consideration of its normal (H_n) and tangential (H_t) vector components. ϕ is the angle between H and H_n. The directionality of the field with respect to an interface determines the magnetic stress difference across it.

while tangential components cancel. The normal stress at the surface becomes:

$$\sigma_{nn} = a_0 - \xi_0\rho_\alpha - \frac{1}{2}\mu_0\mu_r H^2 - \frac{1}{2}\mu_0 H^2 \rho_\alpha \frac{\delta\chi}{\delta\rho_\alpha} + \mu_0\mu_r H_n^2 \tag{3.38}$$

The vapour phase is air, which I approximate as vacuum in its magnetic properties ($\mu = \mu_0$) as well as in its chemical potential ($\xi_\alpha\rho_\alpha = 0$). Equation 3.38 therefore becomes:

$$\sigma_{nn}^v = a^v - \frac{1}{2}\mu_0 H^2 + \mu_0 H_n^2 \tag{3.39}$$

In the liquid phase, I substitute $a = a^l$ into equation 3.38. The electromagnetic stress difference across the air-liquid boundary is therefore:

$$\Delta\sigma_{nn}^{mag} = \sigma_{nn}^l - \sigma_{nn}^v \tag{3.40}$$

$$= a^l - a^v - \xi_0\rho_\alpha - \frac{1}{2}\mu_0 H^2\left(\chi + \rho_\alpha \frac{\delta\chi}{\delta\rho_\alpha}\right) + \mu_0\chi H_n^2 \tag{3.41}$$

I conclude from Eq. 3.41 that (1) the magnetic stress difference depends on the shape of the interface and its orientation with respect to the applied magnetic field, as well as the magnetic properties of the liquid (χ); (2) the direction of the magnetic stress is independent of the sign of the magnetic field, but is instead determined by the sign of χ; and (3) in a non-uniform magnetic field, the magnitude of $\Delta\sigma_{nn}^{EM}$ varies along the liquid-vapour interface, causing a stronger deformation of the interface in regions of higher magnetic field strength.

3.5 The modified Young-Laplace equation

In the preceding sections, I discussed the forces acting on a fluid at rest, including the electromagnetic force. I discussed the balance of the forces in a fluid at rest is captured in the stress balance at the interface of the fluid. I also discussed how the shape of an interface between two fluids is determined by the stress balance across it. In the remaining sections of this chapter, I use this understanding, to define the shape of a sessile, quasi-static, axisymmetric drop in a magnetic field.

3.5.1 Derivation of the modified Young-Laplace equation

In addition to the magnetic stress difference across the liquid-vapour interface, there is also a gravitational and surface stress difference.

$$\Delta \sigma_{nn}^{surf} = \gamma (R_1^{-1} + R_2^{-1}) \tag{3.42}$$

$$\Delta \sigma_{nn}^{grav} = g \Delta \rho z \tag{3.43}$$

where R_1 and R_2 are the main curvature radii of the interface (m), g is the gravitational acceleration (ms^{-2}), ρ is the mass density (gl^{-1}), and z is the vertical distance from the interface (m) [84, 89].

In equilibrium these stress differences must balance. I substitute the expressions for the magnetic stress difference (Eq. 3.41), the surface stress difference (Eq. 3.42), and the gravitational stress difference (Eq. 3.43) across the liquid-vapour interface into equation (Eq. 3.20) and obtain:

$$0 = \gamma (R_1^{-1} + R_2^{-1}) + g \Delta \rho z + a^l - a^v - \xi_0 \rho_\alpha - \frac{1}{2} \mu_0 H^2 \left(\chi + \rho_\alpha \frac{\delta \chi}{\delta \rho_\alpha} \right) + \mu_0 \chi H_n^2 \tag{3.44}$$

This equation is the modified Young-Laplace equation for a quasi-static drop in a magnetostatic field. Note that this equation holds for ferrofluids and para- and diamagnetic salt solutions and is valid in any time-independent (static) magnetic field. To illustrate the effect of the choice of fluid or field, I will consider a number of limiting cases of equation 3.44.

3.5.2 Limiting case: absence of magnetic fields

In the absence of magnetic fields, **B**=**H**=0, the stress balance of the drop simplifies again to the Young-Laplace equation [90, 89, 91]:

$$0 = \gamma (R_1^{-1} + R_2^{-1}) + g \Delta \rho + (a^l - a^v - \xi_0 \rho_\alpha) \tag{3.45}$$

The equilibrium shape of the liquid-vapour interface is solely affected by the gravitational and hydrostatic forces acting on it.

3.5.3 Limiting case: one-component fluids

In a one-component fluid $\rho_\alpha = \rho$ and $\xi_\alpha = \xi$. Using the Clausius-Mossotti approach, I obtain a relation between the density and the susceptibility of the fluid, which I can approximate as linear for fluids with $\chi << 1$:

$$\rho \frac{\delta \chi}{\delta \rho} = \chi \left(\frac{\chi}{3} + 1 \right) \approx \chi \tag{3.46}$$

Substituting this into equation 3.41 I obtain for the magnetic stress across the interface:

$$\Delta \sigma_{nn}^{mag} = a^l - a^v - \xi_0 \rho + \mu_0 \chi (H_n^2 - H^2) \tag{3.47}$$

$$= a^l - a^v - \xi_0 \rho + \frac{\chi}{\mu_0} B^2 \left(\frac{1}{1 + \frac{1}{r'}} - 1 \right) \tag{3.48}$$

where I used equation 3.37 for H_n and replaced the applied field (**H**) with the magnetic flux density measured in air (**B**). The first three terms in this equation are field-independent energy terms, which are determined through the thermodynamic potential. The sign of the field-dependent term is determined through the prefactor to B_n, which ranges between 0 and 1, since $(0 < \cos(x)^2 < 1)$. Assuming that the sum of the field-independent terms is positive, the magnetic stress difference $\Delta \sigma_{nn}^{em}$ is largest when $B_n = B$, which is true when $r' = 0$.

3.5.4 Transformation to electrohydrodynamic phenomena

The magnetic stress difference expressed in Eq. 3.41 can easily be transformed to an electric stress difference [84]:

$$\mathbf{H} \rightarrow \mathbf{E}$$
$$\mathbf{B} \rightarrow \mathbf{D}$$
$$\mu_0 \rightarrow \epsilon_0$$
$$\chi_m \rightarrow \chi_e \tag{3.49}$$

This means that the extensive body of work on electrostatic phenomena can be transferred to magnetostatic phenomena with some key differences: charge induced fluid circulations limit the validaty of a static stress balance in dielectrics [93, 94] - these circulations are not present in magnetic fluids [71]; natural materials may have a

negative magnetic, but not a negative electric susceptibility. These phenomenological differences make the study of magnetostatic phenomena particularly attractive. Here, I exploit the fact that diamagnetic fluids have a negative magnetic susceptibility to demonstrate the reverse effect to the elongation along the field lines of paramagnetic drops in uniform magnetostatic fields [95] and conducting drops in electrostatic fields [96].

Eq. 3.41 can be used to describe a range of common electrostatic and magnetostatic fluidic phenomena as those discussed in Ch. 2. Stierstadt and Liu [84] have explicitly used the EMST to describe the height-of-rise of a magnetic fluid (Fig. 2.1, Fig. 3.4a)) and the electromagnetic force on a particle in a fluid (Fig. 3.4b)). In section 3.5 I have used the EMST to describe the shape of sessile drops in magnetic fields (Fig. 3.4c)). At rest, the stresses acting in these different experiments must balance. For the measurement of height-of-rise of a liquid column, this is gravitational and electromagnetic stress; for a floating particle it is stress due to the buoyant, gravitational, and electromagnetic forces; for a drop it is the stress due to the interfacial, gravitational, and electromagnetic forces.

The expressions for key parameters of these phenomena are summarised in Table 3.1. These different electro- and magnetohydrodynamic phenomena are commonly treated separately, often as different subjects, such as dielectrophoresis and density measurements in magnetic fluids. The EMST is able to describe all these phenomena and highlight the commonalities between them. The EMST that I employ in this thesis is a third rank tensor - it is defined in the three spatial dimensions. To consider time-dependent processes, the EMST can be defined as a fourth rank tensor - including time as the fourth dimension - where the tensor elements describe not only the flow of momentum, but also the density of the momentum and the flow of energy and density of energy [4]. In vacuum, this results in the Poynting vector, which describes the momentum carried by the electromagnetic field. In time-dependent processes the frequency-dependent nature of susceptibility must also be considered. This frequency-dependence of electric susceptibility is commonly exploited in dielectrophoresis; frequency-dependence of magnetic susceptibility is not as widely studied.
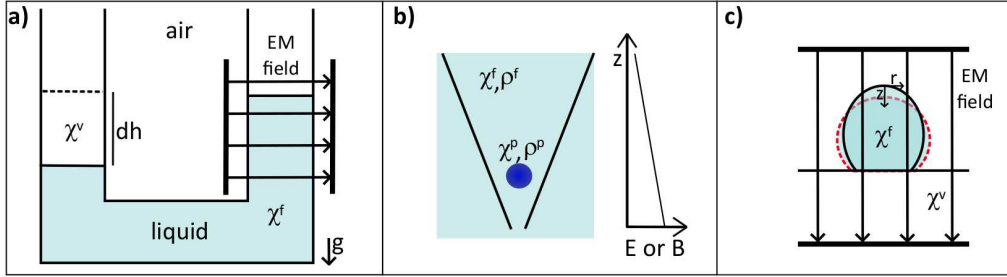
Figure 3.4: Examples of common electro- and magnetohydrodynamic experiments. **(a)** The height of a liquid column in air is raised in an electric or magnetic field, where the electric or magnetic susceptibility of the fluid is $\chi^f > 0$, and χ^v is the susceptibility of air. **(b)** A particle with magnetic susceptibility χ^p and density ρ^p is suspended in a liquid with χ^f and density ρ^f. In a non-uniform electrostatic or magnetostatic field, the electromagnetic force acting on the particle experiences depends on $\chi^p - \chi^f$. **(c)** A drop of a fluid with χ^f in air with χ^v in a uniform electrostatic or magnetostatic field is elongated for $\chi^f > 0$.

Table 3.1: Expressions of key observables of some magnetostatic phenomena in fluids, derived using the electromagnetic stress tensor (Eq. 3.21) [84].

Phenomenon	Characteristic expression	Label
Change in height (Δh) of a liquid column in air	$\Delta h = \mu_0 \chi_m (2\rho g)^{-1} H_t^2$	(3.1.1)
Force (**F**) on particle (p) of volume V_p in fluid (f)	$\mathbf{F} = \mu_0 (\chi_m^p - \chi_m^f) V_p \mathbf{H} \cdot \nabla \mathbf{H}$	(3.1.2)
Shape of a sessile drop in air	$\gamma(R_1^{-1} + R_2^{-1}) = -g\Delta\rho\,z + a_0^l - a_0^v - \xi_0 \rho_\alpha + \mu_0 \chi(H_n^2 - H^2)$	(3.1.3)

3.6   Summary and conclusion

This chapter reviewed the fundamental concepts behind the EMST and presented the derivation of an expression of the shape of a liquid-vapour interface in a magnetostatic field. The EMST is valid for quasi-static, non-dissipative processes and captures the interaction between an electromagnetic field and a fluid. For a fluid at rest this stress must balance with other common stresses acting on fluids, such as gravitational and surface stress. By balancing these stresses an expression of the shape of a liquid-vapour interface in an electromagnetic field can be obtained. This expression can be transformed to electric fields, but in real systems there are differences between the two cases.

In the following chapter I discuss the methods and materials used to experimentally verify this expression.

Chapter 4

Materials and methods

4.1 Introduction

In this Chapter I discuss the fundamental methods and materials used in this thesis for the experimental investigation of the analytical expression obtained in Ch. 3.

The samples are drops of aqueous solutions of salts, which I prepare and characterise as described in Sec. 4.2. In Sec. 4.3 I describe the experimental set-up. The substrates are microscope slides coated in superhydrophobic composite films from colloidal graphite, which I prepare as described in Sec. 4.3.2. The magnetic field is generated by an actuation system, consisting of an electromagnet and a programmable power supply, which I describe in Sec. 4.3.3. The drops are imaged in an image-acquisition system - which I describe in Sec. 4.3.4 - consisting of a backdrop and a remotely-controlled DSLR camera. The images of the drop are analysed using the custom-made program Axisymmetric Drop Shape Analysis in magnetic fields (ADSA-mf), which I developed to extract the outline of the drop and iteratively fit to it the analytical model described in Ch. 3. I describe ADSA-mf in Sec. 4.4. Fig. 4.1 illustrates the components of the experimental method, which I discuss in more detail in this chapter.

The data presented in Fig. 4.3 was obtained in an experiment carried out by Machiel G. Flokstra and myself in the School of Physics and Astronomy, University of St Andrews. I played a major role in the preparation and execution of the experiment, and the data analysis and interpretation are entirely by own work.
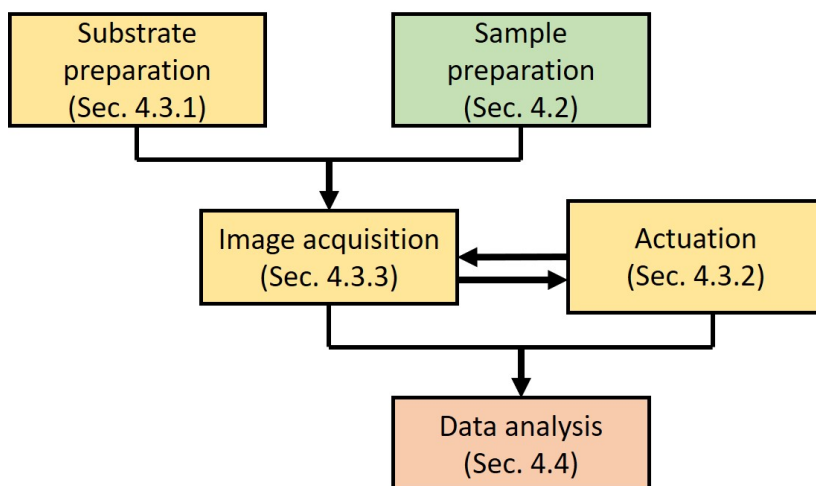
Figure 4.1: Schematic of the experimental method for shaping drops with magnetic fields. The methods include the samples preparation; the experimental set-up, including the substrate preparation, image acquisition, and magnetic actuation; and the data analysis using the custom-made program ADSA-mf. The corresponding sections in the text where these topics are discussed are indicated in the figure.

4.2 Sample specifics and preparation

The drops are aqueous solutions of para- and diamagnetic salts. The paramagnetic salts are manganese chloride tetrahydrate ($MnCl_2 \cdot 4H_2O$, CAS-No.: 13446-34-9) and gadolinium chloride hexahydrate ($Cl_3Gd \cdot 6H_2O$, CAS-No.:13450-84-5). The diamagnetic salts are calcium bromide hydrate ($Br_2Ca \cdot xH_2O$, CAS-No.: 71626-99-8) and sodium sulphate ($NaSO_4$, CAS-No.: 7757-82-6). The salts were sourced from Sigma-Aldrich (Sigma-Aldrich Company Ltd., UK) and their properties and the properties of the DI water are summarised in Table 4.1.

Table 4.1: List of properties of DI water and of diamagnetic salts used in this work.

Substance Name	Formula	M_S g mol^{-1}	χ_m[97] $\times 10^{-6}$cm^{3}mol^{-1}
DI water	H_2O	18.02	−12.63
Manganese chloride tetrahydrate	$MnCl_2 \cdot 4H_2O$	197.9	14350
Gadolinium chloride hexahydrate	$GdCl_3 \cdot 6H_2O$	371.7	27930
Calcium bromide hydrate	$Br_2Ca \cdot xH_2O$	199.89	−73.8
Sodium sulphate	$NaSO_4$	142.04	−52

To dissolve the paramagnetic and diamagnetic salts DI water, I weighed the amount of salt and water required for the desired solution on a microscale. The
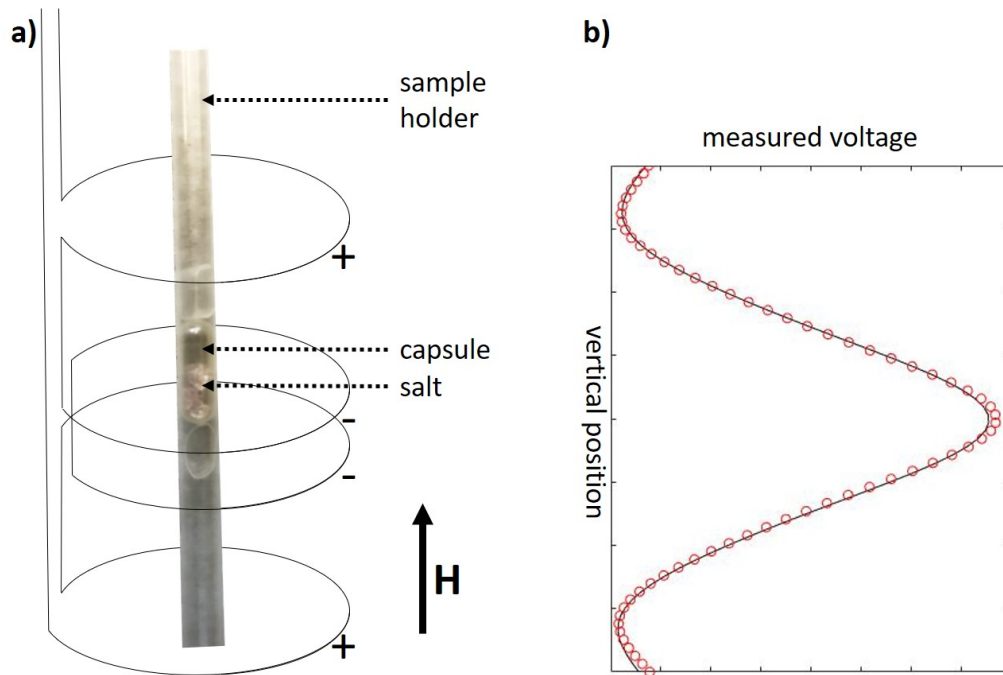
Figure 4.2: Illustration of the detection coils of the Magnetic Property Measurement System (MPMS). The sample is contained in a capsule in a sample holder. A magnetic field **H** is applied to the sample, and the sample is moved by a stepper motor through the detection coils. The coils pick up the induced magnetisation of the sample, which hold information about the magnetic susceptibility of the sample.

DI water is added to the dry chemical and the solution is lightly shaken until completely dissolved. To calculate the magnetic susceptibility of the drop, I use

$$\chi = \rho(\chi_s^m C_s M_s^{-1} + \chi_w^m (1 - C_s) M_w^{-1}) \tag{4.1}$$

where M_s and M_w (kg mol^{-1}) are the molar masses and χ_s^m (m^3 mol^{-1}) and χ_w^m (m^3 mol^{-1}) are the molar magnetic susceptibilities of the diamagnetic salt and water respectively. C_s is the weight concentration of salt in the solution and ρ is the density of the solution.

To confirm the field-independence of magnetic susceptibility over the field range investigated in this thesis, I measured the magnetic susceptibility of dry salt and salt in solution in a Quantum Design's Magnetic Property Measurement System (MPMS). In the MPMS a superconducting magnet applies a magnetic field to a sample, inducing a magnetic moment J:

$$J = \chi H V \tag{4.2}$$

The sample is moved through superconducting detection coils as shown by figure 4.2a). These coils couple inductively into the sample. As the sample moves through the coils, the current induced into the coils changes, which is picked up as a change

in voltage by the detection circuit. An example of such a voltage measurement is shown in figure 4.2b). From this voltage, the total magnetic moment of the sample is calculated, and therefore the magnetic susceptibility of the sample. I placed the samples, contained in polycarbonate capsules (AGC3, Quantum Design), in a sample holder which is inserted into the detection coils of the MPMS. I measured two samples: (1) 41.7 mg of manganese chloride tetrahydrate; and (2) 79 mg of an aqueous solution of $C_s \approx 40\%$ manganese chloride tetrahydrate.
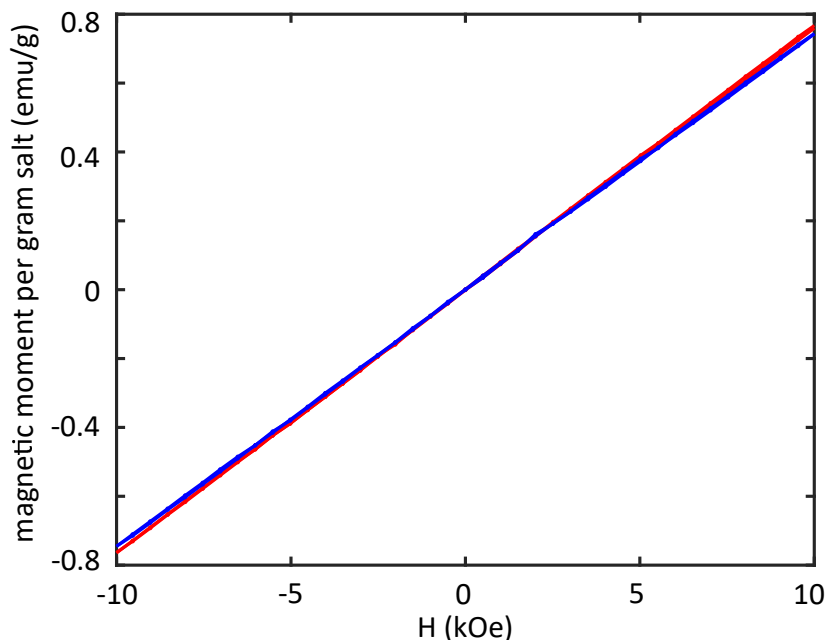
Figure 4.3: MPMS measurement results of the total magnetic moment of dry and dissolved manganese chloride. As expected, the induced magnetisation is proportional to the applied field, meaning that the magnetic susceptibility (the slope) is constant over the applied field range. The data the dry (red) and dissolved (blue) manganese chloride samples overlap, meaning that the magnetic properties of the salt do not change when it is in solution.

The magnetic moment per gram salt (emu/g) is plotted against applied field in Fig. 4.3, for the dry (red) and liquid sample (blue). The magnetic moment per gram salt in both dry and liquid sample is the same, which means that the paramagnetism of the salt is not affected when it is dissolved. From discussion in Chapter 3 this makes sense, because in the salt crystal, the manganese is already ionised and in an ionic bond with chloride. The electronic structure remains therefore the same for manganese in the dry crystal and in solution.

The magnetic moment is linear with applied field, over the range from $H = -10$ kOe to $H = 10$ kOe (-800 kA m^{-1} to 800 kA m^{-1}), which means the susceptibility of the samples is independent of applied field as expected. The slope of the magnetic moment per gram salt in Fig. 4.3 is the magnetic susceptibility. The corresponding

magnetic volume susceptibilities are $\chi_V = 1.5414 \times 10^{-4}$ emu cm^{-3} for the dry sample and $\chi_V = 1.4945 \times 10^{-4}$ emu cm^{-3} for the aqueous solution. The slight difference in value may be due to crystals in the dry sample shifting as the sample is moved through the detection coils, which affects the measured magnetic moment. Using the molar volume V_m of MnCl$_2 \cdot$6H$_2$O ($V_m = M_S/\rho_m$, with $\rho_m = 2.01$ g cm^{-3}), the values of χ_V are converted to molar magnetic susceptibilities $\chi_m = 15176 \times 10^{-6}$ cm^3 mol^{-1} and $\chi = 14714 \times 10^{-6}$ cm^3 mol^{-1} respectively. These measured values are within 15% of the literature value for χ_m, listed in Tab. 4.1.

In conclusion, the MPMS measurements showed that dissolving the salt does not affect its magnetic properties and the susceptibility is independent on the applied field over the field range of interest in this thesis (0 to 1 T).

4.3 Experimental set-up specifics and preparation

4.3.1 Set-up overview

Fig. 4.4 shows the experimental set-up, which consists of superhydrophobic substrates (Sec. 4.3.2), a magnetic actuation system (Sec. 4.3.3) and image acquisition system (Sec.4.3.4). Aqueous sessile drops are exposed to magnetic fields and their shape is measured. An illustration of the experimental set-up to actuate and image a drop in a magnetic field is presented by Fig. 4.4. The drop is imaged on a substrate in a magnetic field. For each measurement, the images and applied currents are saved automatically, and physical drop parameters are saved manually. The data is analysed to extract a relationship between the shape of the drop and the magnetic properties of the system (drop size and susceptibility, applied field). I use the computing environment MATLAB (R2017b, MathWorks) for instrument control, data acquisition and data analysis.
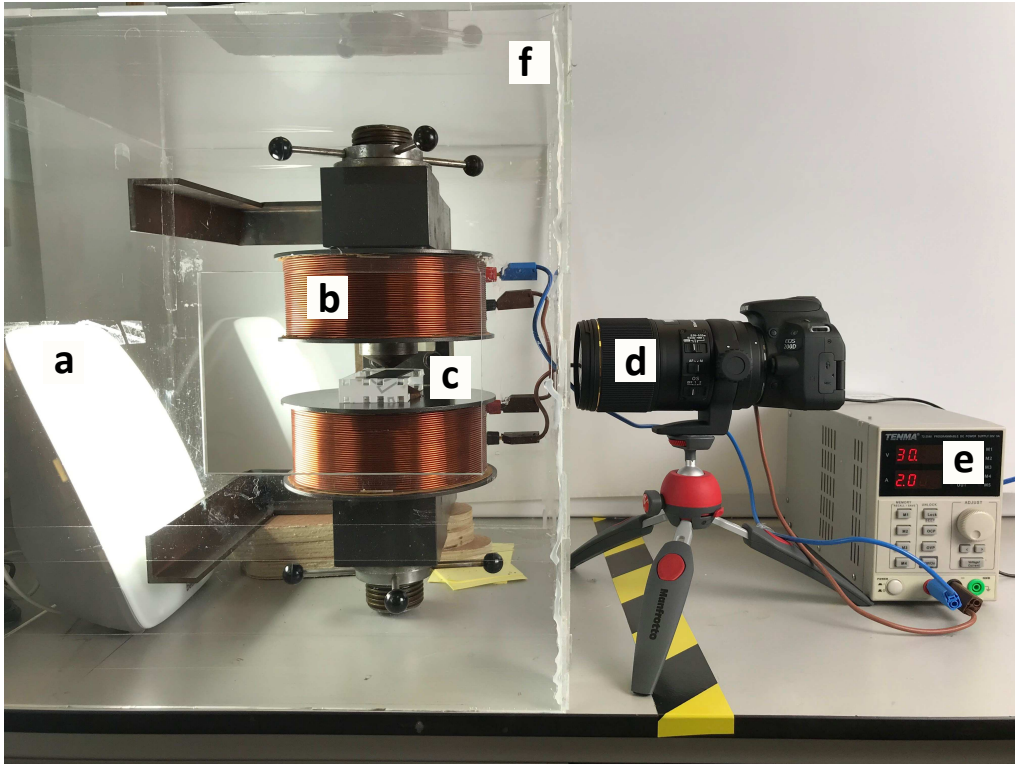
Figure 4.4: Photograph of the experimental set-up to actuate and measure the shape of drops in a homogeneous magnetic field. The drop sits on a substrate in a slide holder (c), subject to the magnetic field generated by the an electromagnet (b). The electromagnet is powered by the programmable DC power supply (e). The drop is backlit by the diffuse light source (a) and imaged by the DSLR camera (d). Both the power supply and the camera are interfaced with a PC through which they are controlled remotely using custom-made software.

4.3.2 Substrates

For the superhydrophobic composite films from colloidal graphite I use Polytetrafluoroethylene powder (Teflon, free-flowing), 1 μm particle size (CAS-No: 9002-84-0, Sigma-Aldrich Company Ltd., UK) and colloidal graphite suspension, sold as Bonderite L-FG ADAG C EU (Henkel, DE). The suspension is a mixture of 20 wt % colloidal graphite particles (CAS-No. 7782-42-5) and 80 wt % aqueous solution of ammonia (CAS-No. 1336-21-6). I also use isopropyl alcohol (IPA, CAS-No. 67-63-0, Sigma Aldrich Company Ltd., UK). I weigh all chemicals using a microbalance and measure volumes of the solutions using a micropipette (10-100 μl, F1-Clip-Tip, Thermo Scientific, UK). I cast the syperhydrophobic coating onto microscope slides with dimensions 76 x 26 x 1 mm (ISO 8037/1, Menzel-Glaeser, Thermo scientific, Germany). To sonicate the teflon powder suspension I use a Fluoreon Ultrasonic Cleaner (https://www.amazon.co.uk/FLOUREON-Ultrasonic-Jewellery-Household-Stainless/dp/B074L2DZZY). To position the substrates correctly within the magnetic field I built an acrylic slide holder using rapid-fabrication techniques.

To fabricate superhydrophobic substrates, I followed the method presented by Bayer *et al.* [98]. I suspended 6 wt % submicron teflon particles in IPA and mixed these with graphite suspension at a teflon-to-graphite ratio of 2. I dispersed the teflon and graphite particles in the mixture by sonicating it for 30-40 minutes. I drop cast the mixture onto the microscope slides, and let the coating dry in ambient conditions before annealing it, by heating the slides to 670 K for 30 s, melting and fusing the teflon particles.

An image of a drop of deionised water on one of these superhydrophobic glass slides is shown by figure 4.5. I measure the contact angle of the drop using the method
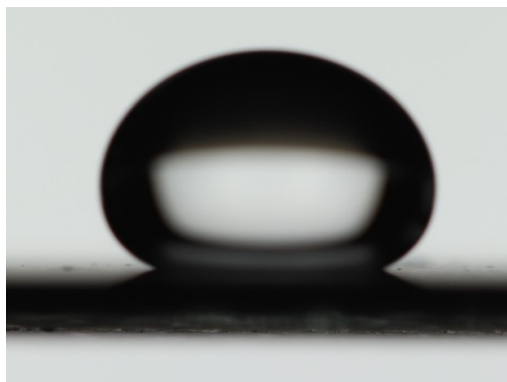
Figure 4.5: Image of a drop of deionised water on a superhydrophobic substrate. The substrate is a glass slide coated with superhydrophobic composite films from colloidal graphite. The contact angle of the drop is $150 \pm 1°$ which is in agreement with the literature value for these substrates [98].

described in section 4.4, and calculate a contact angle of $150 \pm 1°$, which agrees with the findings by Bayer *et al.* [98]. To clean the substrates after usage from residual salt, I rinsed them with hot water and then with DI water.

4.3.3   Actuation system

The actuation system consists of an electromagnet connected to a programmable power supply (72-2540, Digital-Control and Programmable DC Power Supply 30V 3A, Tenma). The power supply is connected through a serial port to a computer, from which I control the output current and voltage through a custom-made program in Matlab. To measure the magnetic field strengths I use a Gauss meter (GM07, Hirst Magnetic Instruments LTD, UK) with a transverse probe.

The electromagnet is a C-frame adjustable electromagnet, illustrated by Fig. 4.6a), consisting of two identical coils that are connected in-series to the power supply. The coils contain 50 mm wide iron cores with 8 mm wide tips. These tips are the magnetic poles. The magnetic flux density is concentrated through the iron cores into a homogeneous field region between the two core tips. The air-gap between the poles is adjustable and affects the field strength and uniformity. As shown by figure 4.6b) the relationship between magnetic field strength (B) and applied current (I) is linear. I analyse this linear relationship between B and I using the MATLAB function 'polyfit', which fits a first-order polynomial (linear function) to the data:

$$B = b_1 I + b_2 \tag{4.3}$$

where b_1 is the slope, and b_2 the off-set (residual field). An example result of this methodology is shown in Fig. 4.6b).
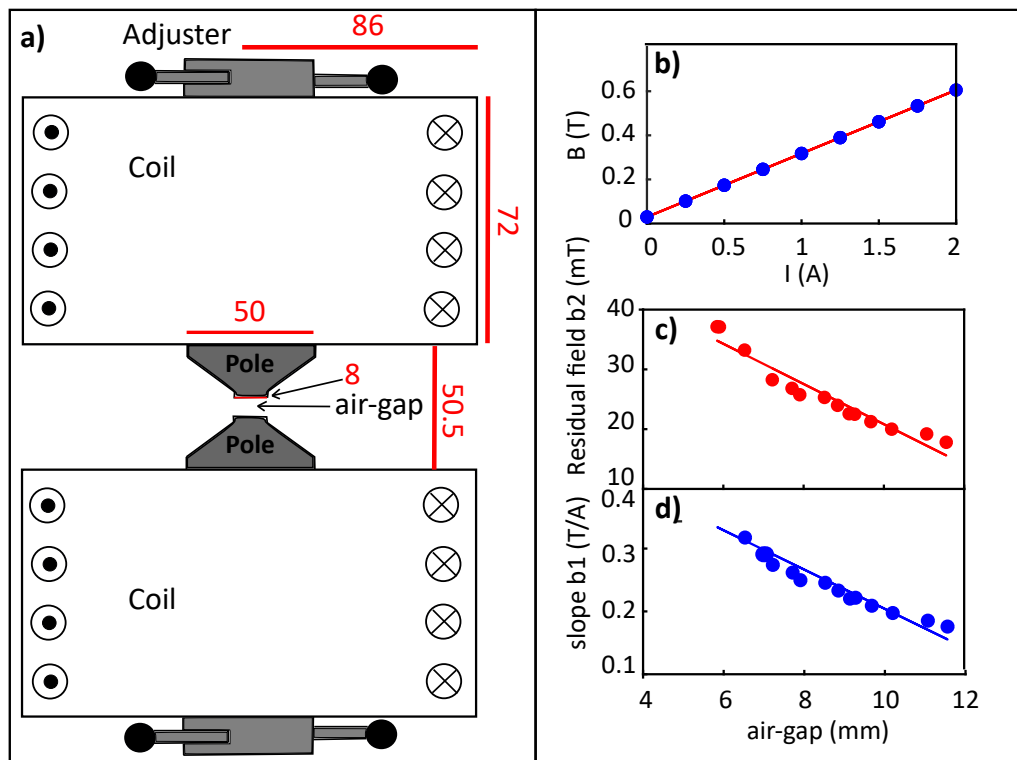
Figure 4.6: Illustration and characterisation of the electromagnet. **a)** Illustration of the electromagnet with dimensions indicated in mm. The distance between the poles is adjustable and affects the field strength between the poles. **b)** The magnetic flux density (B) generated is proportional to the current (I), where the proportionality constant depends on the air-gap between the poles. The data here is shown at an air-gap of 7 mm. **c)** The slope and **d)** residual field as are approximately linear functions with respect to air-gap. These curves can be used to convert current to field strength for a given air-gap.
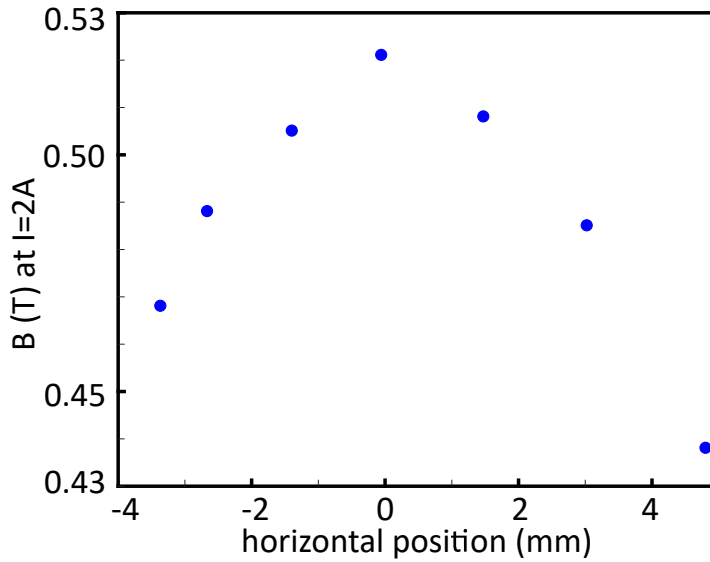
Figure 4.7: Measurement of the spatial uniformity of the electromagnet. A measurement of the z-component of the magnetic field (directed along the cylindrical axis of the coils) at 2 A applied current along the horizontal distance from the centre of the electromagnet, shows that the field decays by roughly 10% over a distance of 4 mm.

I measure this relationship for a range of air-gaps and find that the values of b_1 and b_2 are approximately proportional to the value of the air-gap d. To analyse these relationships I use again the MATLAB function 'polyfit' to obtain the slopes m_1 and m_2, and linear off-set c_1 and c_2 associated with the linear relations between the air-gap and b_1 and b_1 respectively.

$$b_1 = m_1 d + c_1 \tag{4.4}$$

$$b_2 = m_2 d + c_2 \tag{4.5}$$

In the homogeneous field region of the magnet, the values for the slopes and offsets are:

$$m_1 = -31.3 \quad \text{TA}^{-1}\text{m}^{-1} \tag{4.6}$$

$$c_1 = 0.5 \quad \text{TA}^{-1} \tag{4.7}$$

$$m_2 = -3.4 \quad \text{Tm}^{-1} \tag{4.8}$$

$$c_2 = 0.05 \quad \text{T} \tag{4.9}$$

To determine the uniformity of the magnetic field in the homogeneous field region, I measured the magnetic field generated by $I = 2$ A at an air-gap of 8 mm over the horizontal length of the homogeneous field region. The horizontal position is zero where it coincides with the cylindrical axis of the magnet. The results of this methodology are shown in Fig. 6.9. The field decreases by ≈ 10 % over the

58

homogeneous field region. This relative drop in field strength increases slightly with decreasing air-gap. The magnetic field decreases with distance to the cylindrical axis of the magnet to 50% at ≈ 2 cm distance and vanishes at ≈ 6 cm distance.

4.3.4 Image acquisition system

To take photographs of the drop, I position a DSLR camera (Canon EOS 200D, Canon, The Netherlands) with a 150 mm macro lens (Sigma 150 mm f 2.8 EX DG OS HSM Macro Lens) on a table-top tripod (Manfrotto PIXI EVO Tripod). As a backdrop for imaging the drop, I use a diffuse light source (SAD lamp, Beurer, Germany). I connect the camera to a computer through a USB port and automated the image acquisition by interfacing the camera with a custom-made MATLAB program through the free software package 'digiCamControl' (http://digicamcontrol.com/). The custom-made MATLAB program sets the current on the power supply and takes photographs of the drop. The value of the current and timing between photographs can be adjusted.

4.4 Axisymmetric Drop Shape Analysis in magnetic fields (ADSA-mf)

4.4.1 Overview of key features

To analyse the shape of a sessile drop in an electromagnetic field, I developed an algorithm that is similar to the standard Axisymmetric Drop Shape Analysis (ADSA) [70]. ADSA algorithms exploit the fact that the shape of a drop depends on the balance of surface tension and external forces acting on the drop, such as gravity. This force balance is expressed in the Young-Laplace equation. In the presence of electromagnetic fields, the Young-Laplace equation is modified to account for the forces acting on the drop due to these applied fields (Eq. 3.44), as we have shown in the previous chapter (Ch. 3). In this section I describe the algorithm that I developed to analyse drops using this modified Young-Laplace equation - Axisymmetric Drop Shape Analysis in magnetic fields (ADSA-mf). The code for ADSA-mf is available at https://github.com/jdodoo/Thesis.

In ADSA-mf, the outline of the liquid-vapour interface is measured on side-profile images of the drop. The modified Young-Laplace equation (Eq. 3.44) is iteratively fitted to the outline of the drop and the solid-liquid contact angle of the drop is measured.

Figure 4.8 illustrates the side-profile of an aqueous drop, indicating some features that are processed by ADSA-mf (inputs) to obtain unknown parameters (outputs).

The inputs to ADSA-mf include parameters of the drop (mass density and salt concentration), of the liquid-vapour interface (shape of the outline), and of the external forces applied to the drop (gravity and the direction of the magnetic field and current applied to the electromagnet). The direction and magnitude of the gravitational force is constant for the location of the experiment; and the magnetic field is uniform and directed along z, with a magnitude set by the current applied to the electromagnet.

The inputs to ADSA-mf are listed here:

- one side-profile photograph of the drop per current value applied to the electromagnet (JPEG loaded into MATLAB as 8-Bit unsigned integer array)

- value of the current applied to the electromagnet I(A)

- concentration by weight of the salt in the drop C_s

- volume of the drop V (l)

- molecular weight of the salt M_s ($g\,mol^{-1}$)

- molar magnetic susceptibility of the salt χ_s^m ($m^3 mol^{-1}$)

- estimated density of the drop ρ (kgm^3)
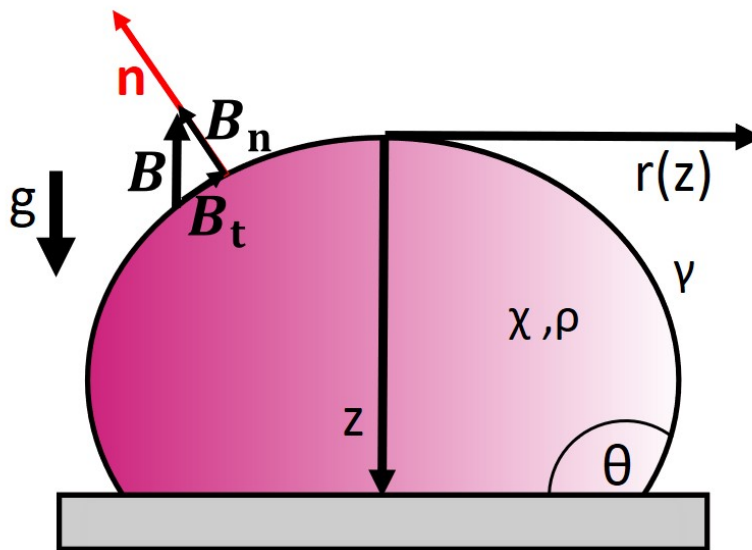
Figure 4.8: Illustration of a sessile drop on a hydrophobic substrate. The outline of the liquid-vapour interface of the drop with mass density ρ and magnetic susceptibility χ is defined in the r-z-coordinate system and contact angle θ. γ is the surface tension of the liquid-vapour interface, g is the gravitational acceleration, n is the surface normal, B is the applied magnetic field which can be split into vector components tangential and normal to the surface (B_n and B_t respectively).

- initial guess of the surface tension of the drop γ (Nm^{-1})

- physical constants: permeability of free space $\mu_0 = 1.2566 \times 10^{-6}$ (NA^{-2}); density of water at room temperature $\rho_w = 0.99 \times 10^3$ (kg m^{-3}); magnetic susceptibility of water $\chi_w = -12.96 \times 10^{-6}$ (cm^{3}mol^{-1}); molecular weight of water $M_w = 18.02 \times 1E-3$ (kg mol^{-1}).

The surface tension is an unknown parameter that is determined in ADSA-mf (output) by analysing the drop profile. The profile of the drop is analysed using the modified Young-Laplace equation, which is derived in Ch. 3 and is an expression of the balance of the stress differences across the liquid-vapour interface due to surface tension, gravity and the applied magnetic field. The stress due to surface tension depends on the surface tension of the drop; the stress due to gravity depends on the gravitational acceleration, the mass density of the drop; the magnetic stress depends on the magnetic susceptibility of the drop, the strength and direction of the applied magnetic field, and the pressure difference between vapour and liquid phase. The stresses vary along the outline of the drop, where the stress due to surface tension varies curvature; the gravitational stress varies with z; and the magnetic stress varies with the normal component of the applied magnetic field with respect to the outline of the drop.

The modified Young-Laplace equation is solved iteratively along the outline of the drop where the optimisation parameter is - in the absence of electromagnetic fields - the surface tension; and - in the presence of electromagnetic fields - the field-independent chemical potential. The contact angle θ is measured by fitting polynomials to the section of the drop close to the contact line.

The parameters that are obtained in this algorithm (outputs) are listed here:

- magnetic field strength B (T)

- pixel-to-distance ration p2m (m)

- outline of the liquid-vapour interface (lv-outline) and of the solid-liquid interface (sl-outline) (pixel)

- apex point of the drop (pixel)

- left- and right-hand-side outlines (pixel) of the liquid-vapour interface

- left and right contact angle of the drop (degrees)

- r-z-coordinates of the outline of the left- and right-hand-side outlines

- radius-of-curvature at the apex point, b (m)

- r-coordinates of the fitted outline r_{fit}

- goodness-of-fit (chi-squared-value) associated with r_{fit}

- numerical apex point and the associated error

- numerical chemical potential and the associated error

- numerical surface tension at zero applied field γ (Nm^{-1}) and the associated error

The radius-of-curvature at the apex point is a parameter that is commonly used to describe the shape of an axisymmetric drop [89, 91]. As discussed in Sec. 3.3.4 it holds information about the field-independent thermodynamic potential of the drop. These computational functions used in ADSA-mf to process the inputs and obtain corresponding *outputs* are:

- 'calculate susceptibility': C_s, M_s, χ_s^m and ρ are inputs to Eq. 4.1, which calculates the *susceptibility χ* of the drop.

- 'magnetic field module' (Sec. 4.4.3): The current (I) and one photograph of the drop are inputs to the magnetic field module, where the *magnetic field strength (B)* is determined, and the conversion factor from pixels on the drop image to real distance (*p2m*) is calculated.

- 'extract drop outline' (Sec. 4.4.4): the drop images are input to this function, where the images are cropped and the outlines of the liquid-vapour interface (*lv-outline*) and of the solid-liquid interface (*sl-outline*) are found. The *apex point* of the drop is extracted from the lv-outline, which is split at the apex point into left- and right-hand-side outlines. The pixel coordinates of the left- and right-hand-side outlines are transformed to *r-z-coordinates*, with the apex point at (0,0) and unique z-values.

- 'iterative fitting of parabolic functions to the outline' (Sec. 4.4.5): the lv-outline and the r-z-coordinates are inputs to this function, where parabolic functions are iteratively fit to (1) the lv-outline around the apex point where the *radius of curvature at the apex point (b)* is measured; (2) the bottom of the left- and right-hand-side outlines to determine the left and right *contact angles* of the drop.

- 'iterative fitting of the Young-Laplace equation to the outline' (Sec. 4.4.6): r-z-coordinates, b, p2m, B, χ, ρ, γ and the physical constants are inputs to this function. The numerical model of the lv-outline is obtained from the Young-Laplace equation, which is solved for r(z). This expression for r(z) is iteratively fit to the r-z-coordinates of the left- and right-hand-side outlines separately
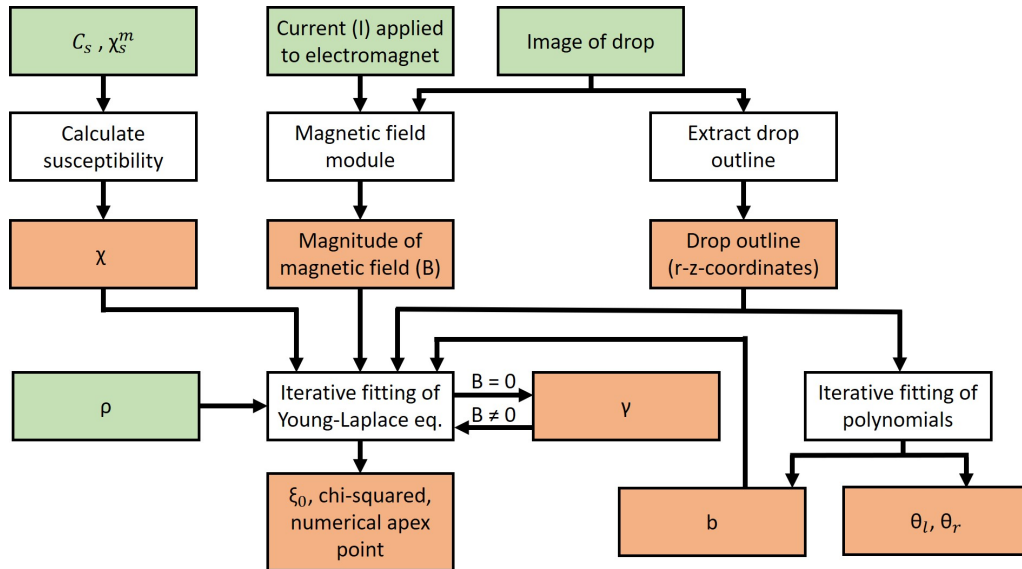
Figure 4.9: Flow chart of the Axisymmetric Drop Shape Analysis (ADSA-mf). This algorithm analyses the shape of a drop in a magnetic field. The inputs to the algorithm (green boxes) are processed by the computational functions (white boxes) to outputs (brown boxes).

and the fitted r-coordinates are obtained (r_{fit}), where the goodness of fit is described in the *chi-square-value*. The *numerical apex point*, the *numerical surface tension* γ at zero applied field, and the *numerical chemical potential* are optimised in the fit and the *errors of the optimised parameters* are obtained.

Figure 4.9 presents a flow chart of ADSA-mf, highlighting the inputs and outputs of the computational functions of the algorithm. The iterative fit routine that I use to fit the polynomials and the Young-Laplace equation is the Levenberg-Marquardt (LM) method - a standard technique to solve non-linear least-square problems, i.e. problems that are not linear in their parameters.

In the following subsections I discuss the methodology used in the iterative fit routine and the computational functions that process the inputs of ADSA-mf to obtain the desired outputs.

4.4.2 Levenberg-Marquardt method

The LM method is a numerical fit routine for non-linear least-square problems [99]. The LM method is commonly used in ADSA, with the benefit that it requires considerably less computation time than other iterative fit routines commonly used in ADSA, such as the Nelder-Mead simplex method [70]. To obtain good fits with the LM method, a good initial guess of the fit parameters is required (close to the optimal value of the fitted parameter). Since I am able to produce good initial guesses of the

fit parameters for the polynomial and Young-Laplace functions, I am using the LM method.

In the LM method, the sum of the weighted residual between a fitted function $y_f(x;\mathbf{a})$ and a set of measured data $y(x_i)$ is minimised, where x is the independent variable and $\mathbf{a}$ is a vector of n parameters. The sum of weighted residuals is defined as:

$$\chi^2(\mathbf{a}) = \frac{1}{2} \sum_{i=1}^{m} \left(\frac{y(x_i) - y_f(x_i;\mathbf{a})}{w_i} \right)^2 \tag{4.10}$$

where w_i is the weighing parameter that is dependent on the measurement error on $y(x_i)$ [99] and m is the number of data points. The χ^2-value, or *chi-squared value*, is a measure of the goodness of fit. The goal of the LM method is to minimise the χ^2-value. This minimisation is achieved by iteratively perturbing the fit parameters $\mathbf{a}$ and re-evaluating the χ^2-value for each perturbation. The minimisation terminates when a predetermined threshold is reached. In the here presented implementation of the LM method, this threshold is reached if the improvement of χ^2 between two subsequent iterations is smaller than 1×10^{-4}.

Fig. 4.10 shows a demonstration of the LM method for the optimisation of a polynomial fit function to the apex of a drop. The optimisation occurs over three
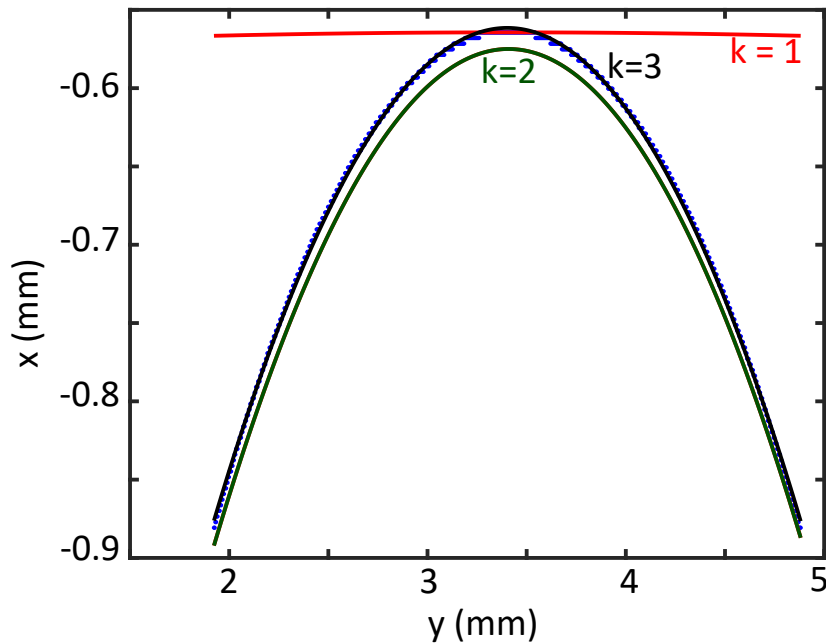
Figure 4.10: Demonstration of the Levenberg-Marquardt method for optimising a polynomial fit function to the apex of a drop. The data set is shown as blue dots, the fit function is optimised over three iterations (k). Over three iterations the fit function is optimised to have good agreement with the data.

iterations (k). The fit function is:

$$y_f = a_3 + a_2 x + a_1 x^2 \qquad (4.11)$$

The corresponding parameters **a** are:

k	χ^2	$\mathbf{a_1}$	$\mathbf{a_2}$	$\mathbf{a_3}$
1	108	1	0.0034	0.0006
2	3.61	143.79	0.0034	0.0006
3	0.079	143.88	0.0034	0.0006

The initial guesses of the parameters **a** are:

$$a_1 = 1$$
$$a_2 = \frac{y(10) - y(1)}{x(10) - x(1)}$$
$$a_3 = y(1)$$

In this example, all parameters **a** can be freely perturbed. In the implementation of the LM method used for this thesis, the freedom to change a parameter can be restricted by (i) restricting the range over which the parameter can be changed; and (ii) forbidding a perturbation to the parameter entirely. This feature is particularly useful for fitting the modified Young-Laplace equation to a real drop, where I want to restrict parameters to remain physically plausible.

4.4.3 Magnetic field module

In the magnetic field module, I calculate the applied magnetic field strength using an image of the drop and magnetic poles, and the values of the applied current. In the image, I measure the pixel distance between the magnetic poles manually using the MATLAB function 'imtool'. I measure: (i) the diameter of the tip of the top pole; (ii) the distance between the poles.

From (i) the measurement of the diameter of the top pole I calculate a conversion factor, p2m (m pixel^{-1}):

$$p2m = \frac{d_{real}}{d_{image}} \qquad (4.12)$$

where d_{image} (pixels) is the diameter on the image, and $d_{real} = 8 \times 10^{-3}$ m is the real diameter of the top pole. The conversion factor is multiplied with a distance on the image to convert it to a real distance.

I use this conversion factor to convert the measurements on the image of (ii) the distance between the poles. I then use the calibration curve in figure 4.6c) to calculate the conversion factor between applied current and generated magnetic field strength corresponding to the measured air-gap as described in Sec. 4.3. To quantify the error on the converted values, I use the standard error of the magnetic field strength values over a data set with the same air-gap between the magnetic poles and same applied current.

4.4.4   Extract drop outline

To measure the outline of the liquid-vapour interface of a drop, I follow these steps:

1. First, I crop the first frame, using the MATLAB function 'imcrop', to the region covering the drop from the contact line to just above apex point. The coordinates of the cropped region of the first frame are used to automatically crop all other frames.

2. Next, I convert the video to a binary image using the MATLAB function 'imbinarize' with adaptive thresholding. I manually adjust the sensitivity of the thresholding using a custom-made GUI. The same sensitivity is used on all frames.

3. Using the MATLAB function 'bwconvhull' I identify the drop as an object and find the outline of the drop using the MATLAB function 'bwboundaries'. The outline is expressed as a two-dimensional matrix, representing horizontal and vertical coordinates (here referred to as y and x). The error on these coordinates is estimated to be 2 pixel, due to random fluctuations in the lighting, which is equal to $\approx 7\,\mu$m for an image with a p2m ratio of 3.5 μm per pixel. This error on the detected outline is similar to the error on the detected outline in common ADSA techniques (20 μm) [70].

The drop outline is split into two parts: the liquid-solid (ls) and liquid-vapour (lv). The ls-outline is equal to the diameter of the triple contact line. The lv-outline is split further into left- and right-hand-side outlines which join at the apex point, the highest point of the drop. For the iterative fitting of the Young-Laplace equation to the outline, the coordinates describing the outline need to be unique in x. The y-x-coordinates of the left- and right-hand-side outlines are therefore separately converted to r-z-coordinates:

$$y \longleftrightarrow r \tag{4.13}$$

$$x \longleftrightarrow z \tag{4.14}$$

where (0,0) is defined at the apex point and only unique values of x are considered, resulting in a set of unique z-coordinates. The y-coordinates corresponding to a set of x-coordinates with the same value are averaged to obtain the r-coordinate associated with the unique z-coordinate. The error associated with the r-coordinate is the standard error, which is inversely proportional to the square root of the number of y-coordinates that have been averaged to obtain the z-coordinate. Fig. 4.11 illustrates how the y-x-coordinates of pixels from the outline of the liquid-vapour interface are converted to r-z-coordinates.
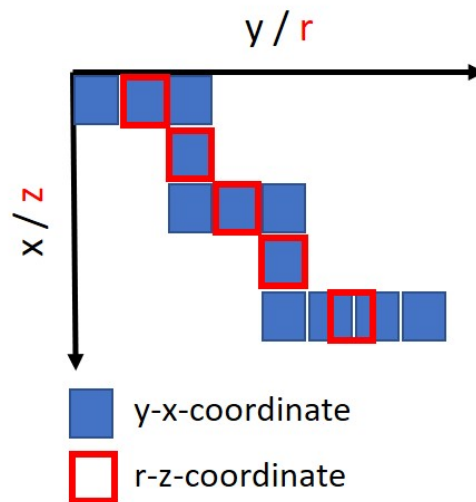
Figure 4.11: Illustration of the conversion of y-x-coordinates of pixels from the outline of the liquid-vapour interface to r-z-coordinates. The pixel coordinates (x-y) are converted to r-z-coordinates by selecting unique x-coordinates and averaging the y-values corresponding to x-coordinates with the same value. The error on the averaged values is weighted by the number of values that are averaged. The error is therefore lowest on the parts of the outline that are flattening off towards the r-axis, such as at the top and bottom of the drop.

4.4.5   Iterative fitting of parabolic functions to the outline

Parabolic functions are iteratively fitted to (i) the apex of the drop, to determine the radius of curvature at the apex point; (ii) the lower sections of the left- and right-hand side of the outline of the drop separately, to measure the left and right contact angles that the drop forms with the substrate. The data sets to be fitted are comprised of (i) the x-y-coordinates of the lv-outline in the range of 95-100% of the height of the drop; (ii) the r-z-coordinates of the lv-outline in the range of 0-10% of the height of the drop.

The parabolic fit function is:

$$y_f = a_3 + a_2 x + a_1 x^2 \tag{4.15}$$

where a_1, a_2, and a_3 are the parameters of the fit function, and x is the independent variable. The fit function is optimised using the Levenberg-Marquardt method as described in Sec. 4.4.2.

An example result of (i), the fit of a y_f to the apex of a drop, is shown in Sec. 4.4.2. The radius of curvature at the apex point (b) is subsequently calculated from the
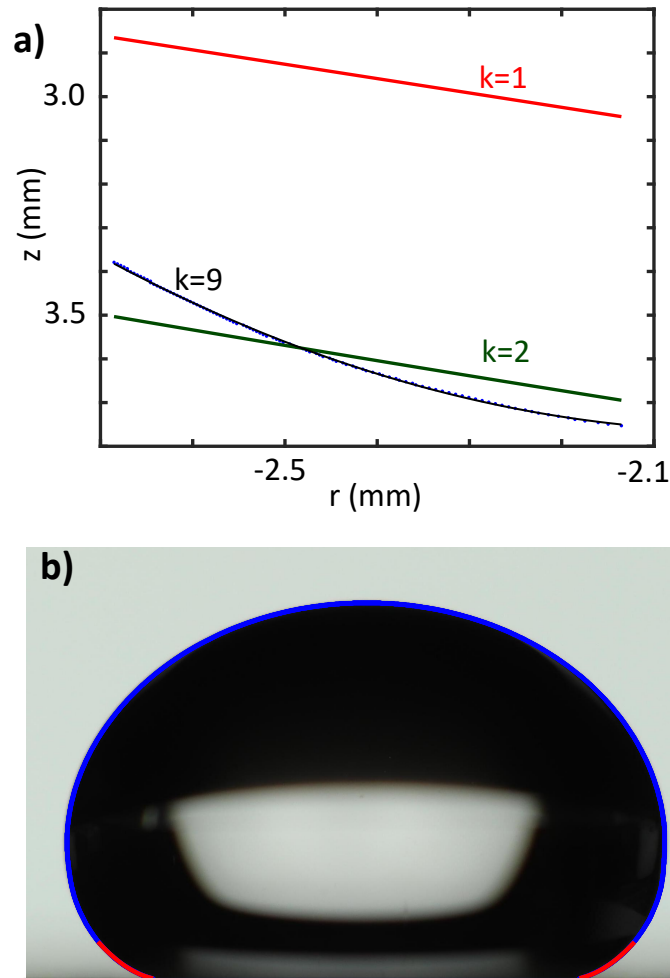
Figure 4.12: Example results of the polynomial fits to the left and right lower half of the drop for contact angle measurement. **a)** The fit function is optimised to the lower left hand side of the drop (blue dots) over 9 iterations (k) using the LM method. **b)** The outline (blue) and fitted polynomial functions (red) are plotted on an image of the drop. The fit shows good agreement with the outline of the drop.

optimised parameters of the fit function:

$$b = \frac{\left(1 + \left(\frac{dy}{dx}\right)^2\right)^{3/2}}{\left|\frac{d^2y}{dx^2}\right|} \tag{4.16}$$

where $\frac{dy}{dx} = a_2 + 2a_1 x_0$, with x_0 the value of the independent variable at the apex, and $\frac{d^2y}{dx^2} = 2a_1$. The radius of curvature at the apex point for the example shown in Fig. 4.10, calculated using Eq. 4.16 is $b = 3.5$ mm.

An example result of (ii), fit of y_f to the left and right lower half of the r-z-coordinates of the drop, is shown in Fig. 4.12. The iterative optimisation of the fit function by the LM method is shown in Fig. 4.12a), where the parameters **a** of y_f are optimised over 9 iterations:

k	χ^2	a_1	a_2	a_3
1	377	1	-0.333	0.0038
2	35.8	-21.52	-0.244	0.0043
9	0.0038	-809.589	3.2336	0.0005

The optimised fit functions are plotted on a photograph of the drop in Fig. 4.12b). The contact angle θ is calculated for the left and right hand side separately:

$$\theta = 180° - (\mathrm{atan}(a_2 + 2a_1 x(1))\frac{180}{\pi} \tag{4.17}$$

The results for the contact angles of the here presented drop are $\theta_{left} = \theta_{right} = 167° \pm 1°$.

4.4.6   Iterative fitting of the Young-Laplace equation to the outline

The modified Young-Laplace equation (Eq. 3.20) is iteratively fit to the r-z-coordinates of outline of the drop (i.e. to the left- and right hand side of the drop separately):

$$0 = \Delta\sigma_{nn}^{surf} + \Delta\sigma_{nn}^{grav} + \Delta\sigma_{nn}^{EM}$$

where the magnetic stress is valid for a one-component fluid (Eq. 3.48), and we use the stresses due to surface tension and gravity as defined in Eq. 3.42 and Eq. 3.43

respectively:

$$\Delta\sigma^{em}_{nn} = \frac{2\gamma}{b} - \xi_0\rho + \frac{\chi}{\mu_0}B^2\left(\frac{1}{1+\frac{1}{r'}} - 1\right)$$

$$\Delta\sigma^{surf}_{nn} = \gamma\frac{r''}{(1+r'^2)^{3/2}} - \frac{1}{r(1+r'^2)^{1/2}}$$

$$\Delta\sigma^{grav}_{nn} = g\Delta\rho\, z$$

where we have substituted $a^l - a^v = 2\gamma/b$, which is valid for an axisymmetric drop. The expression of the principle radii of curvature is a non-linear second order differential equation which must be solved numerically. To solve this equation for r(z), I use the MATLAB function ODE45, which is based on the Runge-Kutta method and requires the equation to be rewritten as a set of linear differential equations:

$$\frac{dr}{dz} = r' \tag{4.18}$$

$$\frac{d^2r}{dz^2} = \left(1 + r'^2\right)^{3/2}\left(\left(r + r_0^f\right)^{-1}\left(1 + r'^2\right)^{-1/2} - \left(\Delta\sigma^{grav}_{nn} - \Delta\sigma^{em}_{nn}\right)\gamma^{-1}\right) \tag{4.19}$$

where I introduced r_0^f as a parameter that adjusts the numerical apex point. The numerical apex point $r + r_0^f$ accounts for some asymmetry in the shape and deformation of the drop. While the ideal drop for this problem is perfectly axisymmetric, the real drop is not. Asymmetry in the shape of the drop is introduced due to inhomogeneous surface roughness, manual levelling of the substrate and magnet, manual centring of the drop in the magnetic field, inhomogeneities in the magnetic field profile.

The function ODE45 evaluates the fit function in each iteration of the LM method. The parameters are iteratively perturbed as described in the previous sections. The initial value of r (r-value of the coordinate of the triple-contact-point) and the initial slope (slope of the r-z-coordinates close to the triple-contact point) are required inputs to the ODE45 solver and are free parameters in the iterative fit routine. Other free parameters in the iterative fit routine are the surface tension γ_0 at zero applied field, and the field-independent chemical potential ξ_0. To achieve good fits, γ_0 is optimised for a drop at zero applied field when ξ_0 is kept constant at 0; and ξ_0 is optimised in the presence of a magnetic field.

An example result of this methodology is presented by Fig. 4.13 where the Young-Laplace equation is iteratively fit to the left hand side outline of a drop. There is no magnetic field applied to the drop, therefore the surface tension is freely optimised. The optimisation of the fit equation takes place over 27 iterations:

k	χ^2	r_{tcl}	r'_{tcl}	r_0^f	γ_0
1	9344	0.021	3	0	72.8 Nm^{-1}
27	0.0675	0.022	2.477	-8.7×10^{-5}	69.6 Nm^{-1}
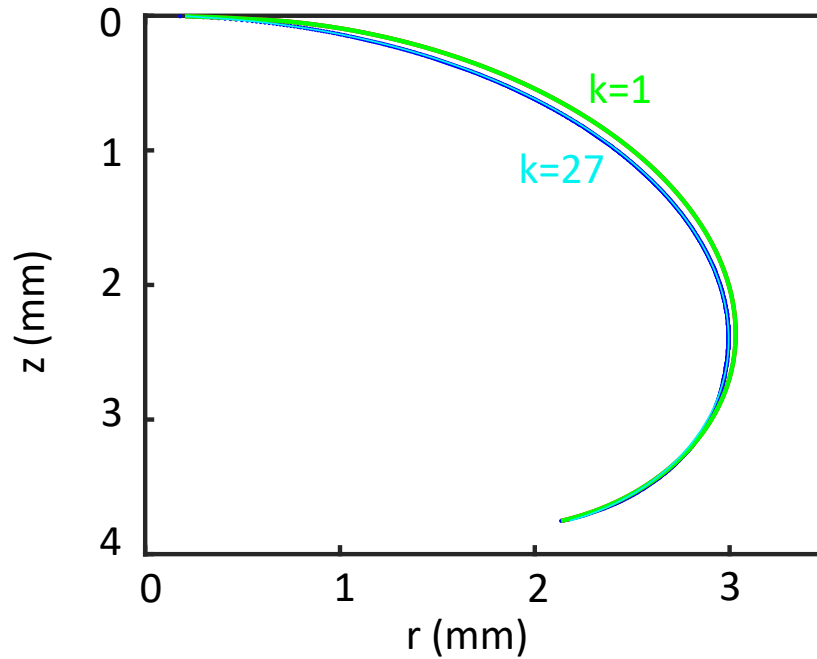
Figure 4.13: Example results of the optimised solutions of the Young-Laplace equation, plotted onto the left-hand-side (mirrored along z-axis) of the outline of the liquid-vapour interface of a drop in the absence of a magnetic field. The fit function is optimised over 27 iterations after which it shows good agreement with the outline.

The optimised value of γ_0 for this drop is subsequently used for the same drop in the presence of magnetic fields as a fixed parameter. The error on γ_0 is determined by the errors on the estimates of the other parameters used in the fit equation. Particularly in the estimation of physical properties of the drop significant errors may be introduced, such as in the density of the drop.

4.5 Summary and conclusion

This chapter introduced the experimental set-up used in this thesis to measure the shape of a drop in a homogeneous magnetic field. The drops that are aqueous solutions of paramagnetic and diamagnetic salts. Samples of a paramagnetic salt have been characterised in an MPMS to confirm the linear relationship between induced magnetisation and applied field. This relationship is not affected by the state of the salt (dry or dissolved).

The experimental set-up consists of superhydrophobic substrates, and actuation system and an image acquisition system. The superhydrophobic substrates are prepared from colloidal graphite. The actuation system consists of an electromagnet that is powered by a DC power supply, where the relationship between applied current

and magnetic field strength is linear. The proportionality factor and linear off-set (residual field) depend on the air-gap between the magnetic poles. The field is directed perpendicular to the surface of the magnetic poles and is strongest in the centre between the magnetic cores. The image acquisition system consists of a DSLR camera and a diffuse light source. With the image acquisition system, side-profile photographs are taken of the drop.

In the custom-made program Axisymmetric Drop Shape Analysis in magnetic fields (ADSA-mf) the shape of the drops is measured and analysed using the theory described in Ch. 3.

In the following chapter I use these materials and methods on shaping drops with magnetic fields.

Chapter 5

Shaping drops with magnetic fields

5.1 Introduction

In this chapter, I explore experimentally how drops are shaped with magnetic fields and compare these results to the theoretical predictions made in Ch. 3.

In Sec. 5.2, I describe the experimental design for the shaping and transporting of magnetic drops. The corresponding experimental methods are described in Sec. 5.3, and include the methods discussed in Ch. 4. In Sec. 5.4.1, I present and discuss the results to shaping of a paramagnetic drop with a magnetic field. For this, I shape the drop with magnetic fields of varying strengths, and analyse how the field strengths relate to the shape of the drop. I then explore the scaling of the shaping for drops with different volumes and susceptibilities, including negative susceptibility (diamagnetic) (Sec. 5.4.2). I discuss the use of dimensionless parameters in Sec.5.4.3, such as the magnetic bond number, which is the ratio of magnetic to surface energy. In Sec. 5.4.4 I present and discuss the transporting of drops with magnetic fields, and confirm that paramagnetic drops are attracted into and diamagnetic drops repelled from a magnetic field. In Sec. 5.5 I summarise the findings of this chapter.

The work presented in this chapter on paramagnetic drops, was jointly conceived by myself, Glen McHale, and Adam A. Stokes. I was responsible for all experimental and analytical work and interpretation of the results. Glen McHale contributed to discussions. Adam A. Stokes provided project supervision.

5.2 Experimental design for shaping drops with magnetic fields

To confirm the predictions on the shape of para- and diamagnetic drops made in Ch. 3, I demonstrate and analyse here the shaping and transport of drops with

magnetic fields. These predictions were (i) that paramagnetic drops are subjected to an outward-directed, and (ii) diamagnetic drops to an inward-directed magnetic stress difference across the liquid-vapour interface. Due to (i), paramagnetic drops should elongate along the field lines of a uniform magnetic field, and be attracted into the highest magnetic field region of a non-uniform magnetic field. Due to (ii), diamagnetic drops should shorten along the field lines of a uniform magnetic field and be repelled form the region of highest magnetic field strength of a non-uniform magnetic field. To test the validity of the modified Young-Laplace equation derived in Ch. 3, I fit the equation to the outlines of drops. Since the expression for the modified Young-Laplace equation is valid for axisymmetric drops, I deform the drops axisymmetrically using a uniform magnetic field as illustrated by Fig. 5.1a).

To demonstrate transport of a drop, a non-axisymmetric stress needs to be applied to the drop, such that the drop deforms more towards one side, causing transport of the drop. To induce this non-axisymmetric stress, I apply a non-uniform magnetic field to the drop, as illustrated by Fig. 5.1b). Since I cannot analyse the shape of the drop using the modified Young-Laplace equation due to the non-axisymmetric deformation of the drop, I measure instead the position of the centre-of-mass (CM) of the drop as a function of applied field.

In these experiments, I use aqueous solutions of para- and diamagnetic salts, which allow me to tune the susceptibility of the drop by varying the salt concentration. To actuate the drops, I use an electromagnet, which allows me to set the magnetic field strength through the applied current. I can therefore obtain statistically relevant sample sizes of the shape of the drop at different applied magnetic field strengths.

I neglect here any effects of electric fields on the drop. This is because in the present set-up I apply a maximum of 30 V to the coils of the electromagnet. The elongation of a drop due to electric stress, as shown in Fig. 2.5, requires a homogeneous electric field across the drop of $\approx 10^5 \, \text{V m}^{-1}$. Since neither the direction nor the strength of the electric field applied to the electromagnet fulfil these requirements, I assume that the deformation of the drop is solely due to a change in magnetic stress.

5.3 Experimental method for shaping drops with magnetic fields

5.3.1 Experimental set-up and salt solutions

I use the set-up described in Sec. 4.3. Side-profile photographs of the drop are taken on which the shape (r(z) in Fig. 5.1a)) and the position of the centre of mass (CM in Fig. 5.1b)) of the drops is measured for the shaping and transport experiments
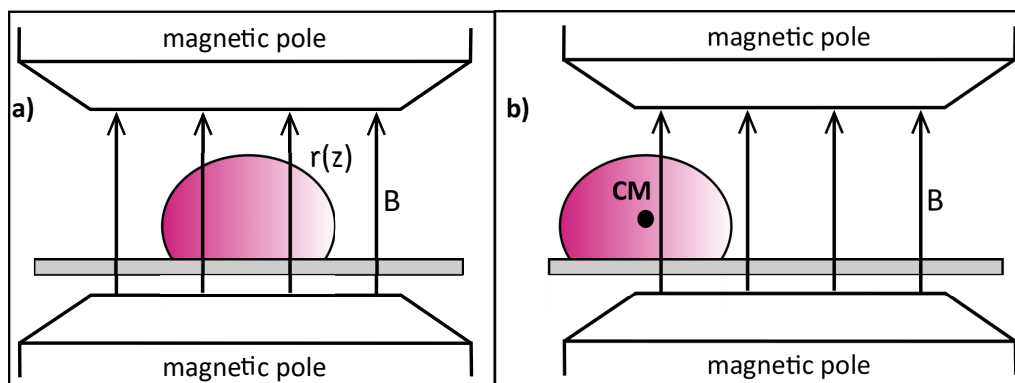
Figure 5.1: Schematic of an aqueous drop on a hydrophobic substrate between two magnetic poles. **a)** In the homogeneous region of the magnetic field **B**, the shape of the drop r(z) is measured. **b)** In the inhomogeneous magnetic field region, the position of the centre of mass (CM) of the drop is measured.

Table 5.1: Para- and diamagnetic salt solutions (with salt concentration C_s, and magnetic susceptibility χ) used for shaping (S) and transport (T) measurements.

Salt Formula	C_s (%ppw)	$\chi \times 10^{-6}$	Experiment
$MnCl_2 \cdot 4H_2O$	35.6	321	S
	27.4	245	T
	17.8	156	S
$GdCl_3 \cdot 6H_2O$	51.0	524	S
$Br_2Ca \cdot xH_2O$	55.8	−7.82	S
$NaSO_4$	15.7	−8.27	S& T

respectively. The magnetic field strength is set through the remotely controlled power supply that provides a current to the electromagnet. The properties of the para- and diamagnetic salts used here are listed in Sec. 4.2. The concentrations and corresponding susceptibilities of the salt solutions used in this chapter are listed in table 5.1.

5.3.2   Shaping drops with magnetic fields

I measure the shape of a drop in the homogeneous magnetic field region, as illustrated in Fig. 5.1. To better understand the effects of different parameters on the shape of the drop, I vary the volume (40-100 µl) and magnetic susceptibility of the drop, the type of salt used in the aqueous solution comprising the drop; and measure over a range of magnetic field strengths, from 0 to 0.6 T. I use three paramagnetic (35.6% ppw

and 17.8% ppw $MnCl_2 \cdot 4H_2O$, and 51.4% ppw $GdCl_3 \cdot 6H_2O$) and two diamagnetic salt solutions (55.8% ppw $Br_2Ca \cdot xH_2O$ 15.7% ppw $NaSO_4$).

To analyse the shape of the drops I use the ADSA-mf algorithm described in Sec. 4.4, where I numerically fit the modified Young-Laplace equation (Eq. 3.44) to the outline of the drop, as described in Sec. 4.4.6. The modified Young-Laplace equation describes the balance of hydrostatic, gravitational, and magnetic stresses on the liquid-vapour boundary. For a axisymmetric drop consisting of a one-component fluid the modified Young-Laplace equation is:

$$0 = \frac{2\gamma}{b} - \xi_0 \rho + \frac{\chi}{\mu_0} B^2 \left(\frac{1}{1 + \frac{1}{r'}} - 1 \right) + \gamma \frac{r''}{(1 + r'^2)^{3/2}} - \frac{1}{r(1 + r'^2)^{1/2}} + g \Delta \rho z \qquad (5.1)$$

where γ is the surface tension of the liquid-vapour interface (N m^{-1}), b is the radius of curvature at the apex point (m), ξ_0 is the field-independent chemical potential of the liquid (J kg^{-1}), ρ is the mass density of the liquid (kg m^{-3}), χ is the magnetic susceptibility of the liquid, μ_0 is the vacuum permeability, B is the applied magnetic field (T), r' and r'' are the first and second derivative of r w.r.t. z respectively, g is the gravitational acceleration (m s^{-2}), and $\Delta \rho$ is the difference in density between liquid and vapour (kg m^{-3}).

To obtain good fits of Eq. 5.1 to r(z) of (i) the drop in the absence of magnetic fields: the density of the solutions ρ is estimated to be equal to the density of water ($\rho_w = 997$ kgm^{-3}) and 1.1 times the density of water for the $MnCl_2 \cdot 4H_2O$ and $GdCl_3 \cdot 6H_2O$ solutions respectively and γ is allowed to freely change; and (ii) the drop in the presence of magnetic fields: $\xi_0 \rho_\alpha$ is allowed to freely change. This numerical optimisation of physical values accounts for errors in the estimates of (i) the surface tension and density of the drop; and (ii) the value of the field-independent chemical potential and the value of the difference of the field-independent thermodynamic potentials of liquid and vapour phase ($a_0^l - a_0^v$). The uncertainty on the $a_0^l - a_0^v$ value is caused by a non-axisymmetric deformation of the drop, due to systematic errors such as inhomogeneties in the applied field and in the roughness of the substrate, and the coarseness of the manual levelling of the substrate and magnet.

To measure the radius of curvature at the apex point, a parabolic function is fit to r(z) in the range where Eq. (5.1) vanishes. The contact angles of the left and right side of the drop is measured independently by fitting second-order polynomials to the outline of the drop close to the triple contact line.

5.3.3 Transporting drops with magnetic fields

To actuate the drops in a non-uniform magnetic field, I place the drops outside the homogeneous magnetic field region. I use 100 µl paramagnetic drops consisting of

an aqueous solution of 27.4% $MnCl_2 \cdot 4H_2O$ (see Tab. 5.1) and 300 µl diamagnetic drops consisting of an aqueous solution of 55.8% $Br_2Ca \cdot xH_2O$.

To analyse the transport of the drop in the non-uniform magnetic field, I measure the position of the centre-of-mass as a function of applied field. I assume that the density of the drop is uniform over the volume of the drop. Therefore I define the centre-of-mass as the point along the symmetry axis of the drop that splits the drop into two regions with equal volume.

5.4 Results and discussion

5.4.1 Shaping drops with magnetic fields

In Fig. 5.2, images of a 60 µl drop of an aqueous solution with 51.4% ppw $GdCl_3 \cdot 6H_2O$ are presented at different applied field strengths. The applied field is increased in strength from 0 to 0.6 T and then decreased back to 0 T in steps of 0.05 T. Each image has been taken once the drop has settled into a quasi-static state, which is after 2s (see Sec. 4.3.3). The following QR code links to a video of this elongation, where the solution of the modified Young-Laplace equation (Eq. 5.1) is plotted onto the image of the drop.

Elongation of a paramagnetic drop in a uniform magnetic field
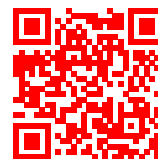
In the absence of a magnetic field, the shape of the drop is a semi-sphere compressed along the direction of gravity. The shape is determined by the balance of the difference in stresses due to surface tension and gravity, and the field-dependent terms in the modified Young-Laplace equation (Eq. 5.1) therefore vanish. The optimised solution of Eq. 5.1 is plotted in red onto the image of the drop, and runs smoothly along the outline, showing that the equation describes the shape of the drop well. The optimised numerical value of the surface tension of the drop in absence of a magnetic field is $\gamma =$66.7 mN m^{-1}. The optimised surface tension is $\approx 8\%$ smaller than that of water (72.8 mN m^{-1}), accounting for errors in the initial guesses of the numerical values of density and surface tension. As the field strength is increased, the drop visibly elongates along the field lines - the height increases and the width decreases. The diameter of the triple contact line of the drop does not change visibly as the drop is elongated. The optimised solution of Eq. 5.1 runs smoothly along the outline of the elongated drop, but diverges slightly at the triple contact line. This effect occurs because (1) Eq. 5.1 does not account for friction between the drop and

77

the substrate, but instead assumes that the contact line can move freely; and (2) the triple contact points of the left and right hand side of the drop are free parameters in the optimisation protocol of Eq. 5.1 (see Sec. 4.4) to account for a not perfectly axisymmetric real drop.
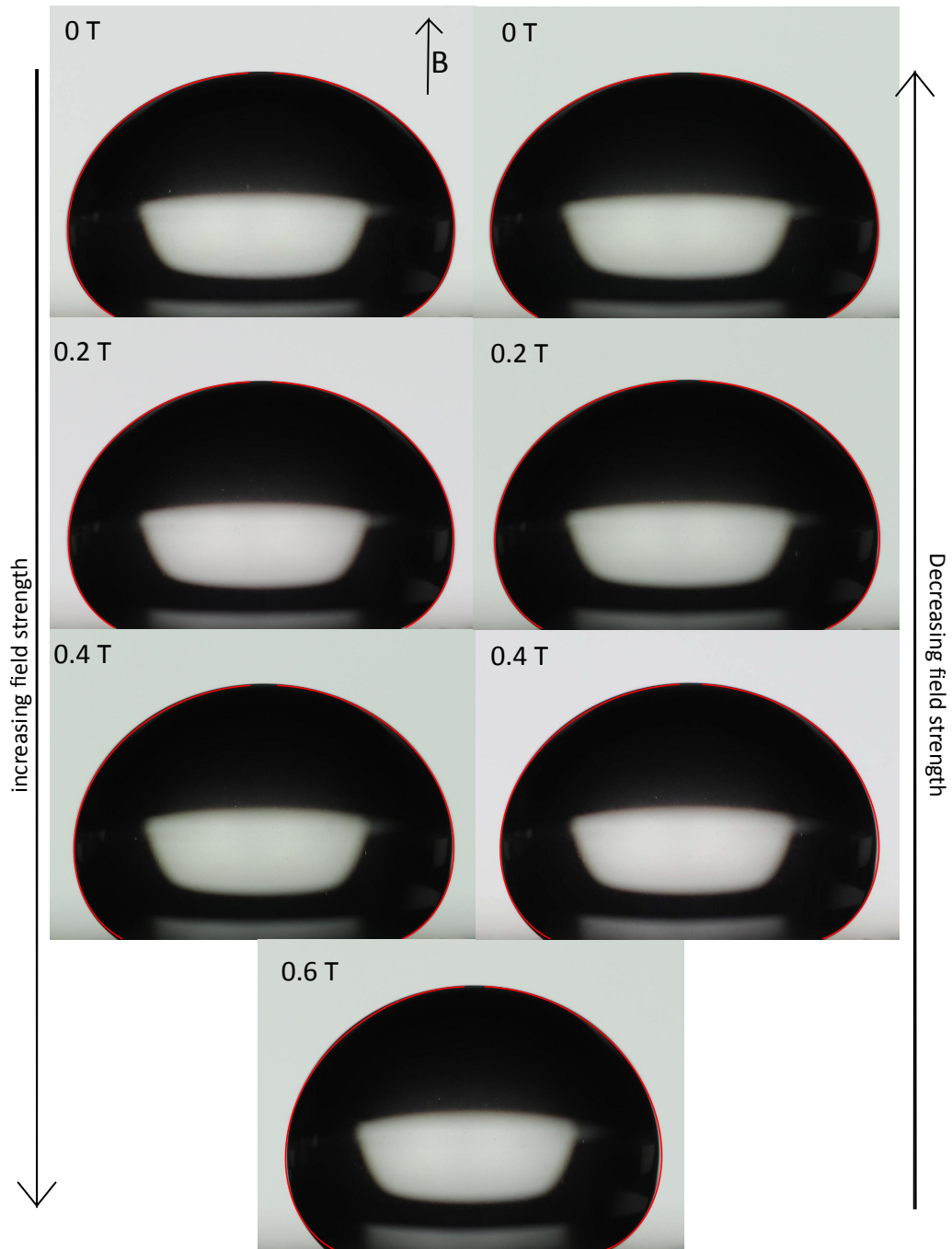
Figure 5.2: Images of a 60 µl drop of 51.4% ppw GdCl$_3 \cdot 6$H$_2$O) are shown as the applied magnetic field is increased from 0 to 0.6 T and decreased again to 0 T. There is no hysteresis visible in the deformation of the drop between increasing and decreasing field scans. The optimised solutions of the modified Young-Laplace equation are plotted onto the images and follow the outlines of the drops well, but diverge slightly at the contact line of the deformed drops at 0.4 and 0.6 T. This is due to the lack of friction in the fit equation, which is present in the real system.

The contact line of the numerical fit and of the real drop are plotted against applied field in Fig. 5.3a). While the contact line of the numerical fit reduces from ≈4.05 to 3.75 mm, the contact line of the real drop only reduces from ≈ 3.95 to 3.90 mm.

As the field strength is decreased, the elongation of the drop lessens until the drop resumes its equilibrium shape in the absence of a magnetic field at 0 T. There is no hysteresis visible in the shape of the drop between the increasing and decreasing field scans. This suggests that no net magnetisation is retained in the paramagnetic solution once the magnetic field is removed.

In the presence of a magnetic field, the field-independent chemical potential ξ_0 is optimised by the fitting algorithm. The numerically optimised ξ_0 is plotted against applied field in Fig. 5.3b). After an initial increase in magnitude of ξ_0 the value settles at $\approx -1.3 \times 10^{-3}$ J kg^{-1}. The initial increase in value is not a real field-dependence of ξ_0, but instead an effect of the fitting routine. The magnetic stress, in which ξ_0
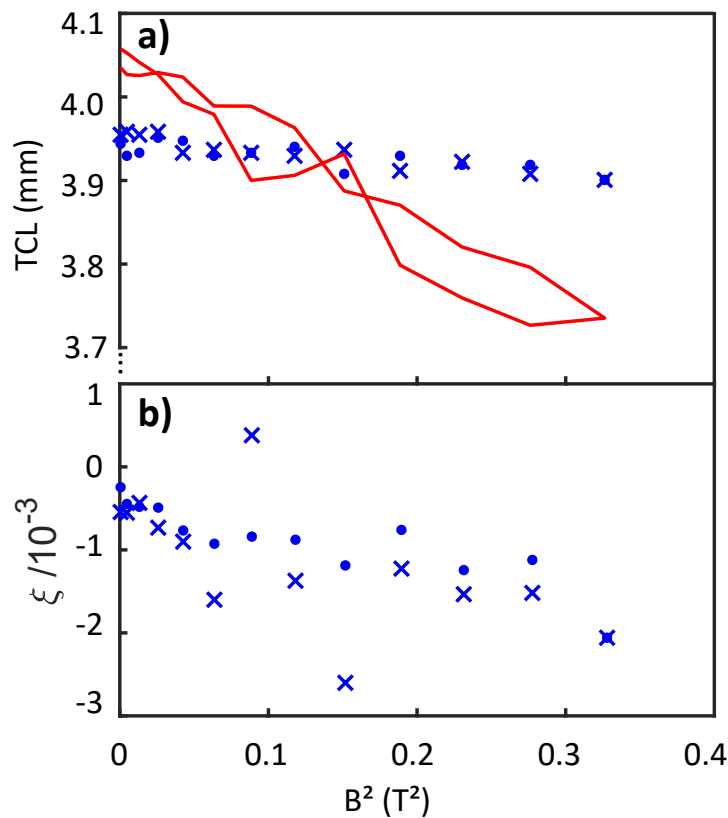
Figure 5.3: Evolution of the numerical values of the diameter of the triple contact line and of the field-independent chemical potential (ξ) during deformation of the drop presented by Fig. 5.2. **a)** The numerical contact line (red) diverges from the real contact line (blue), due to a lack of friction in the numerical model. **b)** Numerical values of the field-independent chemical potential are, as expected, independent of the applied field.

is contained, is zero or negligible at very small applied fields, and becomes increasingly dominant in the stress balance with increasing field strength. The numerically optimisation of ξ_0 therefore becomes more accurate with increasing field strength.

To characterise the elongation of the drop in Fig. 5.2, the height, width and contact angle are shown as a function of applied field by Fig. 5.4. In the absence of a magnetic field, the drop has a height of 3.4 mm and a width of 5.5 mm and a contact angle of 160°. As the field strength is increased to 0.6 T, and the drop elongates along the field lines, the height increases to 3.7 mm, the width decreases to 5.24 mm, and the contact angle decreases to 149°. The changes in height, width and contact angle are linear with B^2. There is some noise visible in the measured data, originating from physical sources (vibrations induced in the drop from the laboratory environment), and from the grayscale to binary image conversion which introduces a random error caused by
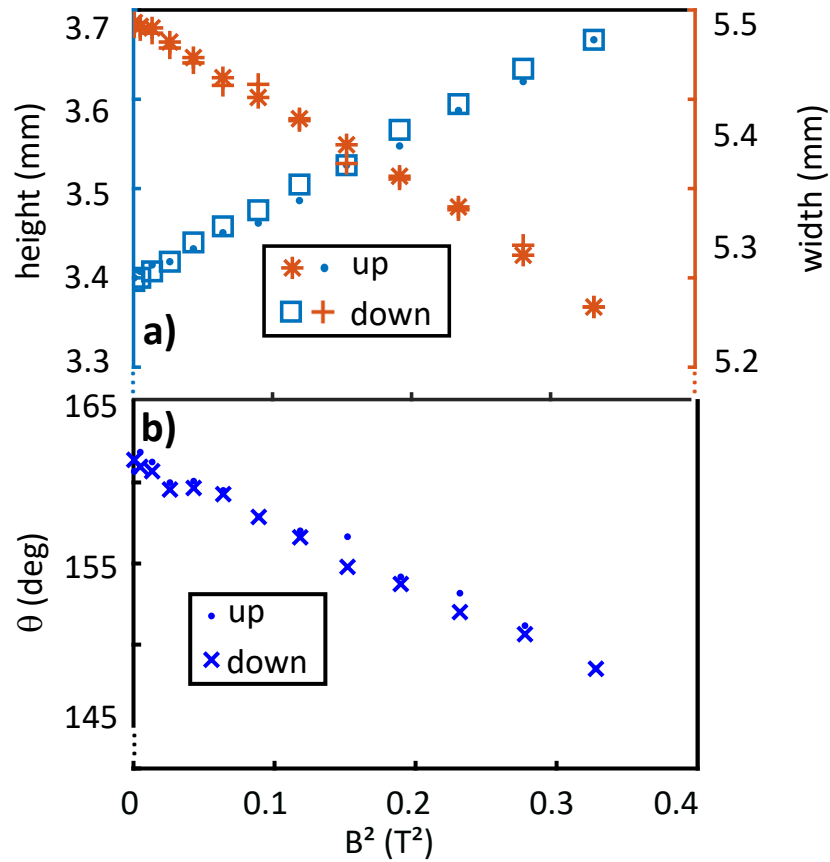
Figure 5.4: Characteristic parameters of the shape of the drop presented by Fig. 5.8) as a function of the increasing (dots) and decreasing (x) applied field. **a)** The height increases and the width decreases linearly with the square of the applied field. The error on these data points is 7 μm as discussed in Sec. 4.4.4. **b)** The contact angle (θ) decreases linearly with the square of the applied field, where the error on these data points is 1°. The proportionality of the shape with B^2 was also found in the analytical relationship between shape and applied field (Eq. 5.1).

the background light and the pixel resolution of the camera. Between the increasing and decreasing field scan ('up' and 'down') there is a small amount of hysteresis visible in the data, which originates from the substrate properties (hysteresis in receding and advancing movement of the triple contact line). The deformation is fully reversible as long as the volume of the drop remains constant for the duration of the measurement.

The elongation of the drop presented by Fig. 5.2 is due to a difference in normal stress across the liquid-vapour interface due to the applied magnetic field. This stress difference is plotted along the outline of the drop in the absence of magnetic fields in Fig. 5.5, illustrating how the drop is deformed to the elongated shape at 0.6 T. The magnetic stress difference is directed outwards from the drop along the magnetic field lines and its magnitude is proportional to the normal component of the magnetic flux density B_n^2. The magnetic stress is largest at the apex point, where the surface normal of the drop is parallel to the magnetic field lines, and diminishes at the outermost sides of the drop, before increasing again. At the solid-liquid interface, the surface vector of the drop is also parallel to the magnetic field lines, resulting in a magnetic stress and subsequent elongation of the drop towards the solid substrate which has not been studied here. This effect can be observed when suspending the droplet in a non-magnetisable medium [82].
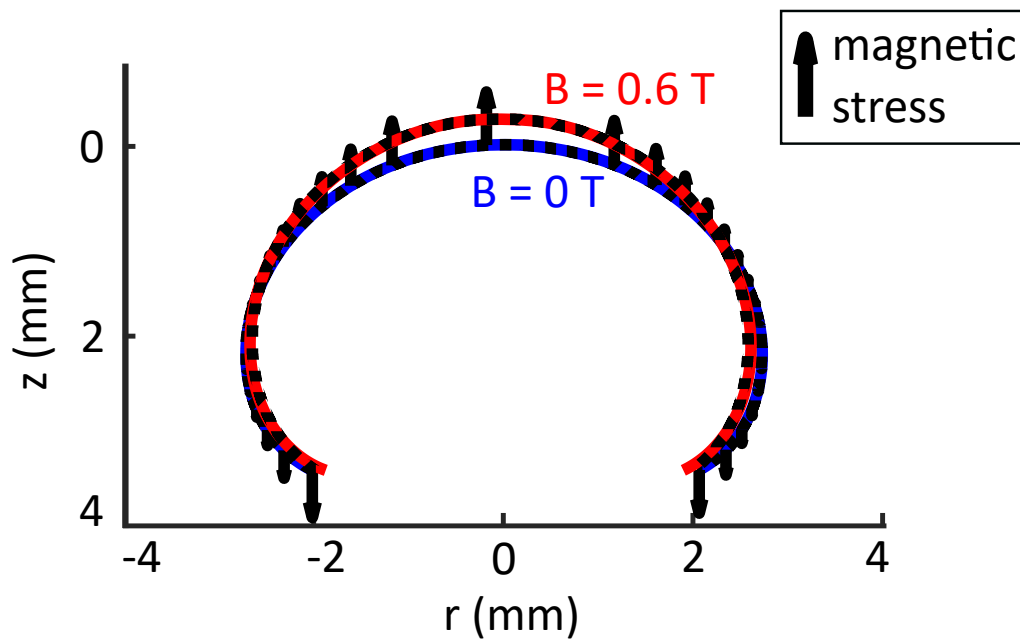
Figure 5.5: Stress on a paramagnetic drop due to a homogeneous magnetic field. The outlines (black dashed) of the paramagnetic drop presented by Fig. 5.2, and the corresponding numerical solutions of Eq. 5.1. The relative magnitude of the magnetic stress (black arrows) is proportional to the vector component of the magnetic field parallel to the surface vector, which is largest at the apex point.

The polarity of the applied field does not affect the direction of the magnetic stress. This is due to the fact that the magnetic stress depends on the square of the applied field (Eq. 5.1). Fig. 5.6 shows the contact angle of a 60 μl drop of an aqueous solution of 0.35% ppw $MnCl_2 \cdot 4H_2O$ as a function of applied field (in an increasing and a decreasing field scan). The polarity of the field is reversed, by switching the direction of current through the electromagnet. The contact angle of the drop is measured again as a function of field (again in an increasing and a decreasing field scan). The contact angle decreases in both cases from 146° to 135° and is therefore clearly independent on field direction.

While the deformation of the drop is independent on the polarity of the applied field, it is affected by the axisymmetry of the drop. The ideal drop - which is described by the mathematical model - is perfectly axisymmetric. The real drop however, is not - as mentioned above in the description of how free parameters in the fit equation are optimised to account for this difference between reality and model. The shape of the real drop is affected by the levelling of the substrate - which is manually adjusted to within ±1°; the manual positioning of the drop within the centre of the magnetic field (±1 mm); and the consistency of the hydrophobicity of a substrate - spatial consistency and consistency after repeated use - and between different substrates. To quantify the effect of these considerations onto the equilibrium shape of a drop in the absence of a magnetic field, the height and width of drops of different volumes is
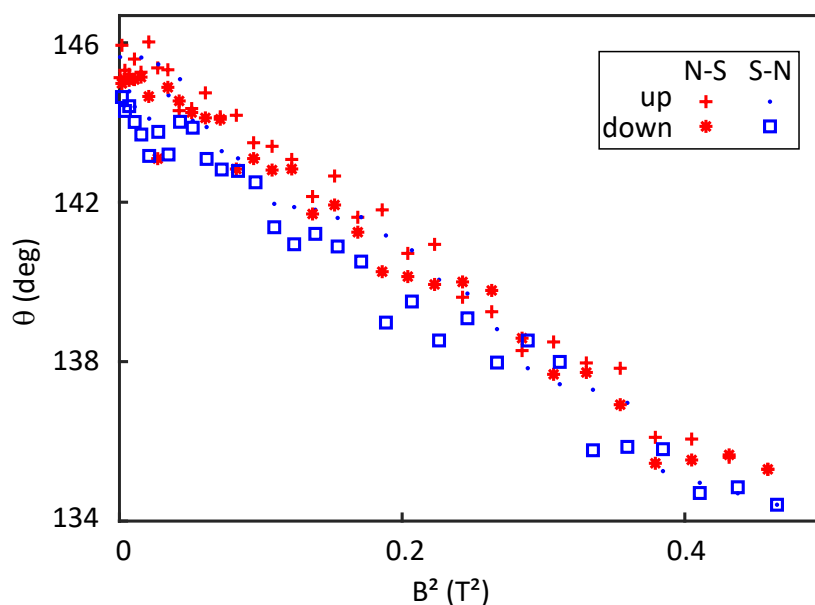
Figure 5.6: The contact angle of a 60 μl drop of 0.35% ppw $MnCl_2 \cdot 4H_2O$ aqueous solution on a Teflon-coated glass slide is shown against applied magnetic field. A reversal of the polarity of the field (from N-S to S-N) does not affect the response of the drop, i.e. the drop still elongates along the field lines, causing a decrease in contact angle with increasing applied field.

presented by Fig. 5.7. The height and width of a drop is proportional to the volume of the drop. The height and width for drops of the same volume varies within ±0.2 mm.

5.4.2 Scaling of shaping drops with magnetic fields

The scaling in height with the volume of the drop extends to a scaling in the change in height due to an applied magnetic field with the volume of the drop. In this section I investigate the effect of the volume and of the susceptibility on the shaping of a drop in a magnetic field.

A set of paramagnetic drops with different volumes in the absence and presence of a magnetic field is presented by Fig. 5.8. Side-profile photographs of 40, 60, and 80 µl drops of the aqueous solution of 51.4% ppw $GdCl_3 \cdot 6H_2O$ are presented, taken at 0 and 0.6 T applied field. The equilibrium shape of the drops in the absence of
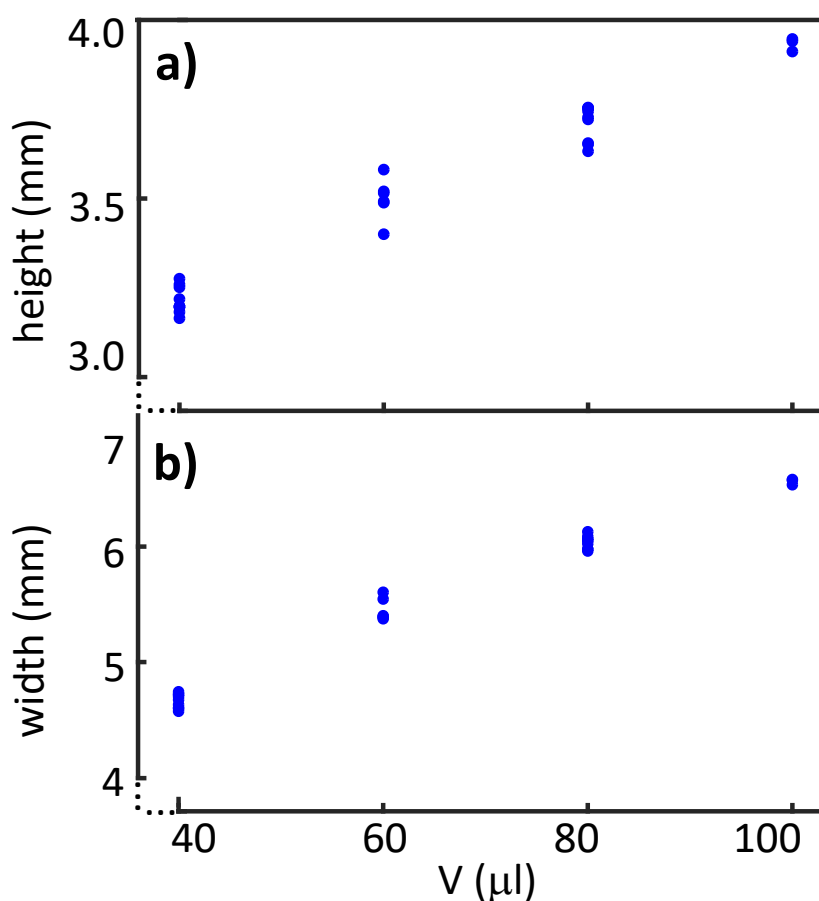
Figure 5.7: The height and width of drops is measured, to quantify the effect of the levelling and quality of the substrate, and the manual positioning of the drop on the shape of a drop. **a)** Height and **b)** width of drops plotted against their volume in the absence of a magnetic field. The height and width of drops of the same volume varies within ±0.1 mm.
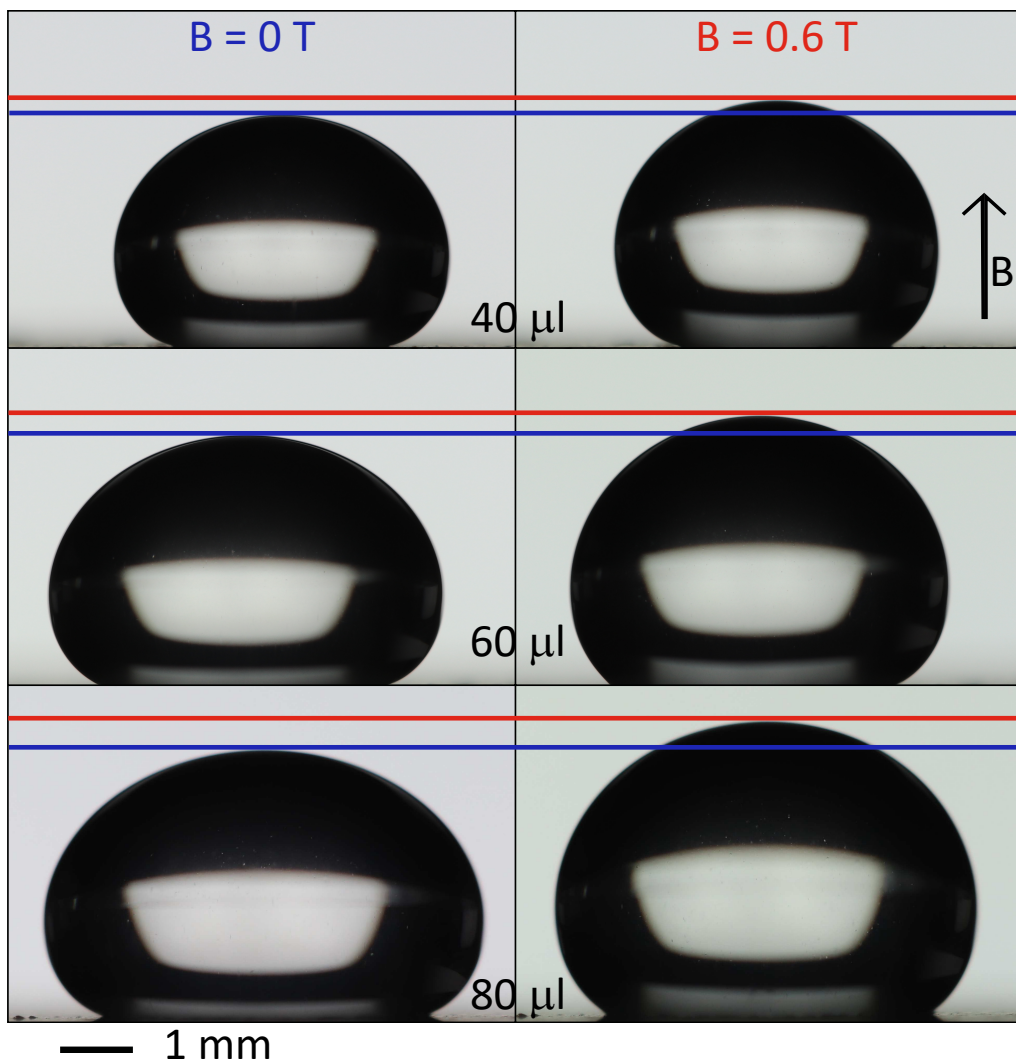
Figure 5.8: Images of the elongation of paramagnetic drops with various volumes in a homogeneous magnetic field. The elongations of 40,60, and 80 µl drops of an aqueous solution with 51.4% ppw $GdCl_3 \cdot 6H_2O$ are shown. The elongation is stronger the larger the volume of the drop.

magnetic fields is determined by gravity and surface tension. The effect of gravity is a flattening of the drop, which is more pronounced the larger the drop (the 80 µl is more flattened than the 60 and 40 µl drop). When a magnetic field is applied, the drops are visibly elongated along the field lines, with their height increased and width decreased, compared to the images of the drop in the absence of a magnetic field. The change in height increases with the volume of the drop.

To investigate this relationship further, the deformation of the drops shown in Fig. 5.8 has been repeated for drops with the same volumes. The difference in height between no applied field and 0.5 T applied field has been measured and is presented in Fig. 5.9a). The change in height increases proportionally to the volume of the drop.
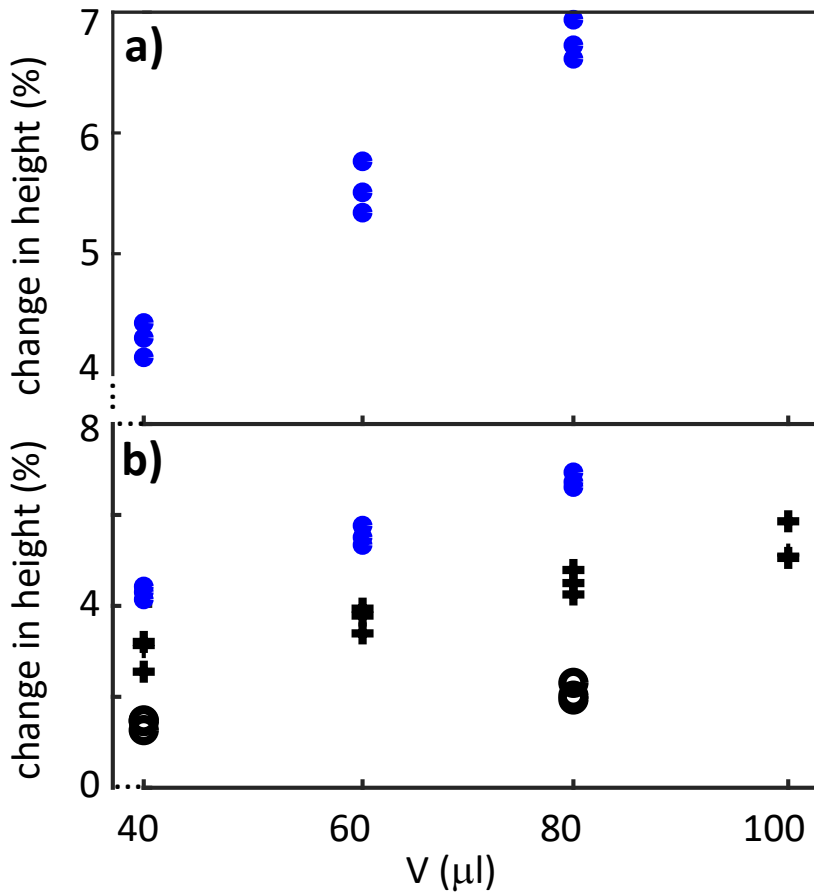
Figure 5.9: **a)** Change in height of paramagnetic drops with different volumes due to the application of a 0.5 T strong magnetic field. The drops are aqueous solution with 51.4% ppw $GdCl_3 \cdot 6H_2O$ with 40, 60 and 80 µl volume. The change in height increases linearly with volume. **b)** The change in height for drops of different salt solutions against volume increases with the magnetic susceptibility of the solution. The three different markers represent the three salt solutions (in order of increasing magnetic susceptibility): 17.8% ppw $MnCl_2 \cdot 4H_2O$ (circles), 35.6% ppw $MnCl_2 \cdot 4H_2O$ (crosses), and 51.4% ppw $GdCl_3 \cdot 6H_2O$ (dots).

The measurements for drops of the same volume show the expected spread in their change in height, due to the substrate levelling, manual positioning of the drop, and quality of the substrates, as discussed above. Fig. 5.9b) shows the change in height of drops of different salt solutions against volume. The change in height fans out into separate linear relations with respect to volume for the different salt concentrations. As well as being proportional to the volume of the drop, the change in height is also proportional to the magnetic susceptibility χ of the drop, as predicted by Eq. 5.1.

The product of χ and the volume of the drop is proportional to the total magnetic moment of the drop ($J = \chi V B \mu_0^{-1}$). Fig. 5.10 shows the change in height in the absence and presence of magnetic fields (B = 0.5 T), of drops with a range of concentrations and volumes. The change in height increases proportionally to the
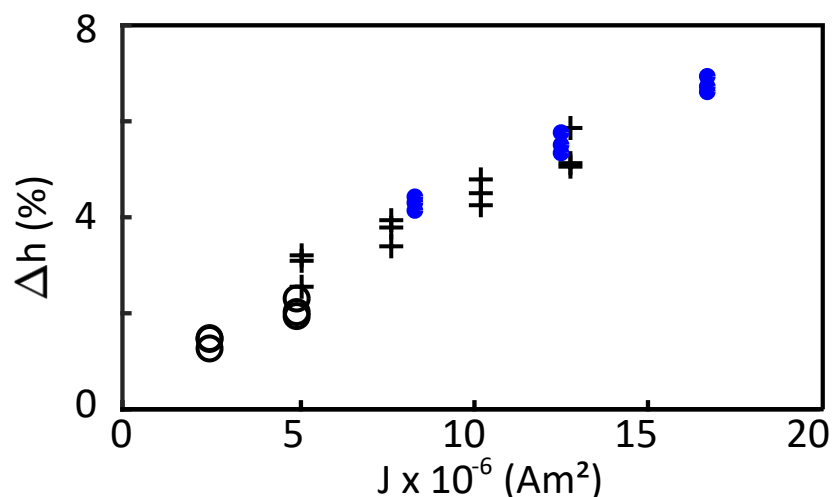
Figure 5.10: The change in height (Δh) between 0 and 0.5 T applied field (B) of drops with different total magnetic moments (J). The change in height increases with total magnetic moment ($J=\chi VB\mu_0^{-1}$) of a drop with volume V and magnetic susceptibility χ. The three different markers represent the three salt solutions: 35.6% ppw $MnCl_2 \cdot 4H_2O$ (crosses), 17.8% ppw $MnCl_2 \cdot 4H_2O$ (circles), and 51.4% ppw $GdCl_3 \cdot 6H_2O$ (dots).

drops total magnetic moment. This result clearly illustrates the underlying electromagnetic theory presented in Eq. 5.1, where the magnetic stress difference across the liquid-vapour interface of the drop, and therefore the shape of the drop, is directly dependent on the exchange of momentum between the magnetic field and the drop - or the total magnetic moment induced by the field into the drop.

While the magnitude of χ affects the strength of deformation of the drop, the sign of χ affects the direction of deformation. At negative susceptibility (diamagnetic drop), the deformation of the shape of the drop in a magnetic field is reversed: the drop is shortened along the field lines - the height decreases and the width increases. An example of a result of this methodology is shown by Fig. 5.11. A 100 µl drop of an aqueous solution of 55.8% $Br_2Ca \cdot xH_2O$ (see Tab. 5.1) is imaged in the absence of a magnetic field (Fig. 5.11a)). The fit of Eq. 5.1 runs smoothly along the outline of the drop, and the numerically optimised parameters of the calcium bromide are the surface tension (70.7 ± 1) mN m^{-1} which is within two standard errors of the surface tension of water (72.8 mNm^{-1}); and the field-independent chemical potential $(1.8 \pm 1) \times 10^{-4}$ J kg^{-1}.

Upon application of a magnetic field, the drop is shortened along the direction of the field lines, as shown by Fig. 5.11b), which shows an enlarged view of the outline of the drop at the apex point. The height and width of the drop as a function of applied magnetic field is presented by Fig. 5.12. As the applied field is increased from 0 to 1.2
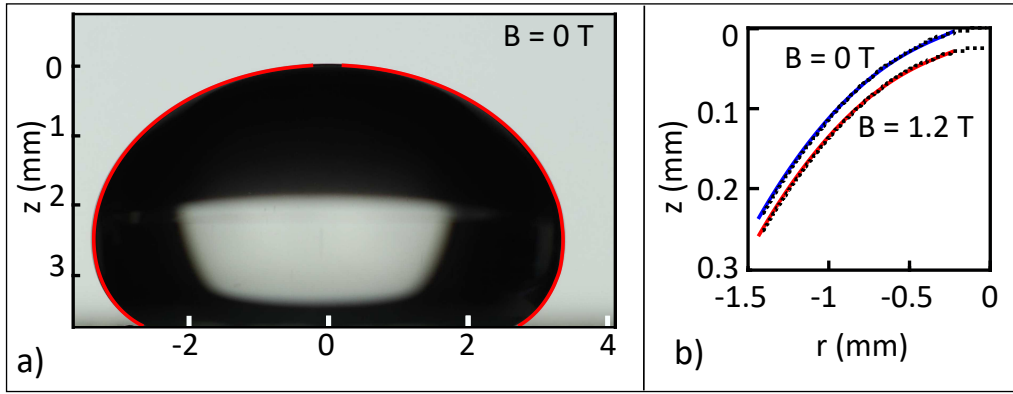
Figure 5.11: **a)** Deformation of a 100 μl drop of an aqueous solution of 55.8% $Br_2Ca \cdot xH_2O$ (see Table 4.1). The numerical solution of the modified Young-Laplace equation (red) is shown on an image of the drop in absence of a magnetic field. **b)** Enlarged view of the outline close to the apex point (black, dashed) with the numerical solution of the modified Young-Laplace equation in the absence of a magnetic field (blue) and with 1.2 T applied field (red).
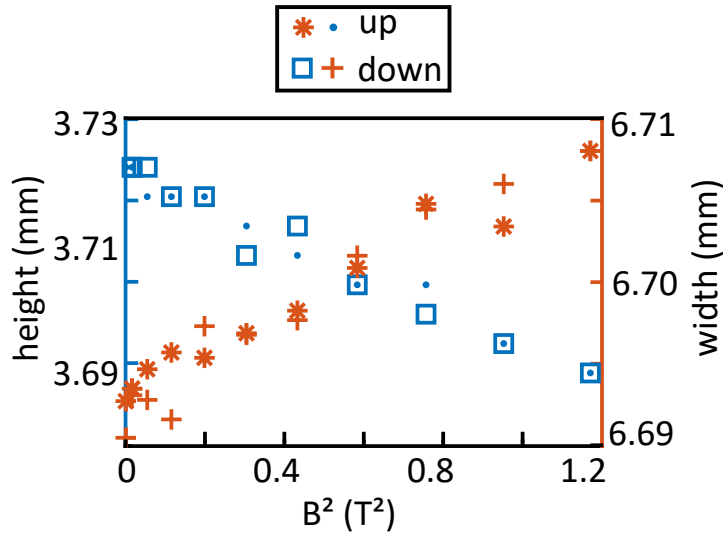
Figure 5.12: Height and width of a diamagnetic drop of 100 μl aqueous solution of 55.8% $Br_2Ca \cdot xH_2O$ against the strength of the applied magnetic field. As predicted by the analytical model (Eq. 5.1), the reverse effect to the elongation of a paramagnetic drop occurs here for a diamagnetic drop, namely that the height decreases and the width increases proportionally to the square of the applied field. The error on these data points has is 7 μm as discussed in Sec. 4.4.4.

T, the height reduces from 3.73 to 3.69 mm, and the width increases from 6.69 to 6.71 mm. The change in shape is proportional to the square of the applied field.

I find this deformation to be repeatable, with a change in height of $-(1.3\pm0.2)\times10^{-5}$ m and $-(2.5\pm0.2)\times10^{-5}$ m for 100 μl drops of the 55.8% $Br_2Ca \cdot xH_2O$ and 15.7% $NaSO_4$ solutions respectively when changing the applied field from 0 to 0.9 T.

The deformation of the diamagnetic drops is an order of magnitude smaller then the deformation of paramagnetic drops. This is due to the fact that the magnitude of the susceptibility of the diamagnetic salt solutions is ≈1-2 orders of magnitude smaller than that of the paramagnetic salt solutions. Because of this scaling effect, the range of volumes and concentrations over which diamagnetic drops can be investigated here is limited by several factors: the volume needs to be maximised, but is limited by the size of the homogeneous field region (100 μl); the salt concentration must be maximised, but is limited by the solubility limit of the salt.

While changing the above discussed scaling parameters, the free parameters in Eq. 5.1, such as the surface tension γ and field-independent chemical potential ξ_0, are optimised in the fit routine. Comparing the variation in γ and ξ_0 for drops with different volumes and susceptibilities, I find that (i) ξ_0 varies independently of the total magnetic moment, between -4×10^{-3} and 1×10^{-3} J kg^{-1}; (ii) γ decreases with increasing concentration; and (iii) γ is independent on the volume. The optimised values of γ for the paramagnetic drops are $\gamma = (71.3 \pm 0.3)$ mN m^{-1}, $\gamma = (72.3 \pm 0.1)$ mN m^{-1}, and $\gamma = (69.8 \pm 0.5)$ mN m^{-1} for the 35.6% ppw MnCl$_2 \cdot$4H$_2$O, 17.8% ppw MnCl$_2 \cdot$4H$_2$O, and 51.4% ppw GdCl$_3 \cdot$6H$_2$O solutions respectively. For the diamagnetic drops, the surface tension value of the sodium sulphate solution is $\gamma = (73.5 \pm 1)$ mN m^{-1}.

5.4.3 Dimensionless parameters

The scaling parameters discussed can also expressed in dimensionless parameters, obtained as ratios of relevant energies in the system. To investigate how the energy induced into the system by a change in applied magnetic field is stored, we consider the free energy of the drops[51]:

$$G = G_S + G_g + G_m \tag{5.2}$$

where G_S is the free surface energy, G_g is the free gravitational energy, and G_m is the free magnetic energy due to the applied magnetic field. The surface energy is determined by the surface tension, which we assume to be independent of applied field. The gravitational free energy depends on the change in the height of the centre of mass δh of the drop, which rises for a paramagnetic drop and is lowered for a diamagnetic drop with increasing magnetic field strength:

$$G_g = mg\delta h \tag{5.3}$$

The magnetic free energy depends on both the magnetisation of the drop, which is in itself field-dependent, and the applied field. The change in free energy δg equals a

change in field-dependent thermodynamic potential a_{em} (Eq. 3.31) due to a change in applied field:

$$\delta g = H \cdot \delta B \tag{5.4}$$

The free magnetic energy is therefore:

$$G_m = \int_V \int_0^B H \cdot dB \, dV \tag{5.5}$$

$$= \frac{1}{2} \chi \frac{B^2}{\mu_0} V \tag{5.6}$$

where V is the volume in m^3. The surface energy is the surface tension multiplied by the surface area:

$$G_s = \gamma V^{2/3} \tag{5.7}$$

where we have approximated the surface area as $4\pi r^2 = (4\pi)^{1/3} 3^{2/3} V^{2/3} \approx V^{2/3}$. The ratio of the gravitational and surface energy is commonly known as the bond number:

$$B_0 = \frac{G_g}{G_s} \tag{5.8}$$

$$= \frac{\rho g V^{2/3}}{\gamma} \tag{5.9}$$

where we approximated that δh is of the order of magnitude of the radius of the drop ($\delta h = V^{1/3}$). If $B_0 \gg 1$ then the shape of the drop is dominated by gravity - the drop is flattened into a puddle. If $B_0 \ll 1$ then the shape of the drop is dominated by surface tension - the drop has the shape of a capped sphere. For the drops presented here, B_0 ranges between 1.5 for the 40 µl drops to 3 for the 100 µl drops. The effects of gravity of the shape of the drop scale with the volume of the drops, which confirms our observation that the larger drops are more flattened by gravity in Fig. 5.8.

The ratio of the magnetic to surface energy is the magnetic bond number [100]:

$$B_m = \frac{\chi V^{1/3} B^2}{2\gamma \mu_0} \tag{5.10}$$

Since the magnetic bond number scales linearly with B^2, the change in shape of the drops scales linearly with B_m. For the drops presented here, $|B_m|$ varies between 0 and 5. Fig. 5.13a) shows the height of drops of 51.4% $GdCl_2 \cdot 6H_2O$ against magnetic Bond number. The height increases linearly with magnetic bond number and is larger than 1 at $B = 0.3$ T applied field, which is when the magnetic force starts to dominate over the surface force in determining the shape of the drop.

The ratio of magnetic to gravitational free energy is:

$$\alpha = \frac{\chi B^2}{2\mu_0 \rho g \delta} \tag{5.11}$$

When $\alpha \gg 1$ then the change in magnetic energy is larger than the change in gravitational energy, and vice versa for $\alpha \ll 1$. Fig. 5.13 shows α at 0.6 T applied field, where δ is replaced by the length scale $V^{1/3}$. α is close to 1, particularly considering that the assumption that $\delta \approx V^{1/3}$ leads to an overestimate of the energy stored in the change in gravitational potential. α is largest for drops with the highest susceptibility
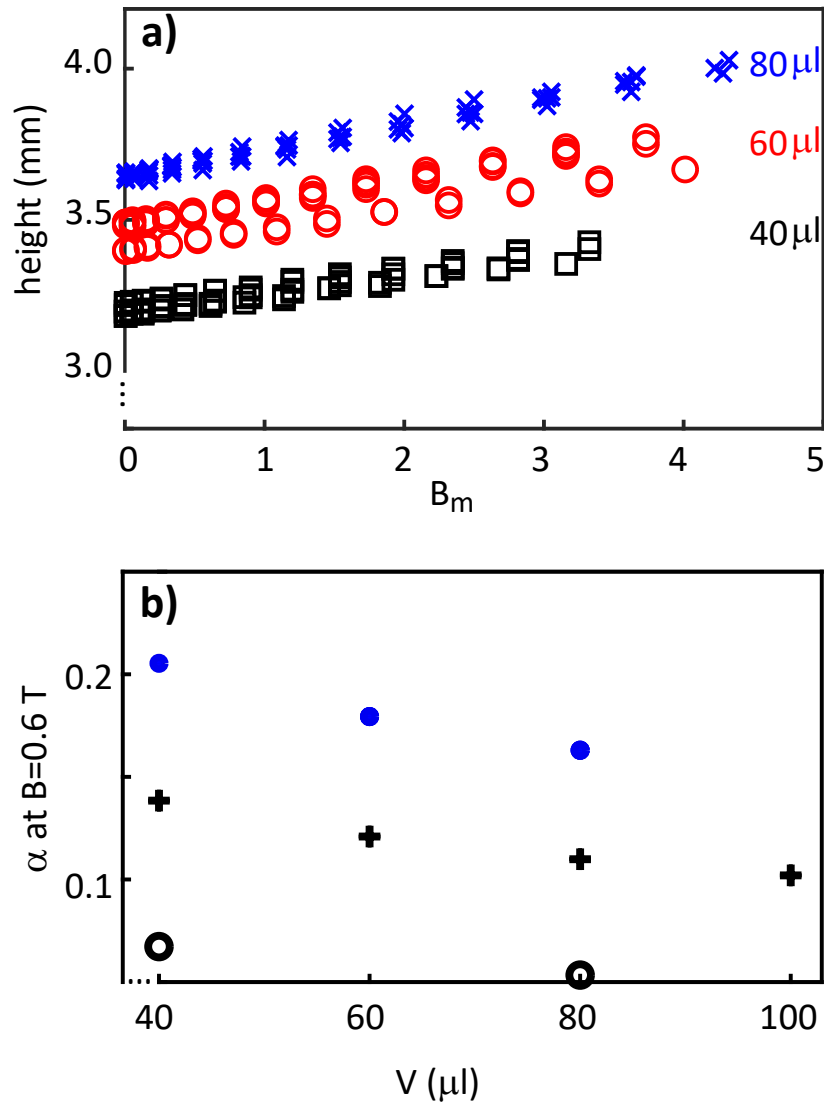
Figure 5.13: Dimensionless analysis of the forces and energies acting on a drop in a magnetic field. **a)** The height of drops of 51.4 % $GdCl_2 \cdot 6H_2O$ with different volumes against magnetic bond number. **b)** The dimensionless ratio of magnetic and gravitational free energy for drops with a range of volumes. The susceptibilities of the drops are again indicated through the symbols, as in Fig. 5.9.

(51.4 % $GdCl_2 \cdot 6H_2O$) and smallest volume (40 µl). We can conclude from these considerations that the change in free energy due to the application of a magnetic field to the drop is stored in equal measures as magnetic and gravitational energy.

5.4.4 Transporting drops with magnetic fields

The magnetic stress difference across the liquid-vapour boundary of drops in a magnetic field can be used to transport them. In this section I discuss some example results of the transport measurements of diamagnetic and paramagnetic drops in a non-uniform magnetic field.

Fig. 5.14 shows the profile of the non-uniform magnetic field which decays along the x-axis from a maximum value of B_m. A 100 µl drop of 27.4% ppw $MnCl_2 \cdot 4H_2O$ in aqueous solution is placed into the non-uniform region of the field and the maximum field strength B_m is increased until the drop is transported into the field. At $B_m = 0.4$ T the drop leans towards the region of highest magnetic flux density. Upon increasing B_m, the drop is pulled over a distance of approximately 12 mm towards the region of highest magnetic field strength. The following QR code links to a video of this attraction of the paramagnetic drop into the magnetic field.

Attraction of a paramagnetic drop into a magnetic field

The transport of drops occurs in two stages, namely leaning and sliding. An example of this process is shown in Fig. 5.15, where a) images of the leaning and b) the position of the centre-of-mass (CM) and contact angles of the paramagnetic drop presented in Fig. 5.14 are shown. As the strength of the magnetic field is increased, the drop leans towards the region of highest magnetic field strength. During leaning, the drop is pinned by the friction between substrate and drop. At a threshold field strength, the friction is overcome, and the drop starts sliding. The two stages of transportation are clearly visible in the data of the contact angles and CM position. During leaning, the advancing contact angle increases and the receding contact angle decreases, while the horizontal position of the CM gradually increases. Once the threshold field strength is reached, the drop slides and the position of the CM is increases rapidly. The contact angles are reset to approximately their initial value, and the horizontal position of the CM has rapidly increased, translocating the drop into the region of highest magnetic field strength.
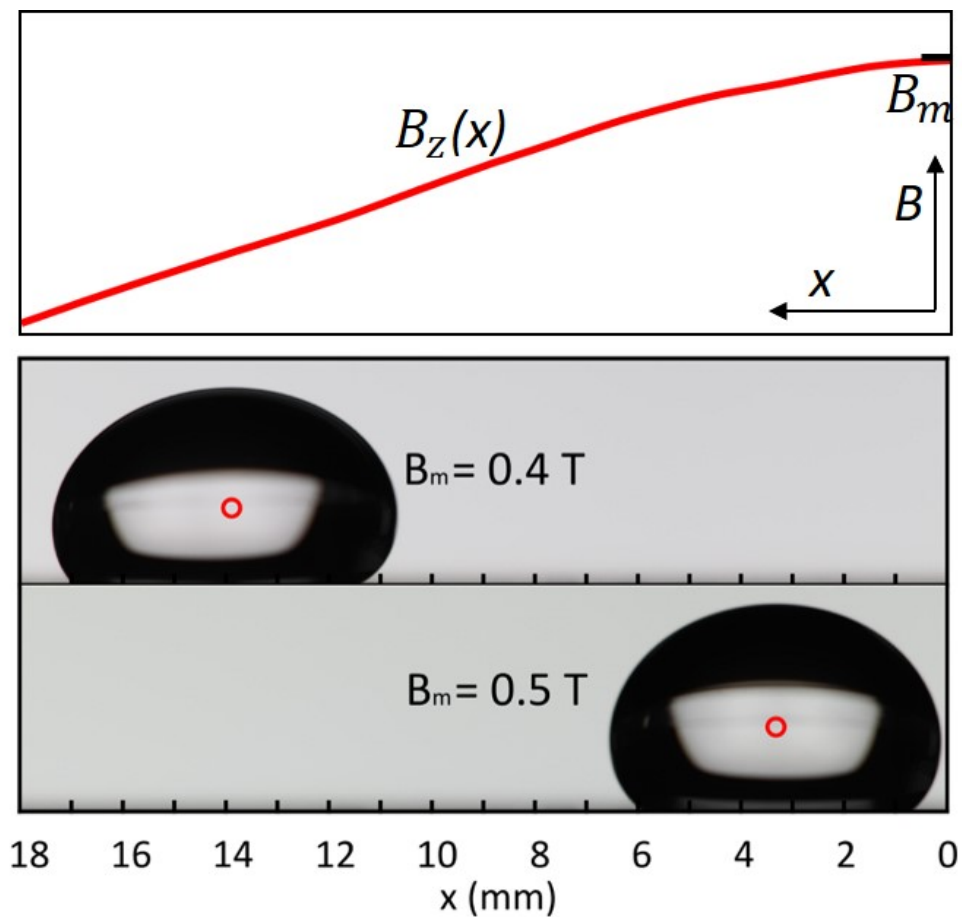
Figure 5.14: Transport of a paramagnetic drop in a non-uniform magnetic field. Illustration of the profile of the magnetic field, which decays along the x-axis from its maximum value B_m. As B_m is increased a 100 µl drop of 27.4% ppw $MnCl_2 \cdot 4H_2O$ in aqueous solution is pulled towards the region of highest field strength. The positions of the centre-of-masses are indicated as red circles. The properties of the salt solutions are summarised in Table 4.1.
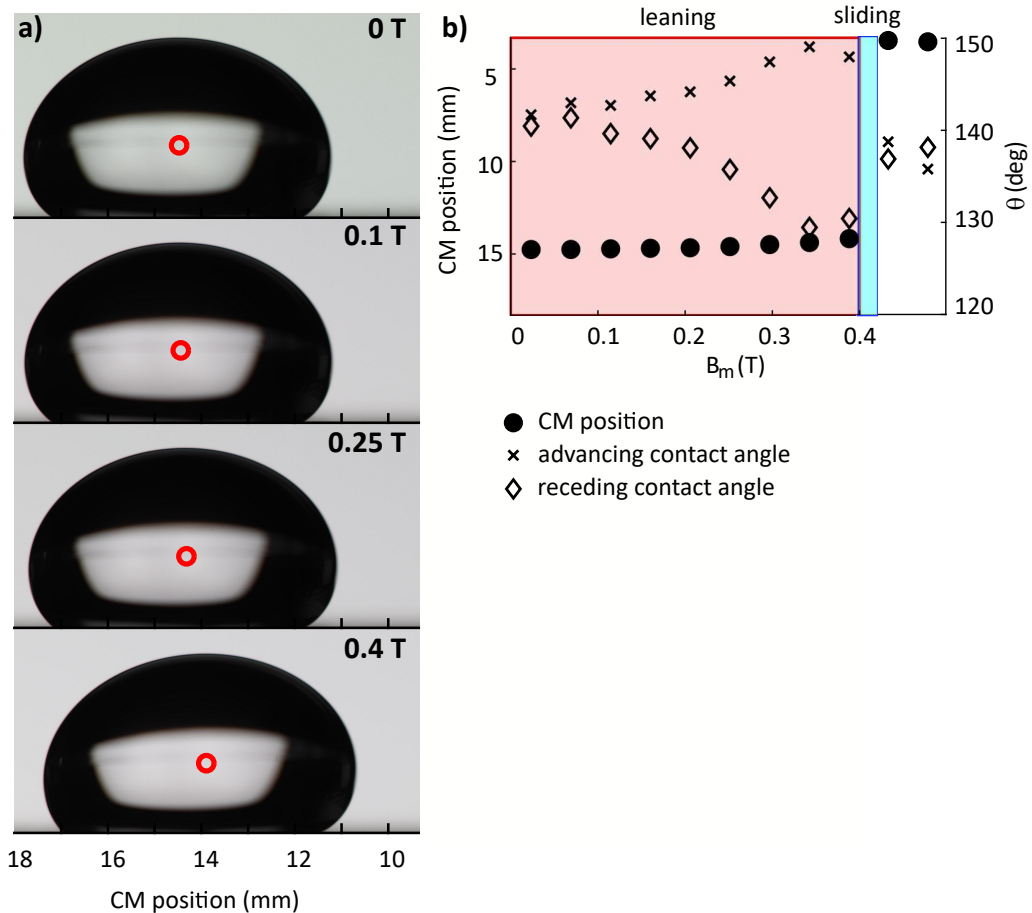
Figure 5.15: Leaning and sliding of a paramagnetic drop due to a non-uniform magnetic field. **a)** Images of the leaning of the drop from Fig. 5.14 are shown. Leaning is the first stage of the transportation. **b)** The position of the centre-of-mass (CM) and the contact angles of the drop in a) are shown. The two stages of transportation are clearly visible in the data: during leaning the advancing contact angle increases and the receding contact angle decreases, while the horizontal position of the CM gradually increases; once a threshold field strength is reached, the drop slides. After sliding, the contact angles are reset to approximately their initial value, and the horizontal position of the CM has rapidly increased.

Fig. 5.16 shows a 300 µl drop of 15.7% ppw $NaSO_4$ in aqueous solution in the same non-uniform magnetic field as the paramagnetic drop in Fig. 5.14. Again, the maximum field strength B_m is increased until the drop is transported by the field. At 0.75 T the drop leans away from the region of high magnetic flux density. Upon increasing B_m the drop is pushed over a distance of approximately 3 mm away from the region of highest magnetic flux density. The following QR code links to a video of the repulsion of this drop from the magnetic field.

Repulsion of a diamagnetic drop from a magnetic field
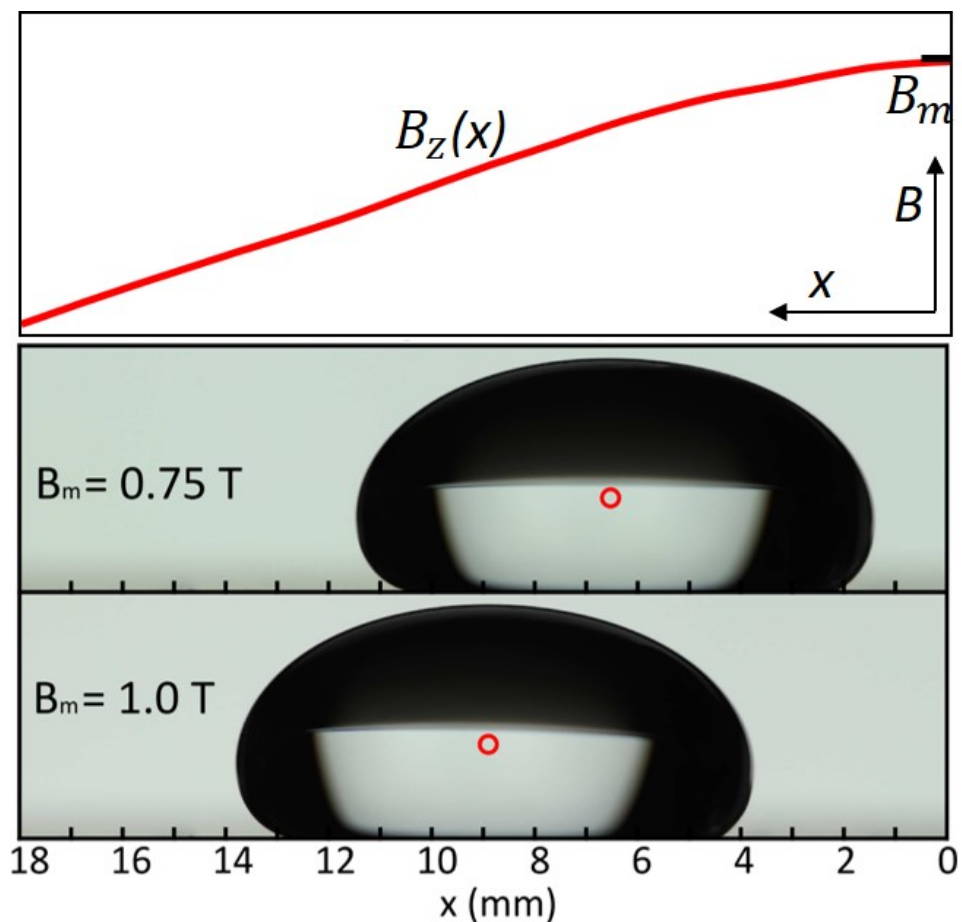
Figure 5.16: Transport of a diamagnetic drop in a non-uniform magnetic field. Illustration of the profile of the magnetic field, which decays along the x-axis from its maximum value B_m. As B_m is increased, a 300 µl drop of 15.7% ppw $NaSO_4$ in aqueous solution is pushed away from the region of highest field strength. The positions of the centre-of-masses are indicated as red circles. The properties of the salt solutions are summarised in Table 4.1.

The translocation of the centre-of-mass in these experiments is repeatable, with drops of 100 µl manganese chloride solutions pulled over a distance of (10.4±0.3) mm, and drops of 300 µl sodium sulphate solution pushed over a distance of (3.0±0.3) mm.

The transport direction is determined by the sign of χ, while the transport distance is determined by the value χ, the size of the drop, and the field gradient. Due to the field gradient, the drop deforms asymmetrically, causing it to lean into ($\chi > 0$) or out of ($\chi < 0$) the region of higher field strength. The static frictional forces between substrate and drop determine how much the drop leans before sliding. Though the stress acting on diamagnetic drops is several orders of magnitude smaller than on paramagnetic drops, it is nevertheless sufficient to achieve transport even in a simple experimental design as we have employed here. Diamagnetic solutions enable the reversal of transport direction, compared to paramagnetic solutions or ferrofluids, without the need to alter the actuation mechanism.
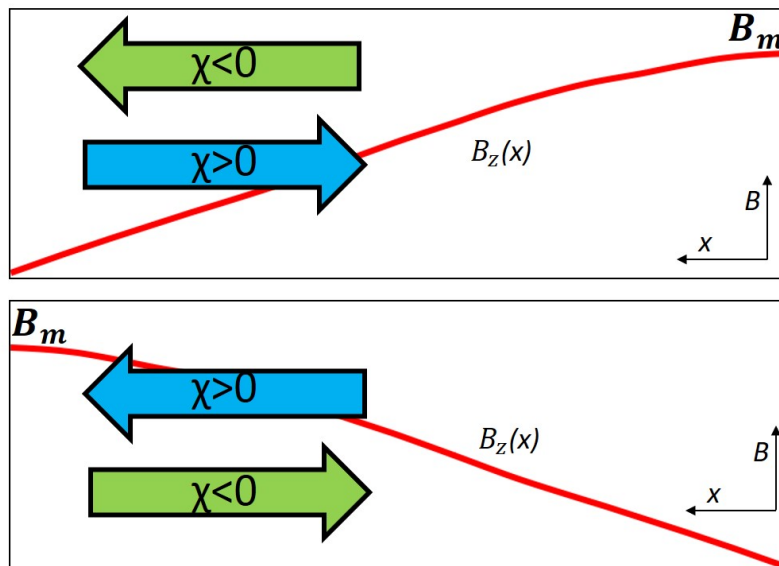
Figure 5.17: Schematic of the transport direction of drops in magnetic fields. The transport directions for paramagnetic drops (blue arrow) and diamagnetic drops (green arrow) are indicated for two different field profiles. Paramagnetic drops are transported to the region of highest magnetic field strength, while diamagnetic drops are transported away from it.

5.5   Summary and conclusion

This chapter investigated the shaping of drops with magnetic fields. Paramagnetic drop can be shaped with a homogeneous magnetic field. The strength of the deformation is larger for drops with a higher total magnetic moment, meaning a larger volume and magnetic susceptibility, and a larger applied magnetic field. The magnetic susceptibility can be tuned through the salt concentration of the drop. An increase in salt concentration equals an increase in magnetic susceptibility and therefore a stronger deformation due to the application of a magnetic field. This observation strengthens the argument that the deformation of the drop is not due to electric fields. The strength of deformation of a drop due to electric stress is proportional to its electric susceptibility, which is discussed in Ch. 3 and shown by Fig. 2.5 where the drop with the higher permittivity (and therefore higher susceptibility) deforms more strongly than the drop with the lower permittivity. Since electric susceptibility of aqueous solutions decreases with increasing salt concentration [101] the increase in strength of deformation due to an increase in salt concentration that I observe here cannot be due to electric stress.

The shape of axisymmetric para- and diamagnetic drops in magnetic fields can be modelled using the modified Young-Laplace equation (Eq. 5.1) presented in Ch. 3. This model has the potential for adaptation to non-axisymmetric deformations on non-uniform magnetic fields. While paramagnetic drops ($\chi > 0$) elongate, diamagnetic drops ($\chi < 0$) shorten along the magnetic field lines in a homogeneous magnetic field.

Paramagnetic drops are pulled into and diamagnetic drops are pushed out off a non-uniform magnetic field. The transport of paramagnetic drops can be achieved at low salt concentrations and field strengths. Paramagnetic drops can therefore be implemented in droplet microfluidics, offering a flexible actuation mechanism. Though the force on diamagnetic drops is several orders of magnitude smaller than on paramagnetic drops, it is nevertheless enough to achieve transport in non-uniform magnetic fields. Diamagnetic drops have a previously unexplored potential for microfluidic applications and the magnetic stress on diamagnetic drops, and subsequently ease of transport, can be increased by suspending the drops in a fluid with a positive magnetic susceptibility, such as a ferrofluid. Though the presented solutions have a too high osmolality to contain mammalian cells (2 osm/kg and 8 osm/kg for the sodium sulphate and calcium bromide solutions respectively), further dilution and usage of stronger magnetic fields may permit suspension and transport of mammalian or plant cells. This technique may also be applied to suspension and transport of DNA or other macromolecules such as proteins.

In the following chapter I explore some applications of shaping drops with magnetic fields.

Chapter 6

Applications of shaping drops with magnetic fields

6.1 Introduction

In this chapter, I explore some applications of the shaping of drops with magnetic fields, namely rheological measurements (Sec. 6.2) and diamagnetic floating objects (Sec. 6.3).

In Sec. 6.2, I investigate how shaping of a drop with a magnetic field is affected by the viscoelastic properties of the drop. In Sec. 6.2.1, I introduce the topic of rheology - for which I relied in particular on the comprehensive reviews by Struble *et al.* [102] and Chen *et al.* [103] - and describe how viscosity can be measured in a strain relaxation experiment. In Sec. 6.2.2, I develop an experimental design to perform a strain relaxation experiment with the set-up presented in Chapter 4 that was used in Chapter 5 to shape and transport drops. I use this set-up in Sec. 6.2.3 to measure the strain relaxation of drops of aqueous solutions of glycerol and a paramagnetic salt. I also developed an algorithm to measure the relaxation time of the drop, which I also describe in Sec. 6.2.3, including a description of the corresponding Matlab programs that I developed. In Sec.6.2.4, I present and discuss my experimental findings, which show that the set-up needs to be modified to measure the relaxation times accurately. In Sec. 6.2.5 I summarise my findings and suggest appropriate modifications that could turn the shaping of drops with magnetic fields into a useful tool for rheological measurements.

In Sec. 6.3, I explore how solids can be driven on the liquid-vapour interface of a drop using a magnetic field. For this I demonstrate control of the position and orientation of the floating objects. This tool could be a useful model for studying statical mechanical processes, such as found in living systems.

The work presented on asymmetric objects in Sec. 6.3 was jointly conceived by myself, Paul Sullivan, Tushar Semwal and Adam A. Stokes. I was responsible for most experimental work and the analysis and interpretation of the results are entirely by my own work. Paul Sullivan and Tushar Semwal contributed to discussions and experiments. Adam A. Stokes provided project supervision.

6.2 Characterisation of viscous fluids

6.2.1 Introduction to rheology

Rheology studies the yielding and flow of matter [102, 103]. It is concerned with the storage and dissipation of mechanical energy in matter. Therefore it is mainly concerned with measuring the stress applied to a material and the resulting strain - a dimensionless number that defined the amount of deformation of the material. In other words, rheology measures the extent to which a solid is elastic and a fluid is viscous. Elastic materials return to their original shape upon deformation, an example of this is a bouncy ball - a popular children's toy made from rubber which can be thrown to the ground where it deforms upon impact and bounces back up - releasing elastic as kinetic energy. Viscosity may be illustrated by considering the flow of air, water, and honey. Clearly, air flows easier than water and both flow easier than honey. This is because honey is more viscous than water, and both are more viscous than air. An image of honey dripping from a dipper is shown by Fig. 6.1a).

Figure 6.1: Honey and toothpaste are examples of viscous and viscoelastic fluids. **a)** Honey forms long strands as it drips down from a honey dipper, due to its viscous properties. Mulitfloral honey is viscous while heather honey is viscoelastic. **b)** Toothpaste - along with mayonnaise - is a viscoelastic fluid known as Bingham plastic; these are materials that behave like solids at low stresses, but flow like a viscous fluid at high stresses. I have attached the copyright to these images in Sec. A.3.
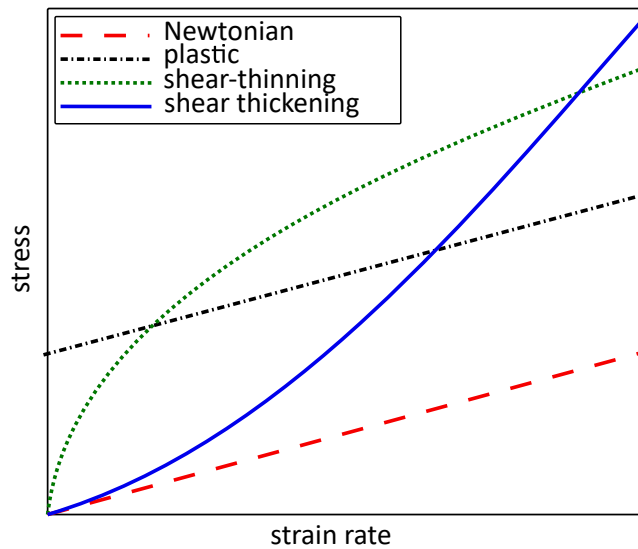
Figure 6.2: Characteristic curves of stress as a function of shear rate for Newtonian and non-Newtonian fluids.

While many honeys - such as Spanish honeys [104], Korean honeys [105], and mulitfloar honeys [106] - are viscous Newtonian fluids, some honeys - such as heather honey [106] - are non-Newtonian fluids. Non-Newtonian fluids, or complex fluids - fluids which contain more than one phase - are materials that are viscoelastic; they are both elastic and viscous. These materials can be polymers, emulsions or suspensions - such as blood, which is a suspension of blood cells (solid) in blood plasma (liquid); or heather honey, which has a high protein content [106]. Other everyday examples of complex fluids include other foods, such as ketchup and mayonnaise; and personal hygiene products, such as toothpaste [102, 103].

The flow properties of complex fluids change depending on the magnitude of stresses that act on them and on how fast these stresses are applied. Toothpaste (shown by Figure 6.1b)) - along with mayonnaise - is a Bingham plastic; these are materials that behave like solids at low stresses, but once a threshold stress is reached, they flow like a viscous fluid. Ketchup and blood are shear-thinning fluids; they flow more readily when a force is applied to them. Oobleck - a mixture of cornstarch and water - is an example of a shear-thickening fluid, which is a fluid that behaves like a solid when a force is applied to them. People can walk on pools filled with oobleck - when their feet impact on the surface of the oobleck it acts like a solid; but if they stand still the oobleck acts like a liquid causing them to sink.

Figure 6.2 shows characteristic relations between stress and strain rate of Newtonian and non-Newtonian fluids. Newtonian fluids, such as most multifloral honey, have a linear relationship between stress and strain rate, meaning that the rate at which they deform is independent of the stress applied to them; in other words, their

viscosity is independent of the applied stress. For a plastic, such as toothpaste, a threshold stress needs to be applied before the material behaves like a viscous fluid that deforms faster the more stress is applied. For a shear-thinning fluid, such as ketchup, the strain rate increases rapidly when stress is applied to it - it becomes less viscous and flows more readily. For shear-thickening fluids, such as oobleck, the strain rate decreases with stress, meaning that they become more viscous and therefore less readily deformable.

Considering the huge variety of complex fluids that are common to our everyday lives, the study of their properties is clearly hugely important. Rheometers are used to measure the relationship between stress and strain rate. They usually consist of two coplanar plates or cylinders through which either stress is applied to a sample and the strain rate is measured or vice versa. To fully characterise the rheological properties of a material, these measurements need to be performed over a large range of strain rates.

The desire to measure viscoelasticity in micron-scale objects, such as cells, has partly driven the development of microrheology [107, 108, 109, 110]. I introduced an example of a magnetic microrheological technique in Fig. 2.2: magnetic tweezers that measure the viscoelastic properties of the cytoplasm of a cell [20]. In this measurement, a magnetic particle is embedded in the cytoplasm of a cell and displaced by a magnetic field. The magnetic field is applied as a step pulse and the shear elastic modulus, effective viscosity and strain relaxation time is measured.

Viscosity is the ratio of the shear stress (F/A) and velocity gradient (dv/dy) [111]:

$$\eta = \frac{F/A}{dv/dy} \tag{6.1}$$

For a Newtonian fluid, the viscosity of a material can be established with a relaxation experiment, where a stress is applied and removed and the corresponding strain on a material is measured [111].

The behaviour of a liquid in a strain relaxation experiment can be modelled with a simple dashpot-spring circuit, such as the Maxwell model shown in Fig. 6.3. The spring models the stiffness of the liquid which is the ratio of stress σ and strain ϵ ($E = \sigma/\epsilon$) and the dashpot models the viscosity of the liquid (η). The relaxation time of such a fluid is:

$$\tau = \frac{\eta}{E} \tag{6.2}$$

Therefore, the strain relaxation time is directly proportional to the viscosity of a Newtonian liquid. By measuring the strain and strain relaxation time, the viscosity can therefore be calculated.
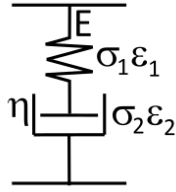
Figure 6.3: Illustration of the Maxwell model for a relaxing fluid. The spring models the stiffness of the fluid (E) and the dashpot models the viscosity (η), both have a stress σ and strain ϵ associated with them.

6.2.2 Experimental design to characterise viscous fluids

I explore here the possibility to characterise a viscous drop through shaping with a magnetic field. The viscosity determines the rate at which the shape of the droplet changes (strain rate) as function of applied force (stress). In these experiments, I measure the rate of change in shape of a drop (strain rate) due to the application and removal of a magnetic field (stress). The magnetic field is switched on and off in the fashion of a top-hat function against time. The drops are paramagnetic and placed in the homogeneous magnetic field region. As observed in the previous chapter (Ch. 5), the drops elongate upon application of the magnetic field and relax back to their initial shape upon removal of the field, as illustrated by Fig. 6.4.

The strain of the drop is measured as a change in shape, which is expressed as the dimensionless parameter D/D_0, where D:

$$D = \frac{w - h}{w + h} \tag{6.3}$$

where w is the width (major horizontal axis) and h is the height (major vertical axis) of the drop. When $D = 0$ the drop is a perfect sphere; when $D < 0$ the width is shorter than the height, the drop is elongated in the vertical direction; when $D > 0$ the height is shorter than the width, the drop is shortened in the vertical direction. D_0 is the initial measurement of D at 0 T applied field. When $D/D_0 = 1$, the drop has assumed its initial shape at 0 T; when $D/D_0 < 1$ the value of D has decreased, which means that the width of the drop has decreased and the height has increased - the drop is elongated along the vertical direction. As discussed in the previous chapters, we expect this elongation when using a paramagnetic drop and applying a homogeneous magnetic field along the vertical direction. The opposite phenomena, when $D/D_0 > 1$ due to a shortening of the drop along the vertical direction, is expected if we used a diamagnetic salt.

The dimensionless parameter D/D_0 quantifies the strain of the drop. I apply a stress to the drop while measuring the strain against time. To achieve an application
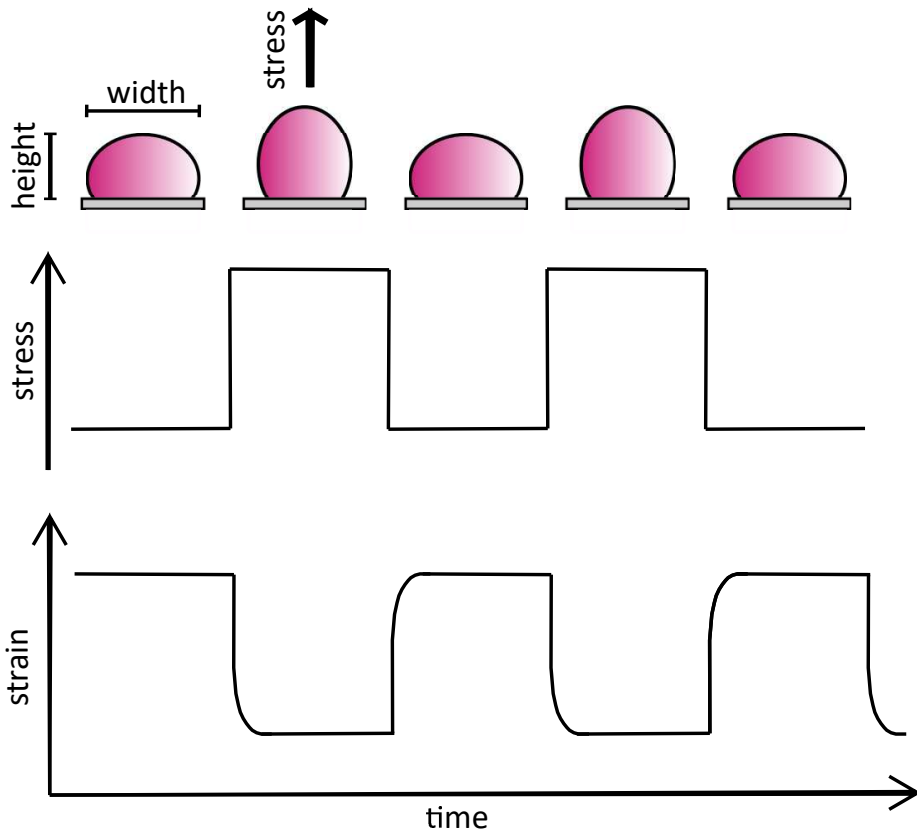
Figure 6.4: Illustration of the stress and strain of a paramagnetic drop in a magnetic field. The stress applied to the drop is the magnetic field, which is switched on and off such that it has the shape of a top-hat function when plotted against time. The stress is directed vertically upwards, causing the drop to elongate. The strain of the drop is measured as the ratio D/D_0 (defined in Eq. 6.3), which decreases as the drop elongates.

of stress in the form of a top-hat function, I increase the magnetic field strength from 0 to 0.6 T in one step, and subsequently decrease the magnetic field strength from 0.6 to 0 T in one step. Considering the previous discussion on the value of D/D_0 and its relation to the deformation of a paramagnetic drop, we expect D/D_0 to be initially equal to 1, and then decrease from 1 to some constant value upon application of the magnetic field. When the field is switched off, we expect D/D_0 to increase again to 1. The speed of this increase and decrease of strain depends on the viscosity of the drop. We therefore want to quantify the speed of the increase and decrease of D/D_0 and establish a relationship to the viscosity of the drop.

To prepare solutions with a range of viscosities, I dilute glycerol with aqueous solutions of $MnCl_2 \cdot 4H_2O$, such that the final $MnCl_2 \cdot 4H_2O$ concentration of all solutions is 15% ppw. The glycerol concentrations of the solutions are 75%, 56%, and 24% ppw. The viscosity of the solution increases with glycerol percentage. The viscocity of the aqueous glycerol dilutions are calculated using Matlab program from

Volk *et al.* [112]. The results for the here presented glycerol dilutions are listed in Tab. 6.1. Upon deformation of the drop, the applied stress is removed, and the stress that restores the drop back to its initial shape is due to the surface tension. The relaxation time can therefore be expressed as the ratio of viscosity and surface stress ($\approx \sigma/V^{1/3}$). The time that it takes for the drop to relax upon removal of the stress, is the relaxation time τ:

$$\tau = \frac{\eta V^{1/3}}{\sigma} \tag{6.4}$$

where σ is the surface tension and V is the volume of the drop (m^3). The expected values for τ are listed in Tab. 6.1. In the present experimental set-up the sample rate of the change in strain is limited by the frame rate of the camera. The drop is imaged by a DSLR camera at 50 fps, which is the maximum frame rate of the camera. The temporal resolution of the strain measurements is therefore 20 ms. We can therefore not measure τ in the present set-up. We can however, explore the change in shape of the drop and investigate if it is indeed dominated by the viscosity of the drop - and τ can therefore be determined using a faster camera - or if other factors dominate the speed of deformation of the drop.

6.2.3 Experimental method to characterise viscous fluids

The experimental set-up to deform the drop (to apply stress to the drop) is the same as described in chapter 4, where a homogeneous magnetic field, produced by an electromagnet, is applied to a drop. The field strength is increased and decreased, such that a top-hat stress is mimicked, as shown in Fig. 6.4. The top-hat stress is applied 5 times to a drop, and the resulting strain is averaged to obtain a less noisy signal from which we can extract the time constant. Four drops of each glycerol dilution are measured, and the mean and standard error of the time constants for a glycerol solution is calculated. I developed a MATLAB program to extract the time constant from these measurements. The code for this program is available at

Table 6.1: Viscosities and relaxation times of aqueous solutions of glycerol and 15% ppw $MnCl_2 \cdot 4H_2O$.

C_g	η	τ
% ppw	mPas	ms
0	1.5	0.14
24	3.6	0.33
56	21.1	1.96
75	142.0	13.18

. These are the inputs to a MATLAB program:

- side-profile video of the drop

- current (I) applied to the electromagnetic vs. time

The parameters that are determined in this program (outputs) are listed here:

- magnetic field strength B (T)

- pixel-to-distance ratio p2m (m)

- outline of the liquid-vapour interface (lv-outline) and of the solid-liquid interface (sl-outline) (pixel)

- dimensionless shape parameter D/D_0

- time constant τ (s)

The computational functions used in this program to process the inputs and obtain the corresponding *outputs* are:

- 'magnetic field module', same as in ADSA-mf (Sec. 4.4.3): the current (I) and one photograph of the drop are inputs to the magnetic field module, where the *magnetic field strength (B)* is determined, and the conversion factor from pixels on the drop image to real distance (*p2m*) is calculated.

- 'extract drop outline', similar as in ADSA-mf (Sec. 4.4.4): the video of the drop is analysed frame-by-frame, where each image is input to this function. The images are cropped and the outlines of the liquid-vapour interface (*lv-outline*) and of the solid-liquid interface (*sl-outline*) are found. The width and height is measured on the outline. When the whole video is analysed, D/D_0 is calculated.

- 'classify strain regions' (Sec. 6.2.3.1): the strain measurement (D/D_0 vs. time) is split into two sections per top-hat stress application, which are further split into a *linear and a decay region*. Each measurement consists of 5 top-hat application, and the corresponding strain sections are averaged to obtain a less noisy signal for the fitting routine.

- 'iterative fitting of exponential decay' (Sec. 6.2.3.2): the linear and decay region are fitted with a discontinuous function. The *time constant (τ) (s)* is extracted from the decay region.

A flow-chart of the experimental method to determine the stress, strain, and time constant is presented by Fig. 6.5. As an iterative fitting routine I use again the Levenberg-Marquardt method, which I describe in Sec. 4.4.2. In the following subsections I discuss the methodology of the computational functions specific to the present experiment.
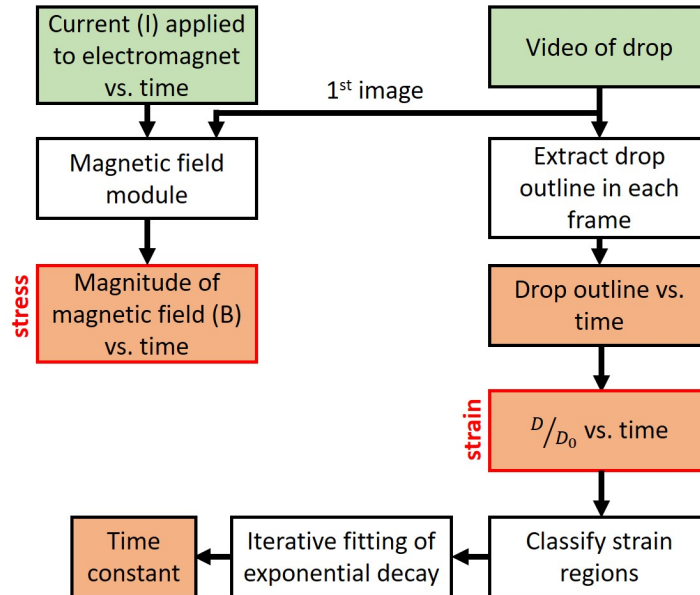
Figure 6.5: Flow-chart of the experimental method to determine the stress, strain, and time constant of a drop.

6.2.3.1 Classify strain regions

To analyse the strain measurements, I separate the data into four regions of interest per top-hat stress application: the initial D/D_0 at 0 T (constant), the decaying D/D_0, the D/D_0 at 0.6 T (constant), and the rising D/D_0. These four regions are treated in two sections: 1. the initial and decaying D/D_0; 2. D/D_0 at 0.6 T and the rising D/D_0. The measured strain in the 2. section is reflected in the time axis, to obtain a decay as in the 1. section. Both sections therefore consist of a linear region and a decay region, as illustrated by Fig. 6.6a).

The start of the decay is found through an automated initial guess. This initial guess is based on a change in slope. Regions with a negative slope are marked as decay regions and further classified into 'real' and 'false' decays, where real decays cross the data mean (the mean of D/D_0 at 0 T and at 0.6 T), and have a minimum length (10 data points). Decay regions that do not cross the data mean and are shorter than the minimum length are classified as false decays. Real decays are caused by the top-hat application of the stress (the magnetic field), whereas false decays are

caused by noise. To ensure a consistently good quality of the exponential fits, the initial guesses of the starts of the real decay regions are checked manually.

The top-hat stress is applied 5 times for each drop, resulting in 5 strain measurements each of the 1. and 2. section. These measurements are averaged to reduce the noise, resulting in one *averaged 1. and 2. section* per drop. An example of an averaged 1. section is shown by Fig. 6.6b).

6.2.3.2   Iterative fitting of exponential decay

The averaged 1. and 2. section are input to this function. Each section can be modelled by a discontinuous function which consists of a linear region and an exponential decay:

$$y(t) = \begin{cases} a_5 & t \leq a_4 \\ a_1 e^{-t/a_2} + a_3 & a_4 \leq t \end{cases} \tag{6.5}$$

where a_1 is the height of the decay or rise, a_2 is the time constant (s), a_3 is the offset of the decay, a_4 is the end of linear region and the begin of the exponential decay (s), and a_5 is the value of D/D_0 in the linear region. When $t = a_2$, then the height of the decay is reduced by $\approx 64\%$.

I use the Levenberg-Marquardt method to optimise the fit function in Eq. 6.5 to fit the strain data. Equation 6.5 is then fitted separately to each section (linear region and decay), where the parameters of the fit equation are determined as follows: a_4 is the start of the decay region, which is determined in 'Classify strain regions' (Sec. 6.2.3.1); a_5 is the mean value of D/D_0 of the linear region which is calculated from the measured data; the height of the decay a_1, the time constant a_2, and the offset a_3 are optimised using the Levenberg-Marquardt method.
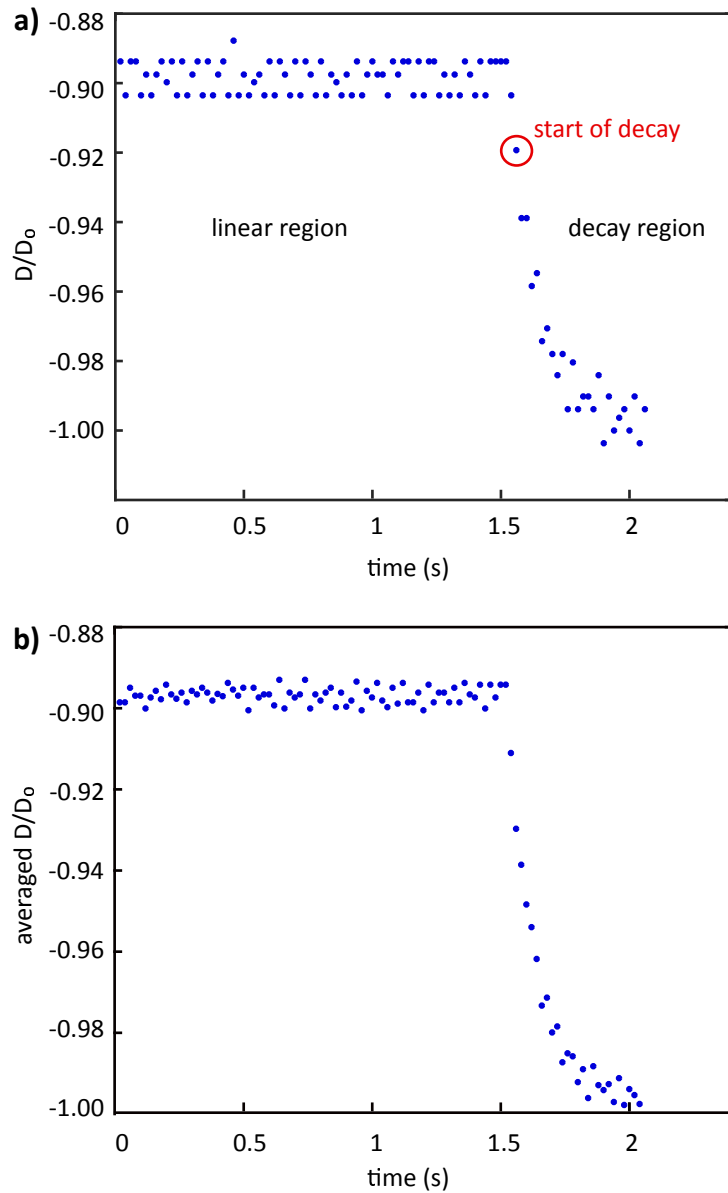
Figure 6.6: Example of the decay of D/D_0 of a paramagnetic drop upon removal of a magnetic field. **a)** D/D_0 decays from -0.9 to -1 upon removal of the magnetic field, meaning that the drop resumes its initial shape. The data can therefore be separated into a linear region and an decay region. The start of the decay region is found automatically and checked manually. **b)** Example of the averaged decay of D/D_0 of a paramagnetic drop. Through the averaging the noise on the data has been visibly reduced.

6.2.4 Results of viscosity characterisation

An example of a measurement of D/D_0 of a 100 µl drop of the solution with 15% ppw $MnCl_2 \cdot 4H_2O$ and 75% ppw glycerol against time is presented by Fig. 6.7. The magnetic field is applied and removed in a manner that is represented by the top-hat function of B(T) in Fig. 6.7. As expected, D/D_0 decreases from its initial value $(D/D_0 = 1 \pm 0.01)$ to a new constant value $(D/D_0 = 0.92 \pm 0.01)$ when the drop elongates due to the application of the magnetic field. Upon removal of the field, the drop relaxes back into its initial shape - D/D_0 increases again to $D/D_0 = 1 \pm 0.01$. The noise on the measurement is caused by a random fluctuations in lighting, which
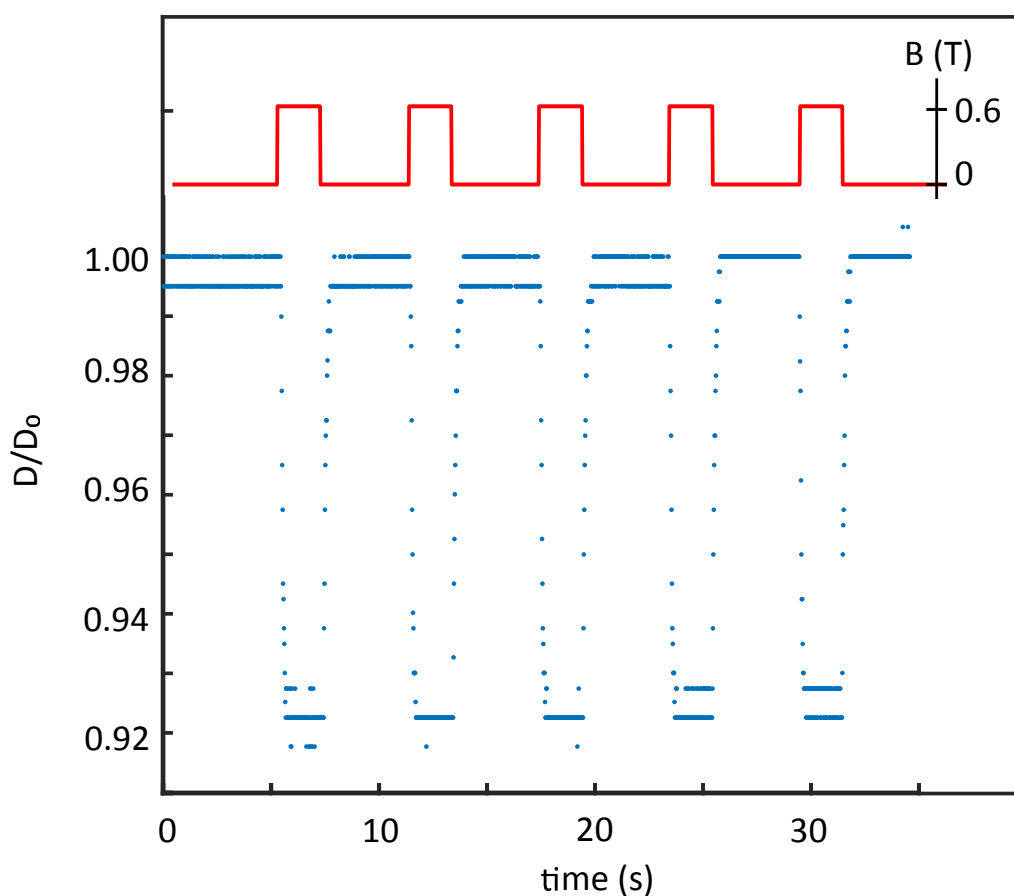
Figure 6.7: Example of the deformation of a drop of an aqueous solution of $MnCl_2 \cdot 4H_2O$ and glycerol. A homogeneous magnetic field is applied to and removed from a 100 µl drop of an aqueous solution of 15% ppw $MnCl_2 \cdot 4H_2O$ and 75% ppw glycerol. The dimensionless parameter D/D_0 - with $D = w - hw + h$, where w is the width and h the height of the drop - is measured at a sample rate of 50 s^{-1}. Upon application of 0.6 T, the drop elongates along the field lines - the height of the drop increases, and the width of the drop decreases - reducing D/D_0. Upon removal of the magnetic field, the drop relaxes back to its initial shape, which is visible in the increase of D/D_0. The time scale of the relaxation is of the order of 100 ms, rather than the 13 ms expected of a relaxation dominated by the viscosity of the fluid.

affects the brightness of pixels and therefore the conversion from a colour image to the binary image on which the outline of the drop is measured.

In this result, it is immediately apparent that the relaxation time of the drop is much longer than anticipated in Tab. 6.1, where the relaxation time for this solution is listed as 13.18 ms. The measured relaxation time can be estimated by counting the number of data points between the end of the linear region and the point at which the drop has relaxed to ≈64% of the total height of the exponential decay, which is ≈5 data points. At a sample rate of $50\ s^{-1}$, this equals 100 ms. This estimate is an order of magnitude larger than the the viscous relaxation time. The relaxation of the drop does therefore not appear to be dominated by the viscosity of the drop.

I determine the relaxation time more accurately by averaging the relaxations and fitting Eq. 6.5 to data, as outlined in Sec. 6.2.3. The response of D/D_0 to the removal of the applied field in Fig. 6.7 is averaged and presented by Fig. 6.8. The averaging has reduced the noise on the data to ±0.03. The fitted Eq. 6.5 is also plotted (red), showing good agreement with the data (blue). The optimised relaxation time of Eq. 6.5 is 112 ms.

Eq. 6.5 is fitted in this manner to the relaxation of drops of the other glycerol solutions as well. The optimised relaxation times, listed in Tab. 6.2, are between 104-128 ms long with no apparent correlation to the viscosity (glycerol concentration)
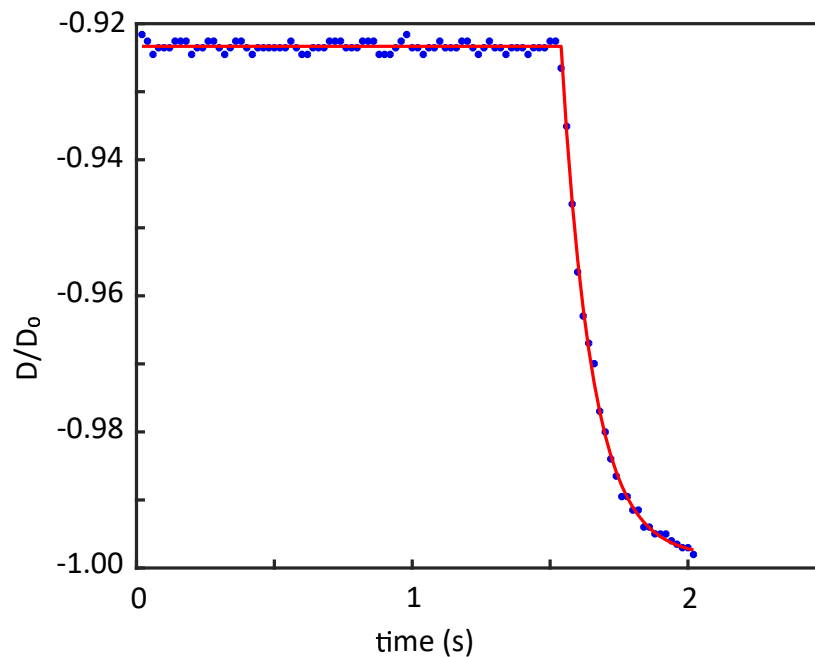
Figure 6.8: Example of the averaged response of D/D_0 to the removal of the applied field from Fig. 6.7. The fitted Eq. 6.5 (red) is in good agreement with the data (blue).

111

Table 6.2: Experimentally obtained relaxation times of aqueous solutions of glycerol and 15% ppw $MnCl_2 \cdot 4H_2O$.

C_g	a_2
% ppw	ms
0	128 ± 10
24	105 ± 2
56	104 ± 3
75	117 ± 3

of the solution. This strengthens the hypothesis that the relaxation of the drop is not dominated by the viscosity of the solution.

Another experimental factor that affects the relaxation of the drop is the decay of the applied magnetic field. I assumed earlier, that the field application and removal of the magnetic field is instantaneous and therefore has the shape of a top-hat function. To test the validity of this hypothesis, I use a Gauss meter to measure the magnetic field as a function of time. The accuracy of the Gauss meter is 1% and its response time is 100 ms, meaning that the reading on the Gauss meter display is updated every 100 ms with an average value that was taken over the past 100 ms. The sample rate at which I read the Gauss meter is 30 s^{-1}. I switch off the voltage on the power supply, which has a reaction time of 100 ms. The reading of the current value on the power supply has an accuracy of 1 mA and a response time of 100 ms.

Fig 6.9 shows the decay of the current and magnetic field after I switch off the voltage of the power supply, wait for the field to settle, switch the voltage back on, wait for the field to settle, and switch the voltage back off. The initial current is 2.5 A and the magnetic field is 0.6 T. Upon removal of the voltage, the current decays exponentially to 0 A. The decay of the magnetic field lacks ≈ 200 ms behind the decay of the current. To estimate the relaxation time of the decay of the magnetic field, I count again the data points between the end of the linear region where $B = 0.6T$ and the point where the field strength is $\approx 64\%$ of the initial field strength. I find ≈ 6 data points on both decays, which - at a sample rate of 30 s^{-1} equals ≈ 200 ms. This observation strengthens the hypothesis that the relaxation of the drop is dominated by the relaxation of the magnetic field. Therefore, the current set-up is unsuitable to measure the relaxation times of aqueous glycerol solutions as proposed in this section.
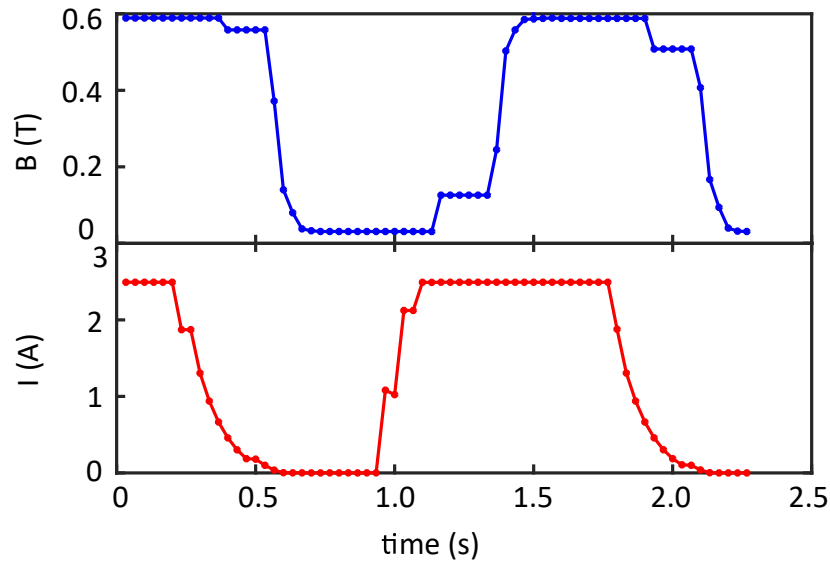
Figure 6.9: Measurement of the settling time of the electromagnet. The magnetic field decays to ≈64% of its initial strength over 200 ms. This time scale dominates the relaxation of the viscous drop.

6.2.5 Conclusion on characterising viscous fluids

In this section, I explored the capabilities of the present set-up for rheological measurements. I measured the strain on drops due to the stress applied on them by a homogeneous magnetic field. For this, I measured the shape of drops of aqueous solutions of glycerol and manganese chloride. Key findings of these measurements are:

- The drops elongate along the direction of the magnetic field lines, as observed in Chapter 5.

- The elongation and relaxation of the drop due to the application and removal of the magnetic field can be sampled by measuring the evolution of the shape of the drop with time.

- The shape detection module of the ADSA-mf algorithm discussed in Sec. 4.4.4 is capable of measuring the shape of the drop in the video frames.

- I developed an algorithm that extracts the relaxation time from the evolution of the dimensionless number D/D_0.

The results of these measurements did not show a relation between the viscosity of the drop and its relaxation time. I identified some limitations of the set-up which make it - in its current form - unsuitable for relaxation time measurements of aqueous glycerol solutions. These limitation include the frame rate of the camera and the

113

decay time of the magnetic field. Based on these observations, I suggest following modifications to the set-up:

- To measure the time constant of a drop with a glycerol concentration of 70% ppw, a camera with a frame rate of at least 1k fps should be used, to ensure a sufficiently large sample rate.

- To ensure that the relaxation of a drop is not dominated by the time scale of the decay of the magnetic field, a magnetic field must be applied that decays faster than the relaxation time of the drop.

While the first modification may be easily achieved since cameras with a faster frame rate are readily available, the second modification may be more difficult to solve and I could not identify a suitable magnet that would fulfil this requirement. With these modifications, shaping of magnetic drops may be an interesting rheological tool, with the benefits of small sample volumes and the flexibility to tune the stress and strain on the drop by adjusting the applied field strength and the magnetic susceptibility of the drop.

6.3 Driving floating objects on a drop

6.3.1 Introduction to driving floating objects using magnetic fields

Floating objects can be controlled using magnetic fields. I highlighted two examples in the introduction (Fig. 2.3), namely the assembly of diamagnetic solids in a bulk paramagnetic fluid, and the movement of floating diamagnetic objects on an air-water interface.

The position of diamagnetic solids in a bulk paramagentic fluid depend on the profile of the applied magnetic field, and the densities of the solids [22]. By choosing a paramagnetic bulk fluid, the difference in magnetic susceptibility between the solid and the surrounding liquid is increased. The application of a non-uniform magnetic field then generates enough force on the solids to cause their travel to the region of lowest magnetic field strength.

At the air-water interface, the movement of floating diamagnetic bodies in a non-uniform magnetic field has been shown to be caused by the deformation of the water through the magnetic field [23, 24]. The direction of movement is set by the contact angle between the water and the floating object.

Another example are micro-rafts for programmable self-assembly at the liquid-vapour interface [113]. Programmable self-assembly means that information about the structure that is being assembled is stored in its individual components. In the case of micro-rafts, this information is a cosinusoidal contour of the top surface edge. The micro-rafts are coated in cobalt, which is a ferromagnet, and are placed on an air-water interface. Rotational motion is induced in the micro-raft through the application of a rotational magnetic field. This motion initiates self-assembly of the rafts into structures such as concentric circles.

6.3.2 Experimental design to driving floating objects on a drop

Here, I explore some fundamental principles of driving floating objects on a liquid-vapour interface. To drive the object directly with a magnetic field - rather than driving the object indirectly through the deformation of the liquid-vapour interface - I chose materials with a sufficiently large difference in magnetic properties, namely a paramagnetic liquid and a diamagnetic floating object. The design of the floating objects is informed by symmetry considerations and I discuss how these can be used to encode information for programmable self-assembly.

The aim of this investigation is to qualitatively explore some design considerations for controlled driving of diamagnetic floating objects on paramagnetic drops. Here, I demonstrate:

- radially symmetric position control in a homogeneous magnetic field;

- control of directionality of positioning by introducing asymmetry to the applied field;

- control of orientation by introducing asymmetry to the floating object.

Radially symmetric position control can be achieved using a drop in a homogeneous magnetic field and a symmetric object, such as illustrated by Fig. 6.10. In the absence of a magnetic field, the equilibrium position of the cube is the apex point of the drop, where the forces acting on the cube (buoyancy, gravity and surface tension) balance. Upon application of a magnetic field, the magnetic stress difference between the paramagnetic drop and the diamagnetic floating object is larger than between the drop and air. As discussed in Ch. 3, the magnetic stress difference across an interface increases with B_n^2 - the vector component of the magnetic field directed along the surface normal of the interface. B_n^2 of the liquid-object interface is largest when the object floats at the apex. The object is driven away from the apex, towards to side of
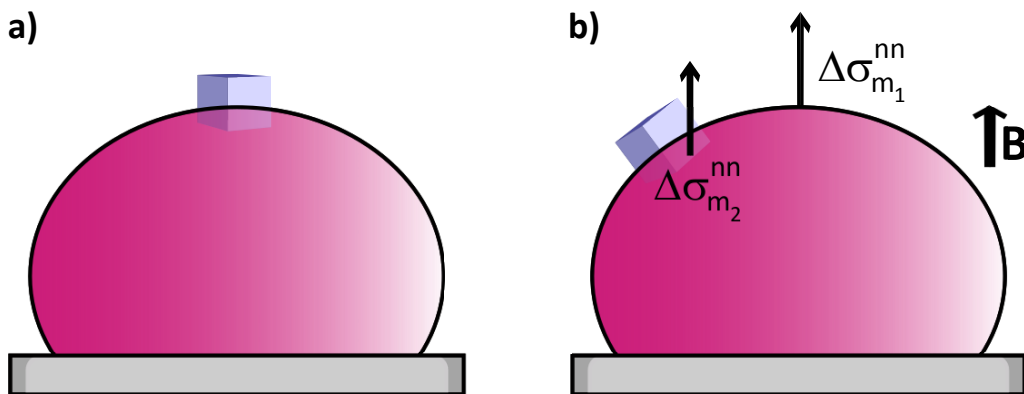
Figure 6.10: Experimental design for radially symmetric position control of a floating object on a drop. **a)** A diamagnetic cube floats on a paramagnetic sessile drop on a hydrophobic substrate. **b)** Upon application of a uniform magnetic field, the magnetic normal stress difference between the drop and the object is larger than between the drop and air. The object is pushed downwards along the liquid-vapour interface of the drop, minimising the object-liquid interface perpendicular to the applied field lines, and therefore the magnetic normal stress difference between the object and the liquid.

the drop, orienting the liquid-object interface parallel to the magnetic field lines, and therefore reducing the magnetic stress difference across the liquid-object interface.

Through the application of a non-uniform magnetic field, the object can be driven on the liquid-vapour interface along a chosen direction - away from the region of highest magnetic field strength.

The orientation of the object can be controlled by introducing asymmetry to its design. Fig. 6.11 shows such an asymmetric design, with a broad body and a slender tail. Again, in the absence of a magnetic field the equilibrium position of the object is at the apex of the drop. Upon application of a magnetic field, the magnetic stress difference across the liquid-object interface is larger at the thick end of the object than at the thin end. In a non-uniform magnetic field, the object therefore reorients such that the thin end points towards the region of highest magnetic field strength.

6.3.3 Experimental method to drive floating objects on a drop

To test these predictions on the control of driving floating objects on a drop, I use two object designs. The symmetric objects are cubes of acrylic (PMMA, $\chi = -9.06 \times 10^{-6}$[114]) with length 2 mm; the asymmetric objects are microfabricated
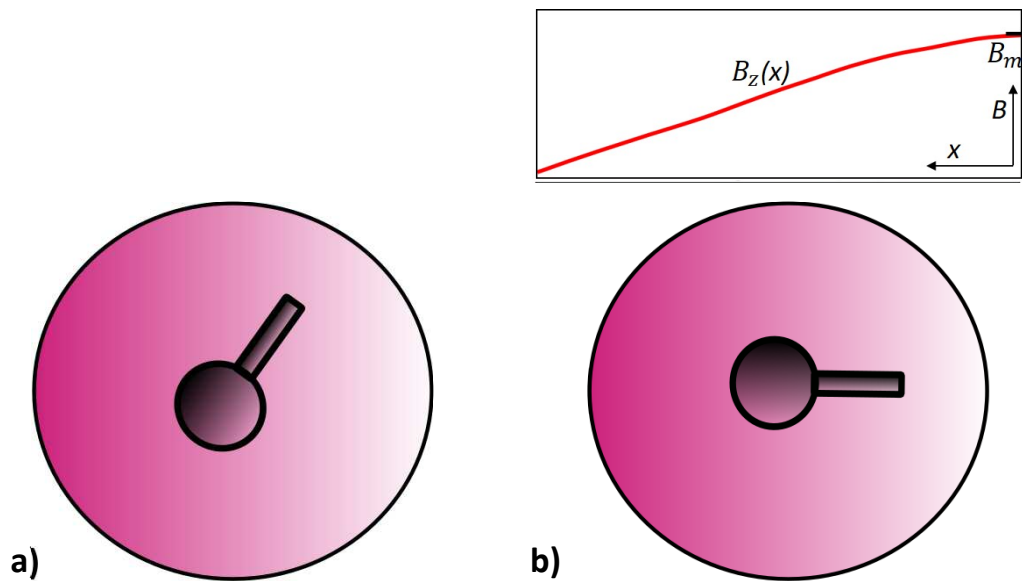
Figure 6.11: Experimental design for orientation control of an asymmetric floating object on a drop. **a)** Bird's-eye view of an asymmetric diamagnetic object on a paramagnetic drop on a superhydrophobic substrate. **b)** A non-uniform magnetic field is applied to the drop, oriented out of the plane and decaying from right to left in field strength. The magnetic normal stress difference across the object-liquid interface is minimised through a rotation of the object that orients the thinner end of the object into the field and the wider end out of the field.

SU-8 structures, coloured with fluorescent marker, as shown by Fig. 6.12. SU-8 is an epoxy-based photoresist. The magnetic susceptibility of epoxy is $\chi_m \approx -6 \times 10^{-7}$ cm^3 g^{-1} [115]. The SU-8 structures were fabricated by Paul Sullivan and myself in the microfabrication facilities of the Scottish Microelectronics Centre. For the measurements in a uniform magnetic field, I use the set-up introduced in Ch. 4 and place the acrylic cubes on 80 µl drops of 50% ppw MnCl$_2 \cdot$4H$_2$O ($\chi = 2 \times 10^{-4}$).

To measure the asymmetric floating objects in a non-uniform magnetic field, I use the set-up shown by Fig. 6.13. The set-up in Fig. 6.13 consists of the same components as the non-uniform magnetic field set-up, with the modification that the drop is placed outside of the homogeneous magnetic field region and the camera records a mirror image of the top of the drop. The drop can be illuminated by either a white or UV light source. The drops are 100 µl drops of 25% ppw MnCl$_2 \cdot$4H$_2$O ($\chi = 2 \times 10^{-4}$).
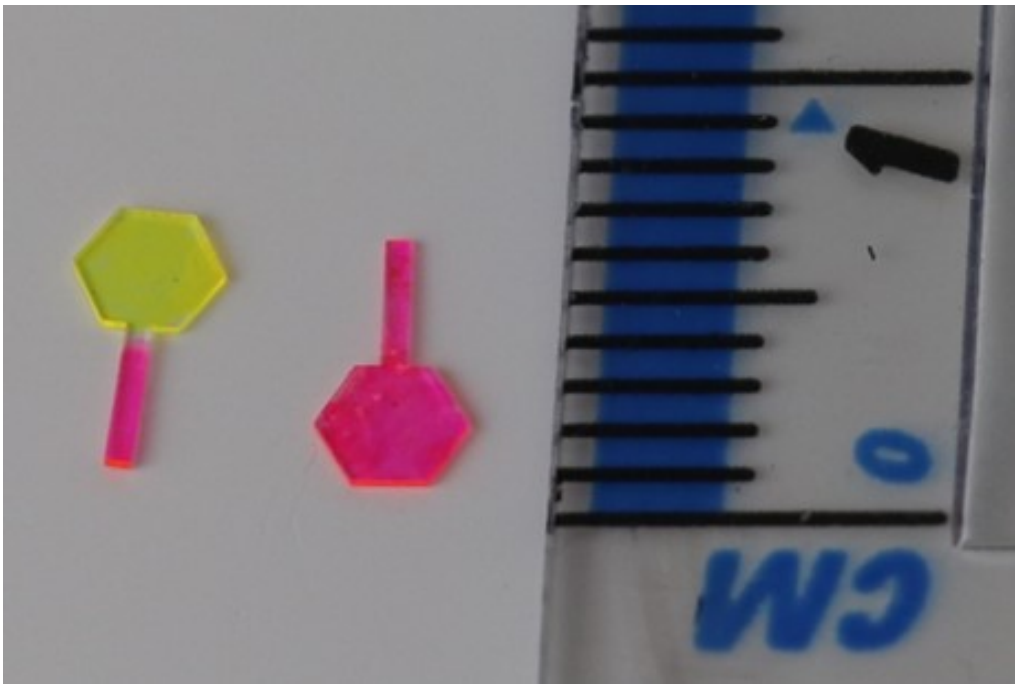
Figure 6.12: Photograph of an asymmetric diamagnetic floating object design. The objects are microfabricated SU-8 structures, which are coloured with fluorescent marker to make them more visible during the orientation measurements.
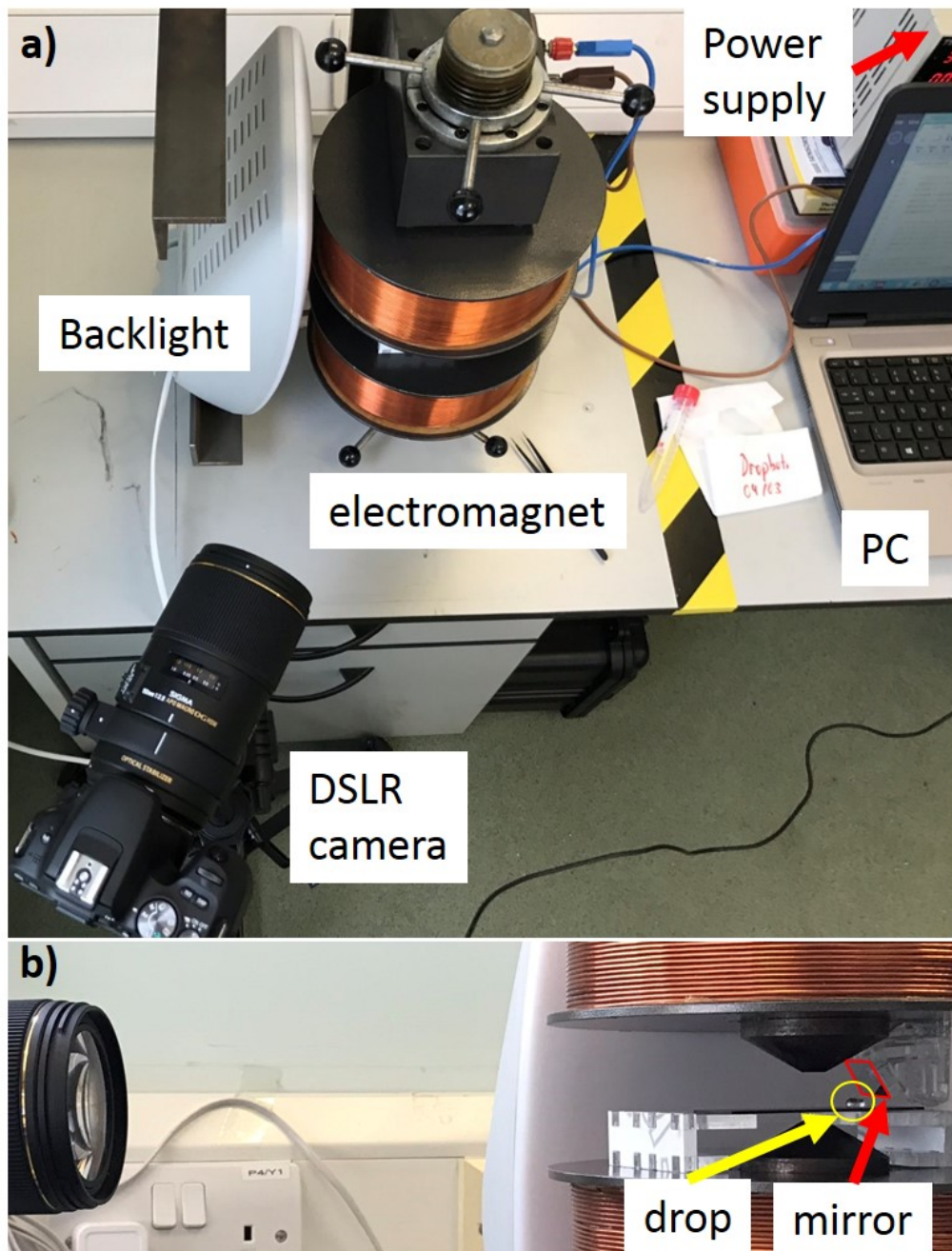
Figure 6.13: Experimental set-up to measure the orientation of floating objects on a drop. **a)** Bird's-eye view of the experimental set-up. The components of the set-up are the same as in Ch. 4, with the addition of a mirror that is used to image the top of the drop. **b)** Side-view of the experimental set-up. The mirror image of the drop is captured with the camera. The drop is illuminated with a white light or a UV light source.

6.3.4 Results of driving floating objects on a drop

Fig. 6.14 shows the acrylic cube on the paramagnetic drop. In the absence of a magnetic field, the acrylic cube is nearly fully submerged in the drop, with the top surface of the cube exposed to air. Upon application of a magnetic field, the cube is driven from the apex to the side of the drop as expected. The position of the cube on the liquid-air interface of the drop depends on the strength of the applied field - the stronger the field, the further the cube is driven from the top. This demonstrates the principle of position control of a floating object using magnetic stress.

When placing the asymmetric floating object on the drop, the drop is deformed such that the floating object is in full contact with the drop, such as shown by Fig. 6.15. This effect is due to the hydrophilicity of the floating object.

Example results of the orientation control tests are shown by Fig. 6.16. Floating objects are shown on drops oriented in different directions in the absence of a magnetic field by Fig. 6.16a) and c). Fig. 6.16b) and d) show the orientation of the floating objects in the presence of a non-uniform magnetic field, which decays from the right- to the left-hand-side of the images as indicated by the field profile. In Fig. 6.16b),
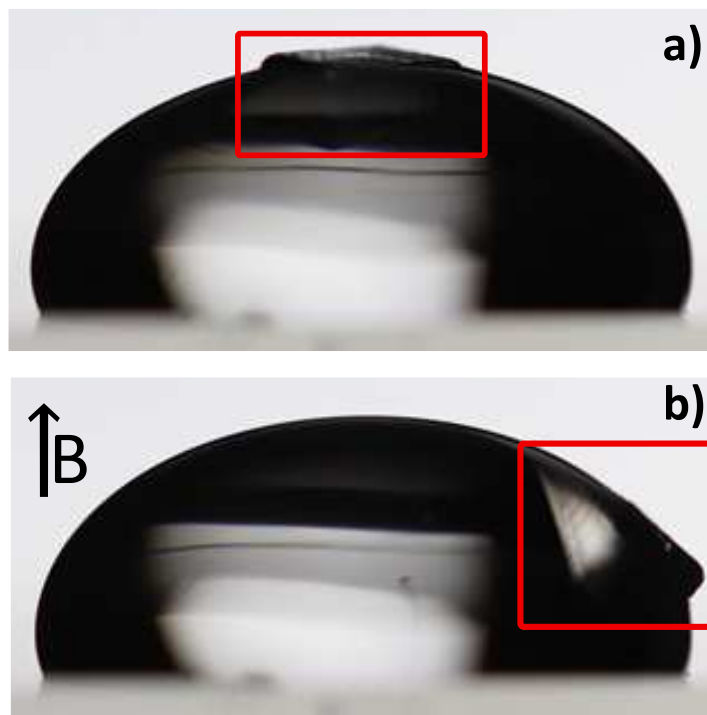
Figure 6.14: Experimental demonstration of position control of a diamagnetic floating object on a paramagnetic drop in a uniform magnetic field. The drop is 80 μl of 50% ppw $MnCl_2 \cdot 4H_2O$. The floating object is a cube of acrylic. **a)** The object floats on top of the drop in the absence of a magnetic field. **b)** In a magnetic field the objects repositions to reduce the magnetic stress across the object-liquid interface.
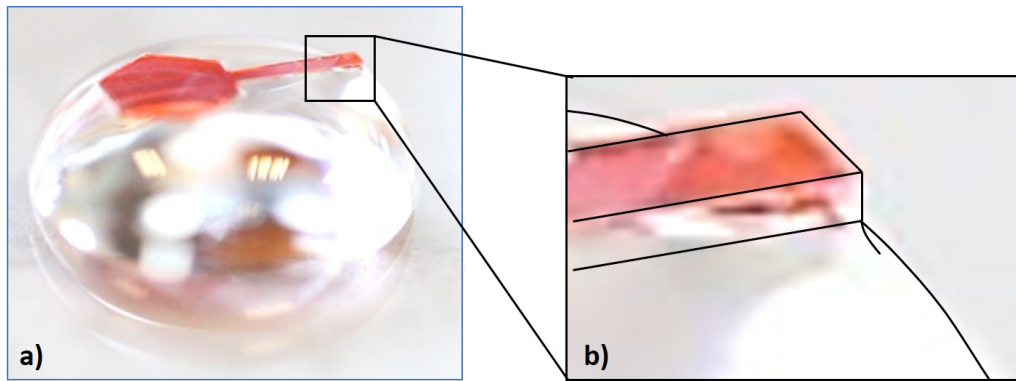
Figure 6.15: An asymmetric object floating on a drop. **a)** Image of the object floating on a drop. **b)**) Illustration of a magnified view of the deformation of the liquid-vapour interface of the drop due to the hydrophilic object.

the module orients, as predicted, such that its thin end points towards to region of highest magnetic field strength. This observation strengthens the hypothesis that the object is driven by the magnetic stress of the object-liquid boundary, which is greater than on the liquid-air boundary.

In Fig. 6.16d) however, the thin end of the object points away from the region of the highest magnetic field strength. This seems on a first glance counter intuitive - the thick end of the module has been driven into the side of the drop exposed to a stronger magnetic field. Since the object is in a quasi-static equilibrium in this orientation, it appears that the energy is minimised. A rotation of the object in either direction would expose more of the liquid-object interface to a stronger magnetic field. The object is therefore caught in a local energetic minimum.

Similar as with the cube in the homogeneous magnetic field, the orientation of the object can be tuned by the strength of the applied field. This tuning is possible because of the surface tension of the liquid-vapour interface of the drop acts as a restoring force on the object, pulling it back to its initial orientation. The following QR code links to a video of this orientation control by a magnetic field.

Orientation control of a solid object on a drop

Above a threshold field strength, the module edges away from the top of the drop and is pushed down the side of the drop, away from the region of highest magnetic field strength. This is again due to $\Delta\sigma_m^{nn}$ larger for object-liquid, than vapour-liquid. There is also a threshold field strength above which the drop unpins from the surface and moves towards the region of highest magnetic field strength.

6.3.5 Conclusion on driving objects on a drop

In this section, I have demonstrated how the position and orientation of diamagnetic objects can be controlled on a paramagnetic drop using a magnetic field. I have found that:

- the directionality of position and orientation can be predetermined through symmetry considerations on the field and the object;

- the amount to which the object is repositioned and reorientated increases with the strength of the magnetic stress difference across the liquid-object interface,
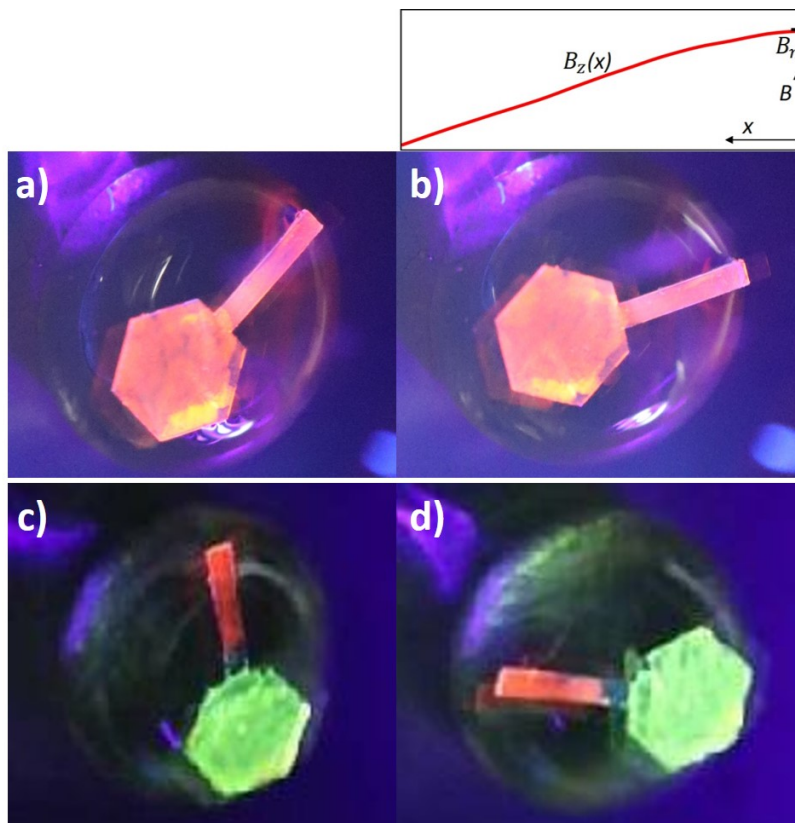
Figure 6.16: Experimental demonstration of orientation control of an asymmetric diamagnetic floating object on a paramagnetic drop with a non-uniform magnetic field. **a)** and **c)** show the orientation of the objects in the absence of a magnetic field. **b)** and **d)** show the objects in their two stable positions in the presence of a non-uniform magnetic field $B_z(x)$. The field has a maximum field strength B_m; is directed along the surface normal of the substrate; and decays in intensity from the right-hand-side of the image to the left-hand-side as illustrated by the field profile. The two stable positions are the global minimum (**b**)) - where the magnetic stress difference across the liquid-object interface is minimised; and a local minimum (**d**)), where any further rotation would increase the magnetic stress difference across the liquid-object interface. The object is 5 mm long.

which can be tuned by the strength of the magnetic field and the magnetic properties of the object and the liquid.

This investigation has exposed the potential of driving objects on drops. Future work should address the design of modules that assemble into more complex structures. Driving objects on drops could be used as a model system to study statistical mechanical processes to understand the dynamics of living systems, such as swarms.

6.4   Summary and conclusion

This chapter explored two application of the shaping of drops with magnetic fields - first as a measurement tool for the rheological properties of fluids; and secondly as a tool for controlled driving of solids along the liquid-vapour interface. In both cases, the magnetic stress differences across the interfaces of the drop is the actuation mechanism, as it was in Ch. 5 to shape and transport a drop. The investigations presented in this chapter show the potential for future work to further develop this technique of using the shaping of drops with magnetic fields for applications.

In the following chapter I conclude this thesis and provide an outlook to future work.

Chapter 7

Conclusion and future work

7.1 Conclusion

In summary, the aim of my PhD research is to investigate the shaping of drops in magnetic fields. This investigation was step-wise, (i) starting with the derivation of an analytical expression for the shape of a drop in a magnetic field, in particular for a para- or diamagentic drop; (ii) then the experimental validation of this analytical expression, and exploration of different cases, such as para- and diamagnetism, variation of the volume and susceptibility of the drops, and variation of the applied field strength, and transport in a non-uniform magnetic field; (iii) finally an exploration of some applications of shaping of drops in magnetic fields, including rheological measurements, and the controlled driving of solids floating on a drop. The main findings of my work include:

- I derived an analytical expression for the shape of para- and diamagnetic drops in a static magnetic field and discussed the limitations of the transferability of this expression to the electric equivalent case. The expression also accurately predicts the transport of drops in a magnetic field.

- I developed a computational package to measure and analyse the shape of a drop in a magnetic field, which can be implemented into standard algorithms in the field.

- I development an experimental method to actuate drops in a magnetic field.

- I demonstrated and characterised shaping of para- and diamagnetic drops with uniform magnetic fields.

- I demonstrated the transport of para- and diamagnetic drops in non-uniform magnetic fields.

- I developed an experimental method to measure the relaxation time of a drop in a magnetic field as a rheological sensing tool, which is limited by the speed of decay of the magnetic field.

- I development an experimental method for controlled driving of diamagnetic solids floating on paramagnetic drops.

7.2 Future directions

1. Time-dependent magnetic phenomena. The analytical model I describe in Ch. 3 is valid for static fields, but can be adapted to time-dependent magnetic fields by using the time-dependent electromagnetic stress tensor. The experimental study of the behaviour of drops in static magnetic fields can also be adapted to time-dependent magnetic fields, such as by using a suitable electromagnet, and would allow the study of the frequency-dependence of the magnetic susceptibility.

2. Measurements of the relaxation time of a drop. In Ch. 6 I develop an experimental method to measure the relaxation time of a drop as a rheological sensing tool. I discuss how the frame rate of the camera and settling time of the electromagnet are in the present set-up the limiting factors in the relaxation of the drop. A camera with a frame rate of at least 1k fps is required to measure the relaxation time of a drop with 70% ppw glycerol. The magnetic field must decay faster than the relaxation time of the drop, which I have identified as a design challenge.

3. Study of dynamics of solids floating on drops. In Ch. 6 I introduce diamagnetic floating objects to paramagnetic drops and show how symmetry considerations can be used to orient and position them. This principle can be build upon by optimising the experimental design to study the dynamics of solids floating on drops, where the dynamics of both, the solids and the drops, are controlled and studied. This may be an interesting model for statistical mechanical processes, such as found in living systems.

7.3 Impact of work

This work is a detailed study of induced magnetism, which has not been published in this extend before. In this work, I have explicitly demonstrated and analysed the deformation of drops due to induced magnetism and therefore contributed of the discussion of this phenomenon by providing evidence of the linear relation between the change in shape and the applied field squared. I have also explicitly demonstrated

the change in shape of a diamagnetic drop in air, contributing to the discussion of diamagnetic phenomena and their use in microfluidics.

This work demonstrated that induced magnetism offers ample opportunity integration into DMF devices and explicitly draws attention to the similarities and differences between electric and magnetic actuation techniques of fluids. My work highlights in particular that: (i) Magnetic actuation techniques remove the necessity of contact between drops and electrodes, such as required in EWOD. (ii) In contrast to the abundance of diamagnetic materials, there are no natural materials known with a negative electric susceptibility. Magnetic actuation techniques can therefore exploit diamagnetism and paramagnetism in the same set-up for applications such as sorting. My work on the shape of diamagnetic drops and the control of diamagnetic objects contribute to the understanding of these control techniques. (iii) My exploration of using induced magnetism for rheological measurements contributes to the discussion of microrheological techniques. The small sample sizes required make this technique particularly appealing for biomedical applications, where for example the rheological properties of blood or other bodily fluids are measured, and sample sizes are naturally limited. I highlighted issues with the speed of decay of the magnetic field, which is an inherent disadvantage of electric actuation techniques where fields are altered much faster (AC currents). (iv) In vitro, magnetic fields are already routinely applied, such as in MRI, and are a promising candidate for cutting-edge applications, such as the control of microrobots. I explore aspects of this novel application through the demonstration of controlled driving of floating objects on a drop. My findings on (a) the dependence of the strength of control on the magnetic stress differences between the module, the drop, and the surrounding medium may inform material requirements of microrobots and their host fluids; (b) the dependence of orientation and position control on the symmetry of the floating object and the applied field may inform the design of the actuation mechanism and of microrobots or their constituent parts.

References

[1] T. K. Simpson, *Maxwell's mathematical rhetoric : rethinking the Treatise on electricity and magnetism.* Santa Fe, N.M.: Green Lion Press, 2010.

[2] J. C. Maxwell, *A treatise on electricity and magnetism.* New York, N.Y.: Dover Publications, unabridged ed., 1954.

[3] M. Faraday, *Experimental researches in electricity.* Mineola, N.Y.: Dover Publications, 2004.

[4] R. P. Feynman, R. B. Leighton, and M. Sands, *The Feynman lectures on physics*, vol. II. London: Addison-Wesley Pub. Co., 1963.

[5] D. A. Fleisch, *A student's guide to Maxwell's equations.* Cambridge: Cambridge University Press, 2008.

[6] R. Pethig and S. Smith, *Introductory bioelectronics for engineers and physical scientists.* Chichester: John Wiley & Sons, Inc., first ed., 2013.

[7] D. Günther, "Schrottsortierung in magnetischen Flüssigkeiten," *Physik in unserer Zeit*, vol. 26, no. 3, pp. 124–128, 1995.

[8] G. M. Whitesides, "The origins and the future of microfluidics," *Nature*, vol. 442, no. 7101, pp. 368–373, 2006.

[9] T. M. Squires and S. T. Quake, "Microfluidics: Fluid physics at the nanoliter scale," *Reviews of Modern Physics*, vol. 77, pp. 977–1026, 2005.

[10] F. Mugele and J.-C. Baret, "Electrowetting: from basics to applications," *Journal of Physics: Condensed Matter*, vol. 17, no. 28, pp. R705–R774, 2005.

[11] K. Mishra, D. van den Ende, and F. Mugele, "Recent developments in optofluidic lens technology," *Micromachines*, vol. 7, no. 6, pp. 1–24, 2016.

[12] M. G. Lippmann, "Relations entre les phenomenes electriques et capillaires," *Annales de Chimie et de Physique, 5 serie, t. V*, 1875.

[13] H. Pellat, "Measure de la force agissant sur les dielectriques liquides non electrises places dans un champ electrique," *Comptes rendus hebdomadaires des séances de l' Académie des sciences, Série B*, vol. 123, pp. 691–694, 1896.

[14] D. B. McLay and H. M. Johnson, "Measurement of Magnetic Susceptibilities by the Quincke Method," *American Journal of Physics*, vol. 31, no. 6, pp. 457–458, 1963.

[15] L. F. Bates, *Modern magnetism*. Cambridge: University Press, third edit ed., 1951.

[16] V. K. Patel and J. Seyed-Yagoobi, "Combined Dielectrophoretic and Electrohydrodynamic Conduction Pumping for Enhancement of Liquid Film Flow Boiling," *Journal of Heat Transfer*, vol. 139, no. 6, pp. 1–9, 2017.

[17] R. Pethig, "Review—Where Is Dielectrophoresis (DEP) Going?," *Journal of The Electrochemical Society*, vol. 164, no. 5, pp. 3049–3055, 2017.

[18] M. P. Hughes, "Fifty years of dielectrophoretic cell separation technology," *Biomicrofluidics*, vol. 10, no. 3, 2016.

[19] H. A. Pohl and I. Hawk, "Separation of Living and Dead Cells by Dielectrophoresis," *Science*, vol. 152, no. 3722, pp. 647–649, 1966.

[20] A. R. Bausch, W. Möller, and E. Sackmann, "Measurement of local viscoelasticity and forces in living cells by magnetic tweezers," *Biophysical Journal*, vol. 76, no. 1 I, pp. 573–579, 1999.

[21] K. a. Mirica, S. S. Shevkoplyas, S. T. Phillips, M. Gupta, and G. M. Whitesides, "Measuring Densities of Solids and Liquids Using Magnetic Levitation : Fundamentals," *J. Am. Chem. Soc.*, vol. 131, no. 1, pp. 10049–10058, 2009.

[22] K. A. Mirica, F. Ilievski, A. K. Ellerbee, S. S. Shevkoplyas, and G. M. Whitesides, "Using magnetic levitation for three dimensional self-assembly," *Advanced Materials*, vol. 23, no. 36, pp. 4134–4140, 2011.

[23] M. Frenkel, V. Danchuk, V. Multanen, I. Legchenkova, Y. Bormashenko, O. Gendelman, and E. Bormashenko, "Toward an Understanding of Magnetic Displacement of Floating Diamagnetic Bodies, I: Experimental Findings," *Langmuir*, vol. 34, no. 22, pp. 6388–6395, 2018.

[24] O. Gendelman, M. Frenkel, V. Fliagin, N. Ivanova, V. Danchuk, I. Legchenkova, A. Vilk, and E. Bormashenko, "Study of the displacement of floating diamagnetic bodies by a magnetic field," *Surface Innovations*, vol. 7, no. 3-4, pp. 194–202, 2019.

[25] S.-Y. Teh, R. Lin, L.-H. Hung, and A. P. Lee, "Droplet microfluidics," *Lab on a Chip*, vol. 8, no. 2, pp. 198–220, 2008.

[26] R. Seemann, M. Brinkmann, T. Pfohl, and S. Herminghaus, "Droplet based microfluidics," *Reports on Progress in Physics*, vol. 75, no. 1, pp. 016601–1 – 016601–41, 2012.

[27] K. Choi, A. H. Ng, R. Fobel, and A. R. Wheeler, "Digital Microfluidics," *Annual Review of Analytical Chemistry*, vol. 5, no. 1, pp. 413–440, 2012.

[28] E. M. Miller and A. R. Wheeler, "Digital bioanalysis," *Analytical and Bioanalytical Chemistry*, vol. 393, no. 2, pp. 419–426, 2009.

[29] M. J. Jebrail and A. R. Wheeler, "Let's get digital: Digitizing chemical biology with microfluidics," *Current Opinion in Chemical Biology*, vol. 14, no. 5, pp. 574–581, 2010.

[30] S. L. S. Freire, "Perspectives on digital microfluidics," *Sensors and Actuators, A: Physical*, vol. 250, pp. 15–28, 2016.

[31] A. Wixforth, "Acoustically Driven Programmable Microfluidics for Biological and Chemical Applications," *Journal of Laboratory Automation*, vol. 11, no. 6, pp. 399–405, 2006.

[32] T. Franke, S. Braunmüller, L. Schmid, A. Wixforth, and D. A. Weitz, "Surface acoustic wave actuated cell sorting (SAWACS)," *Lab on a Chip*, vol. 10, no. 6, pp. 789–794, 2010.

[33] A. Egatz-Gómez, S. Melle, A. A. García, S. A. Lindsay, M. Márquez, P. Domínguez-García, M. A. Rubio, S. T. Picraux, J. L. Taraci, T. Clement, D. Yang, M. A. Hayes, and D. Gust, "Discrete magnetic microfluidics," *Applied Physics Letters*, vol. 89, no. 3, pp. 034106–1 – 034106–3, 2006.

[34] S. Lindsay, T. Vázquez, A. Egatz-Gómez, S. Loyprasert, A. A. Garcia, and J. Wang, "Discrete microfluidics with electrochemical detection," *Analyst*, vol. 132, no. 5, pp. 412–416, 2007.

[35] U. Lehmann, S. Hadjidj, V. K. Parashar, C. Vandevyver, A. Rida, and M. A. M. Gijs, "Two-dimensional magnetic manipulation of microdroplets on a chip as a platform for bioanalytical applications," *Sensors and Actuators, B: Chemical*, vol. 117, no. 2, pp. 457–463, 2006.

[36] Y. Zhang and N.-T. Nguyen, "Magnetic digital microfluidics – a review," *Lab Chip*, vol. 17, no. 6, pp. 994–1008, 2017.

131

[37] A. Munaz, M. J. A. Shiddiky, and N.-t. Nguyen, "Recent advances and current challenges in magnetophoresis based micro magnetofluidics," *Biomicrofluidics*, vol. 12, pp. 031501–1 – 031501–21, 2018.

[38] G. Chen, B. Ji, Y. Gao, C. Wang, J. Wu, B. Zhou, and W. Wen, "Towards the rapid and efficient mixing on 'open-surface' droplet-based microfluidics via magnetic actuation," *Sensors and Actuators, B: Chemical*, vol. 286, no. January, pp. 181–190, 2019.

[39] S. K. Cho, H. Moon, and C. J. Kim, "Creating, transporting, cutting, and merging liquid droplets by electrowetting-based actuation for digital microfluidic circuits," *Journal of Microelectromechanical Systems*, vol. 12, no. 1, pp. 70–80, 2003.

[40] W. C. Nelson and C. J. C. Kim, "Droplet actuation by electrowetting-on-dielectric (EWOD): A review," *Journal of Adhesion Science and Technology*, vol. 26, no. 12-17, pp. 1747–1771, 2012.

[41] T. B. Jones, "Liquid dielectrophoresis on the microscale," *Journal of Electrostatics*, vol. 51-52, no. 1-4, pp. 290–299, 2001.

[42] P. R. Gascoyne, J. V. Vykoukal, J. A. Schwartz, T. J. Anderson, D. M. Vykoukal, K. W. Current, C. McConaghy, F. F. Becker, and C. Andrews, "Dielectrophoresis-based programmable fluidic processors," *Lab on a Chip*, vol. 4, no. 4, pp. 299–309, 2004.

[43] G. McHale, C. V. Brown, M. I. Newton, G. G. Wells, and N. Sampara, "Dielectrowetting driven spreading of droplets," *Physical Review Letters*, vol. 107, no. 18, pp. 186101–2 – 186101–4, 2011.

[44] H. Geng, J. Feng, L. M. Stabryla, and S. K. Cho, "Dielectrowetting manipulation for digital microfluidics: creating, transporting, splitting, and merging of droplets," *Lab on a Chip*, vol. 17, no. 6, pp. 1060–1068, 2017.

[45] F. Mugele, "Droplet motion electrically controlled," *Nature*, vol. 572, no. 7770, pp. 445–446, 2019.

[46] B. Berge, "Electrocapillarite et mouillage de films isolants par l'eau," *Comptes Rendus de L'Academie des Sciences Paris, Serie, II*, vol. 317, pp. 157–163, 1993.

[47] H. J. Verheijen and M. W. Prins, "Reversible electrowetting and trapping of charge: Model and experiments," *Langmuir*, vol. 15, no. 20, pp. 6616–6620, 1999.

[48] E. N. Latip, L. Coudron, M. B. McDonnell, I. D. Johnston, D. K. McCluskey, R. Day, and M. C. Tracey, "Protein droplet actuation on superhydrophobic

surfaces: A new approach toward anti-biofouling electrowetting systems," *RSC Advances*, vol. 7, no. 78, pp. 49633–49648, 2017.

[49] J. Li, N. S. Ha, T. L. Liu, R. M. van Dam, and C.-J. 'CJ' Kim, "Ionic-surfactant-mediated electro-dewetting for digital microfluidics," *Nature*, vol. 572, no. 7770, pp. 507–510, 2019.

[50] P. Aussillous and D. Quere, "Liquid marbles," *Nature*, vol. 411, pp. 924–927, 2001.

[51] E. Bormashenko, R. Pogreb, R. Balter, O. Gendelman, and D. Aurbach, "Composite non-stick droplets and their actuation with electric field," *Applied Physics Letters*, vol. 100, no. 15, pp. 1–6, 2012.

[52] D. F. Evans, "The Determination of the Paramagnetic Susceptibility of Substances in Solution by Nuclear Magnetic Resonance," *J. Chem. Soc.*, pp. 2003–2005, 1959.

[53] M. McElfresh, *Fundamentals of Magnetism and Magnetic Measurements*. Quantum Design, 1994.

[54] L. Huang, T. Hädrich, and D. L. Michels, "On the accurate large-scale simulation of ferrofluids," *ACM Transactions on Graphics*, vol. 38, no. 4, pp. 1–15, 2019.

[55] L. Liang, C. Zhang, and X. Xuan, "Enhanced separation of magnetic and diamagnetic particles in a dilute ferrofluid," *Applied Physics Letters*, vol. 102, no. 23, pp. 1–5, 2013.

[56] M. V. Berry and A. K. Geim, "Of flying frogs and levitrons," *European Journal of Physics*, vol. 18, no. 4, pp. 307–313, 1997.

[57] M. D. Tarn, L. T. Elders, S. A. Peyman, and N. Pamme, "Diamagnetic repulsion of particles for multilaminar flow assays," *RSC Advances*, vol. 5, no. 126, pp. 103776–103781, 2015.

[58] E. Bormashenko, "Moses effect: physics and applications," *Advances in Colloid and Interface Science*, vol. 269, pp. 1–6, 2019.

[59] D. Laumann, "Even Liquids Are Magnetic: Observation of the Moses Effect and the Inverse Moses Effect," *The Physics Teacher*, vol. 56, no. 6, pp. 352–354, 2018.

[60] M. Latikka, M. Backholm, J. V. Timonen, and R. H. Ras, "Wetting of ferrofluids: Phenomena and control," *Current Opinion in Colloid and Interface Science*, vol. 36, no. January, pp. 118–129, 2018.

[61] K. Smistrup, O. Hansen, H. Bruus, and M. F. Hansen, "Magnetic separation in microfluidic systems using microfabricated electromagnets - Experiments and

simulations," *Journal of Magnetism and Magnetic Materials*, vol. 293, no. 1, pp. 597–604, 2005.

[62] Z. Long, A. M. Shetty, M. J. Solomon, and R. G. Larson, "Fundamentals of magnet-actuated droplet manipulation on an open hydrophobic surface," *Lab on a Chip*, vol. 9, no. 11, pp. 1567–1575, 2009.

[63] Y. Zhao, Z. Xu, M. Parhizkar, J. Fang, X. Wang, and T. Lin, "Magnetic liquid marbles, their manipulation and application in optical probing," *Microfluidics and Nanofluidics*, vol. 13, no. 4, pp. 555–564, 2012.

[64] L. Mats, F. Logue, and R. D. Oleschuk, ""particle-Free" Magnetic Actuation of Droplets on Superhydrophobic Surfaces Using Dissolved Paramagnetic Salts," *Analytical Chemistry*, vol. 88, no. 19, pp. 9486–9494, 2016.

[65] K. S. Seo, R. Wi, S. G. Im, and D. H. Kim, "A superhydrophobic magnetic elastomer actuator for droplet motion control," *Polymers for Advanced Technologies*, vol. 24, no. 12, pp. 1075–1080, 2013.

[66] W. Wang, J. V. I. Timonen, A. Carlson, D.-M. Drotlef, C. T. Zhang, S. Kolle, A. Grinthal, T.-S. Wong, B. Hatton, S. H. Kang, S. Kennedy, J. Chi, R. Thomas Blough, M. Sitti, L. Mahadevan, and J. Aizenberg, "Multifunctional ferrofluid-infused surfaces with reconfigurable multiscale topography," *Nature*, vol. 559, pp. 77–82, 2018.

[67] E. Bormashenko, R. Pogreb, Y. Bormashenko, A. Musin, and T. Stein, "New investigations on ferrofluidics: Ferrofluidic marbles and magnetic-field-driven drops on superhydrophobic surfaces," *Langmuir*, vol. 24, no. 21, pp. 12119–12122, 2008.

[68] W. H. Koh, K. S. Lok, and N. T. Nguyen, "A digital micro magnetofluidic platform for lab-on-a-chip applications," *Journal of Fluids Engineering, Transactions of the ASME*, vol. 135, no. 2, pp. 1–6, 2013.

[69] I. F. Lyuksyutov, D. G. Naugle, and K. D. Rathnayaka, "On-chip manipulation of levitated femtodroplets," *Applied Physics Letters*, vol. 85, no. 10, pp. 1817–1819, 2004.

[70] S. M. Saad and A. W. Neumann, "Axisymmetric Drop Shape Analysis (ADSA): An Outline," *Advances in Colloid and Interface Science*, vol. 238, pp. 62–87, 2016.

[71] J. D. Sherwood, "Breakup of fluid droplets in electric and magnetic fields," *Journal of Fluid Mechanics*, vol. 188, pp. 133–146, 1988.

[72] O. A. Basaran and F. K. Wohlhuter, "Effect of nonlinear polarization on shapes and stability of pendant and sessile drops in an electric (magnetic) field," *Journal of Fluid Mechanics*, vol. 244, pp. 1–16, 1992.

[73] L. T. Corson, C. Tsakonas, B. R. Duffy, N. J. Mottram, I. C. Sage, C. V. Brown, and S. K. Wilson, "Deformation of a nearly hemispherical conducting drop due to an electric field: Theory and experiment," *Physics of Fluids*, vol. 26, no. 12, pp. 122106–1 – 122106–19, 2014.

[74] F. Sauer and R. Schlogel, "Torques exerted on cylinders and spheres by external electromagnetic fields: a contribution to the theory of field induced cell rotation," in *Interactions between electromagnetic fields and cells* (A. Chiabrera, C. Nicolini, and H. P. Schwan, eds.), pp. 203–251, Plenum Publishing Corporation, 1985.

[75] T. B. Jones, "On the relationship of dielectrophoresis and electrowetting," *Langmuir*, vol. 18, no. 11, pp. 4437–4443, 2002.

[76] X. Wang, X.-B. Wang, and P. R. Gascoyne, "General expressions for dielectrophoretic force and electrorotational torque derived using the Maxwell stress tensor method," *Journal of Electrostatics*, vol. 39, no. 4, pp. 277–295, 1997.

[77] T. B. Jones, K. L. Wang, and D. J. Yao, "Frequency-dependent electromechanics of aqueous liquids: Electrowetting and dielectrophoresis," *Langmuir*, vol. 20, no. 7, pp. 2813–2818, 2004.

[78] R. E. Rosensweig, *Ferrohydrodynamics.* Cambridge University Press, 1985.

[79] J. C. Bacri and D. Salin, "Instability of ferrofluid magnetic drops under magnetic field," *Journal de Physique Lettres*, vol. 43, no. 17, pp. 649–654, 1982.

[80] O. E. Sero-Guillaume, D. Zouaoui, D. Bernardin, J. P. Brancher, O. E. Séro-Guillaume, D. Zouaoui, D. Bernardin, and J. P. Brancher, "The shape of a magnetic liquid drop," *Journal of Fluid Mechanics*, vol. 241, no. 18, pp. 215–232, 1992.

[81] H. A. Stone, J. R. Lister, and M. P. Brenner, "Drops with conical ends in electric and magnetic fields," *Proceedings of the Royal Society A: Mathematical, Physical and Engineering Sciences*, vol. 455, no. 1981, pp. 329–347, 1999.

[82] S. Afkhami, A. J. Tyler, Y. Renardy, M. Renardy, T. G. St. Pierre, R. C. Woodward, and J. S. Riffle, "Deformation of a hydrophobic ferrofluid droplet suspended in a viscous medium under uniform magnetic fields," *Journal of Fluid Mechanics*, vol. 663, pp. 358–384, 2010.

[83] P. Rowghanian, C. D. Meinhart, and O. Campàs, "Dynamics of ferrofluid drop deformations under spatially uniform magnetic fields," *Journal of Fluid Mechanics*, vol. 802, pp. 245–262, 2016.

[84] K. Stierstadt and M. Liu, "Maxwell's stress tensor and the forces in magnetic liquids," *ZAMM Zeitschrift fur Angewandte Mathematik und Mechanik*, vol. 95, no. 1, pp. 4–37, 2015.

[85] L. D. Landau, E. M. Lifshitz, and L. P. Pitaevskii, *Electrodynamics of continuous media*. Oxford: Pergamon Press, second ed., 1984.

[86] M. Liu and K. Stierstadt, "Thermodynamics, electrodynamics, and ferrofluid dynamics," in *Odenbach S. (eds) Colloidal Magnetic Fluids. Lecture Notes in Physics*, vol. 763, pp. 83–156, 2009.

[87] S. Blundell, *Magnetism in condensed matter*. Oxford: Oxford University Press, 2001.

[88] G. K. Batchelor, *An Introduction to Fluid Dynamics*. Cambridge: Cambridge University Press, 2000.

[89] C. A. Miller and P. Neogi, *Interfacial phenomena : equilibrium and dynamic effects*. Surfactant science series ; v. 139, London: CRC Press, 2nd ed., 2008.

[90] A. W. Adamson, *Physical chemistry of surfaces*. New York: John Wiley & Sons, Inc., fifth ed., 1990.

[91] V. A. Lubarda and K. A. Talke, "Analysis of the equilibrium droplet shape based on an ellipsoidal droplet model," *Langmuir*, vol. 27, no. 17, pp. 10705–10713, 2011.

[92] W. J. Duffin, *Electricity and magnetism*. London: McGraw-Hill, fourth ed., 1990.

[93] G. I. Taylor, "Studies in Electrohydrodynamics . I . The Circulation Produced in a Drop by Electrical," *Proceedings of the Royal Society of London. Series A, Mathematical and Physical Sciences*, vol. 291, no. 1425, pp. 159–166, 1966.

[94] J. R. Melcher and G. I. Taylor, "Electrohydrodynamics: A Review of the Role of Interfacial Shear Stresses," *Annual Review of Fluid Mechanics*, vol. 1, no. 1, pp. 111–146, 1969.

[95] J. Dodoo, G. McHale, and A. A. Stokes, "Shaping of sessile magnetic drops due to electromagnetic stress," 2019.

[96] L. T. Corson, C. Tsakonas, B. R. Duffy, N. J. Mottram, I. C. Sage, C. V. Brown, and S. K. Wilson, "Deformation of a nearly hemispherical conducting drop due to an electric field: Theory and experiment," *Physics of Fluids*, vol. 26, no. 12, pp. 1–20, 2014.

[97] J. R. Rumble, "Physical constants of inorganic compounds," in *CRC Handbook of Chemistry and Physics, 99th Edition (Internet Version 2018)*, Boca Raton, FL: CRC Press/Taylor & Francis.

[98] I. S. Bayer, V. Caramia, D. Fragouli, F. Spano, R. Cingolani, and A. Athanassiou, "Electrically conductive and high temperature resistant superhydrophobic composite films from colloidal graphite," *Journal of Materials Chemistry*, vol. 22, no. 5, pp. 2057–2062, 2012.

[99] H. P. Gavin, "The Levenberg-Marquardt method for nonlinear least squares curve-fitting problems," pp. 1–19, 2017.

[100] N. T. Nguyen, "Deformation of ferrofluid marbles in the presence of a permanent magnet," *Langmuir*, vol. 29, no. 45, pp. 13982–13989, 2013.

[101] J. B. Hasted, D. M. Ritson, and C. H. Collie, "Dielectric properties of aqueous ionic solutions. Parts I and II," *The Journal of Chemical Physics*, vol. 16, no. 1, pp. 1–21, 1948.

[102] L. J. Struble and X. Ji, "Rheology," in *Handbook of Analytical Techniques in Concrete Science and Technology* (V. S. Ramachandran and J. J. Beaudoin, eds.), ch. 9, pp. 333–367, Norwich: William Andrew Publishing/Noyes Publications, 2001.

[103] D. T. N. Chen, Q. Wen, P. A. Janmey, J. C. Crocker, and A. G. Yodh, "Rheology of Soft Materials," *Annu. Rev. Condens. Matter Phys.*, vol. 1, pp. 301–322, 2010.

[104] M. Oroian, S. Amariei, I. Escriche, and G. Gutt, "Rheological Aspects of Spanish Honeys," *Food and Bioprocess Technology*, vol. 6, no. 1, pp. 228–241, 2013.

[105] B. Yoo, "Effect of temperature on dynamic rheology of Korean honeys," *Journal of Food Engineering*, vol. 65, no. 3, pp. 459–463, 2004.

[106] M. Witczak, L. Juszczak, and D. Gałkowska, "Non-Newtonian behaviour of heather honey," *Journal of Food Engineering*, vol. 104, no. 4, pp. 532–537, 2011.

[107] F. MacKintosh and C. F. Schmidt, "Microrheology," *Current Opinion in Colloid & Interface Science*, vol. 4, pp. 300–307, 1999.

[108] T. A. Waigh, "Microrheology of complex fluids," *Reports on Progress in Physics*, vol. 68, pp. 685–742, 2005.

[109] T. M. Squires and T. G. Mason, "Fluid Mechanics of Microrheology," *Annual Review of Fluid Mechanics*, vol. 42, no. 1, pp. 413–438, 2010.

[110] L. G. Wilson and W. C. Poon, "Small-world rheology: An introduction to probe-based active microrheology," *Physical Chemistry Chemical Physics*, vol. 13, no. 22, pp. 10617–10630, 2011.

[111] J. Vincent, "Basic Elasticity and Viscoelasticity," in *Structural Biomaterials*, vol. 3, pp. 1–28, Princeton University Press, 2012.

[112] A. Volk and C. J. Kähler, "Density model for aqueous glycerol solutions," *Experiments in Fluids*, vol. 59, no. 5, pp. 1–4, 2018.

[113] W. Wang, J. Giltinan, S. Zakharchenko, and M. Sitti, "Dynamic and programmable self-assembly of micro-rafts at the air-water interface," *Science Advances*, vol. 3, no. 5, pp. 1–10, 2017.

[114] M. C. Wapler, J. Leupold, I. Dragonu, D. Von Elverfeld, M. Zaitsev, and U. Wallrabe, "Magnetic properties of materials for MR engineering, micro-MR and beyond," *Journal of Magnetic Resonance*, vol. 242, pp. 233–242, 2014.

[115] L. J. Azevedo, "Magnetic susceptibility of Stycast 1266 epoxy," *Review of Scientific Instruments*, vol. 54, no. 12, p. 1793, 1983.

Appendix A

Copyright agreements

A.1   Images used in Fig. 1.1

A.1.1   Figure 1.1a)

Title: Staccoto_Lightning
Source: https://commons.wikimedia.org/w/index.php?curid=37874129
Author: Griffinstorm
Licence: CC BY-SA 4.0

A.1.2   Figure 1.1b)

Title: 20150302_304prominence
Source: https://www.nasa.gov/content/goddard/sdo/pretty-prominence
Author: NASA/SDO
Licence: https://www.nasa.gov/multimedia/guidelines/index.html

A.2   Image used in Fig. 2.6a)

Title: Frog diamagnetic levitation
Source: https://commons.wikimedia.org/wiki/File:Frog_diamagnetic_levitation.jpg
Author: Lijnis Nelemans
Licence: CC-BY-SA-3.0

A.3   Image used in Fig. 6.1

A.3.1   Figure 6.1a)

Title: Honey
Source: https://commons.wikimedia.org/wiki/File:Runny_hunny.jpg
Author: Scott Bauer, USDA ARS (Agricultural Research Service, the research agency of the United States Department of Agriculture)
Licence: Public Domain

A.3.2   Figure 6.1b)

Title: Toothpasteonbrush
Source: https://en.wikipedia.org/wiki/Toothpaste#/media/File:Toothpasteonbrush.jpg
Author: Thegreenj
Licence: CC BY-SA 3.0

Appendix B

Journal publication 1

Status: Manuscript

Authors: Jennifer Dodoo, Glen McHale, and Adam A. Stokes

Title: Shaping of sessile magnetic drops due to electromagnetic stress

Declaration: This publication is jointly authored by myself, Glen McHale and Adam A. Stokes. I was responsible for the experimental and analytical work and the interpretation of the results. I was responsible for the writing and prepared all figures. Glen McHale contributed to discussions, and provided suggestions to the manuscript. Adam A. Stokes provided project supervision and suggestions to the manuscript.

Permission: Reproduced from Jennifer Dodoo, Glen McHale, and Adam A. Stokes, Shaping of sessile magnetic drops due to electromagnetic stress, arXiv:1908.05193.

Shaping of sessile magnetic drops due to electromagnetic stress

Jennifer Dodoo, and Adam A. Stokes*
School of Engineering, Institute for Micro and Nano Systems,
The University of Edinburgh, Edinburgh, EH9 3LJ

Glen McHale
Smart Materials & Surfaces Laboratory, Faculty of Engineering and Environment,
Northumbria University, Newcastle upon Tyne, NE1 8ST
(Dated: August 15, 2019)

While electric fields have been widely studied for drop shaping and digital microfluidics, a unified electromagnetic approach inclusive of magnetic fields is by far less known. Here using the electromagnetic stress tensor, we derive the stress acting on a droplet and test the results experimentally by measuring the shape of a paramagnetic drop in a magnetic field. We show through a simple transformation that our model can be applied to shaping of droplets by electric fields, thus giving a holistic description of the electromagnetic stresses acting on drops. This provides a blueprint for controlled shaping of sessile magnetic drops and has application to magnetic technologies in displays, liquid lenses, and chemical mixing of drops in microfluidics.

Controlled shaping of small volumes of fluids (or drops) is a key ingredient for liquid lenses to set optical properties [1], and for digital microfluidics (DMF) [2–4], where drops are, for example, manipulated for chemical mixing [5]. Drops can be shaped through the application of electromagnetic fields which exert a force on ions, and electric and magnetic dipoles in the drop. These forces can be calculated using the electromagnetic stress tensor, which is a powerful tool derived from first principles of electromagnetism and thermodynamics [6], and generally depends on: the thermodynamic potential of the system; the electric permittivity; the magnetic susceptibility; and the electromagnetic field applied. The electromagnetic stress tensor in vacuum (Maxwell stress tensor) has succesfully been applied to electrowetting - a technique where surface energies of the substrate are electrostatically modified - and dielectrophoresis, where a non-uniform electric field is applied to electric dipoles [7–10]. In contrast to the Maxwell stress tensor, which contains no information about the thermodyamic potential of the system, the full electromagnetic stress tensor, which contains this information, is generally not explicitly applied and evaluated, leading to common misconceptions about the model's range of validity [6].

Electrowetting is the most commonly used technique in DMF, but requires contact between the electrodes and the drop [2]. More recently, liquid dielectrophoresis, a contact-free bulk effect, is explored for DMF and liquid optics [10, 11] and has been successfully implemented for DMF manipulations [12]. Magnetic actuation techniques stand in contrast to electric actuation techniques, which dominate the DMF literature [4]. They open a range of new applications: magnetic fields are not as easily shielded as electric fields, making them suitable for applications in vivo or in environments that are sensitive to electric fields.

Magnetic techniques require the presence of magnetic dipoles and include: liquid marbles created using magnetic particles to enclose the drop; the actuation of fluids through the deformation of magnetic substrates; or the actuation of magnetic particle suspensions, such as ferrofluids [13, 14]. Ferrofluids are commonly used, because their high magnetic susceptibility values ($\chi > 10,000$) mean they can be actuated at low field strength. The application of magnetic fields pulls suspended particles into high-density regions, introducing an asymmetry in concentration that needs to be addressed in any formal treatment of ferrofluids. Paramagnetic salt solutions have a much smaller χ ($<< 1$) than ferrofluids, adding the benefit of uniformly distributed magnetic particles, even on application of a magnetic field. This alternative 'particle-free' actuation method has been demonstrated on superhydrophobic surfaces and a strong correlation between χ and ease of actuation has been shown [15, 16].

Here, we explicitly apply the electromagnetic stress tensor to a sessile drop in a magnetic field and derive a relationship for the change in drop shape as a function of applied magnetic field. We validate this relationship experimentally by measuring the change in shape of a paramagnetic sessile drop on a hydrophobic substrate in a homogeneous magnetic field. Our results highlight the fundamental symmetry in the shaping of drops with electric and magnetic fields.

The equilibrium shape of a sessile drop is determined by the stresses acting on it; these may include but are not limited to interfacial, gravitational and electromagnetic stress. To derive an expression for the shape of a sessile drop, we follow an analogous method to the one presented by Stierstadt and Liu [6] and use their definition of the full electromagnetic stress tensor which is universally valid for time-independent (quasi-static) non-dissipative processes:

$$\sigma_{ik} = (U - TS - \xi_\alpha\rho_\alpha - \mathbf{E}\cdot\mathbf{D} - \mathbf{H}\cdot\mathbf{B})\delta_{ik} + \mathrm{E_iD_k} + \mathrm{H_iB_k} \quad (1)$$

where i is the direction of force and k is the direction normal to the surface to which the force is applied, U is the total energy density of matter and field ($\mathrm{Jm^{-3}}$), T is temperature (K), S is the entropy of matter and field ($\mathrm{Jm^{-3}K^{-1}}$), ξ_α is the mass density of the chemical potential ($\mathrm{J\ kg^{-1}}$) of the material component α, ρ_α is the partial density of the material component α (the total density is $\rho^{tot} = \Sigma_\alpha\rho_\alpha$), $\mathbf{E}$ is the electric field strength, $\mathbf{D}$ is the electrical displacement, $\mathbf{H}$ is the auxiliary field, $\mathbf{B}$ is the magnetic flux density, and δ_{ik} is the Kronecker-Delta function.

In this work, we assume that there are no electric fields acting on the drop ($\mathbf{D}=\mathbf{E}=0$) and that the magnetic susceptibility is independent of the applied magnetic field strength ($\mathbf{B} = \mu\mathbf{H} = \mu_0(1+\chi)\mathbf{H}$ and $\mathbf{M} = \chi\mathbf{H}$). We limit this analysis to a closed thermodynamic system at constant temperature and volume, which is suitably described by the Helmholtz potential ($\mathrm{U = a^t + TS}$). The thermodynamic potential can be separated into field-independent ($\mathrm{a_0}$) and field-dependent ($\mathrm{a_{em}}$) terms: $\mathrm{a^t = a_0 + a_{em}}$, with $\mathrm{a_{em}} = \int \mathbf{H}\cdot\mathbf{dB}$.

The definition of the mass density of the chemical potential is: $\xi_\alpha = \delta\mathrm{a^t}/\delta\rho_\alpha$ [6]. In equilibrium, the stresses on the boundary of the two substances from inside and outside must be equal. The vapour phase is air, which we approximate as vacuum in its magnetic properties ($\mu = \mu_0$) as well as in its chemical potential ($\xi_\alpha\rho_\alpha = 0$). We impose the standard boundary conditions for Maxwell's equations as formulated by Stierstadt and Liu [6]: (1) the difference in the magnetic field component tangential to the surface must vanish ($\Delta \mathrm{B_t} = \Delta \mathrm{H_t} = 0$); (2) the stress components normal to the interface, σ_{nn}, must be continuous, while tangential components cancel. The electromagnetic stress difference across the air-liquid boundary then becomes:

$$\Delta\sigma_{nn}^{EM} = a_0^l - a_0^v - \xi_0\rho_\alpha - \frac{\mu_0}{2}H^2\left(\chi + \rho_\alpha\frac{\delta\chi}{\delta\rho_\alpha}\right) + \mu_0\chi H_n^2 \quad (2)$$

The magnetic flux density is the vector sum of its normal and tangential components with respect to the surface over which $\Delta\sigma_{nn}^{EM}$ is resolved, $\mathrm{H^2 = H_n^2 + H_t^2}$. We calculate the chemical potential using the Clausius-Mossotti approach: $\rho(\delta\chi/\delta\rho) = \chi(1 + \chi/3) \approx \chi$ for one-component fluids with $\chi << 1$.

$$\Delta\sigma_{nn}^{EM} = a_0^l - a_0^v - \xi_0\rho + \frac{\chi}{\mu_0}\left(B_n^2 - B^2\right) \quad (3)$$

where B is the magnetic flux density in air (T). In addition to the electromagnetic stress difference, the shape of the drop is also determined by the stress differences due to gravity and surface tension:

$$\Delta\sigma_{nn}^{surf} = \gamma(R_1^{-1} + R_2^{-1}) \quad (4)$$
$$\Delta\sigma_{nn}^{grav} = g\Delta\rho z \quad (5)$$

where γ is the surface tension ($\mathrm{Nm^{-1}}$), R_1 and R_2 are the principle radii of curvature of the drop outline (m), g is the gravitational acceleration ($\mathrm{ms^{-2}}$), ρ is the mass density ($\mathrm{kgm^{-3}}$), and z is the vertical distance to the apex point (m), as indicated by Fig. 1 [6, 17]. The principle radii of curvature of an axisymmetric drop can be expressed as:

$$(R_1^{-1} + R_2^{-1}) = \frac{r''}{(1 + r'^2)^{3/2}} - \frac{1}{r(1 + r'^2)^{1/2}} \quad (6)$$

where r(z) is the drop outline, originating from the apex point, r' and r'' are the first and second derivatives of r with respect to z, and r(z) and r' vanish at the apex point where z=0 [18]. In equilibrium, the stresses on the drop must sum up to zero.

$$0 = \Delta\sigma_{nn}^{surf} + \Delta\sigma_{nn}^{grav} + \Delta\sigma_{nn}^{EM} \quad (7)$$

Eq. (7) is an augmented Young-Laplace equation, which describes the hydrostatic and magnetic stresses on a sessile magnetic drop in air due to a magnetic field. Note that the definition of the magnetic stress in Eq. (2) holds for ferrofluids and para- and diamagnetic salt solutions and is valid in any time-independent (static) magnetic field. For axisymmetric drops, the radius of curvature at the apex point, b, depends on the difference of the energy densities of the Helmholtz potential of the liquid and vapour phase, $2\gamma\mathrm{b^{-1}} = \mathrm{a_0^l} - \mathrm{a_0^v}$ [6]. In the absence of magnetic fields, $\mathbf{B}=\mathbf{H}=0$, the stress balance of the drop simplifies to $0 = (R_1^{-1} + R_2^{-1}) + 2\mathrm{b^{-1}} + (\mathrm{g}\Delta\rho\gamma^{-1})z$, which is the well-known Young-Laplace equation [17–19]. Eq. (2) can be applied to static electric fields through a simple transformation of $\mathbf{H} \rightarrow \mathbf{E}$, $\mu_0 \rightarrow \epsilon_0$ and $\chi \rightarrow \chi_e$ (electric susceptibility), due to the symmetric and additive nature of the electromagnetic stress tensor with regards to electric and magnetic contributions [6]. Using this transformation on Eq. (2) we obtain the electric stress difference across the air-liquid boundary: $\Delta\sigma_{nn}^{EM} = 2\gamma\mathrm{b^{-1}} - \xi_0\rho_\alpha - 1/2\epsilon_0\mathrm{E^2}(\chi_e + \rho_\alpha(\delta\chi_e)(\delta\rho_\alpha)^{-1}) + \epsilon_0\chi_e\mathrm{E_n^2}$, which is similar to the electric stress used in literature [20], but includes the effect of changes in the distribution of the electromagnetic dipoles in the drop due to the applied electric field.

To test the validity of Eq. (7), we experimentally investigate the shape of paramagnetic drops in a homogeneous magnetic field directed along the symmetry axis of the drop (Fig. 1). We use a C-frame adjustable electromagnet containing iron cores with tips of 8 mm diameter. The substrates are 1 mm thick microscope glass slides coated with superhydrophobic composite films from colloidal graphite [21]. To measure over a wide range of total magnetic moments ($\mathrm{J} = \chi\mathrm{VB}\mu_0^{-1}$), we apply fields of 0 to 0.6 T; use drop volumes of 40-100 μl; and use three different aqueous paramagnetic salt solutions: (1) 35.6% ppw ($\chi = 2.55 \times 10^{-5}$) and (2) 17.8% ppw ($\chi = 1.24 \times 10^{-5}$)

manganese chloride tetrahydrate ($MnCl_2 \cdot 4H_2O$) and (3) 51 % ppw ($\chi = 4.17 \times 10^{-5}$) gadolinium chloride hexahydrate ($GdCl_3 \cdot 6H_2O$) [22].

To analyse the shape of the drop, we developed an algorithm similar to the standard Axisymmetric Drop Shape Analysis [23]: by imaging the side-profile of the drop using a digital DSLR-camera and using computational image analysis, we determine the drop outline $r(z)$; we solve Eq. (7) numerically for $r(z)$, using the Runge-Kutta method; and iteratively fit the solution of Eq. (7) using a standard least-square method (Levenberg-Marquardt) to the left and right-side of the drop outline independently.

To obtain good fits of Eq. (7) to $r(z)$ of (1) the drop in the absence of magnetic fields: we estimate the density of the solutions ρ to be equal to the density of water ($\rho_w = 997$ kgm^{-3}) and 1.1 times the density of water for the $MnCl_2$ and $GdCl_3$ solutions respectively and allow γ to freely change; and (2) the drop in the presence of magnetic fields: we allow $\xi_0 \rho_\alpha$ to freely change. This numerical optimization of physical values allows us to account for errors in our estimates of (1) the surface tension and density of the drop; and (2) the value of the field-independent chemical potential and the value of the difference of the field-independent thermodynamic potentials of liquid and vapour phase ($a_0^l - a_0^v$). The uncertainty on the $a_0^l - a_0^v$ value is caused by a non-axisymmetric deformation of the drop, due to systematic errors such as inhomogeneties in the applied field and in the roughness of the substrate, and the coarseness of the manual levelling of the substrate and magnet. (Without a numerical optimization of $\xi_0 \rho_\alpha$ (set to zero) we achieve less consistently good fits.) To measure the radius of curvature at the apex point, we fit a parabolic function to $r(z)$ in the range where Eq. (7) vanishes. We measure the contact angles of the left and right side of the drop independently by fitting second-order polynomials to the outline of the drop close to the triple contact line.

An example result of this methodology is presented by Fig. 1. The side-profile photographs of a 60 μl drop of the aqueous 51.4% ppw $GdCl_3$ solution presented by Fig. 1(a) show a visible elongation of the drop along the field lines. The numerical solutions of Eq. (7) run smoothly along the outline as shown by Fig. 1(b), with the optimized numerical value $\gamma = 66.7$ mNm^{-1}. The optimized surface tension is $\approx 8\%$ smaller than that of water (72.8 mNm^{-1}), accounting errors in the initial guesses of the numerical values of density and surface tension. Over the range of investigated salt concentrations, the optimized surface tension values are (71.3$\pm$0.3(SE)) mNm^{-1}, (72.3$\pm$0.1(SE)) mNm^{-1}, and (69.8$\pm$0.5(SE)) mNm^{-1} for the 35.6% ppw $MnCl_2$, 17.8% ppw $MnCl_2$, and 51.4% ppw $GdCl_3$ solutions respectively and the field-independent chemical potential varies, independently of salt concentration, between

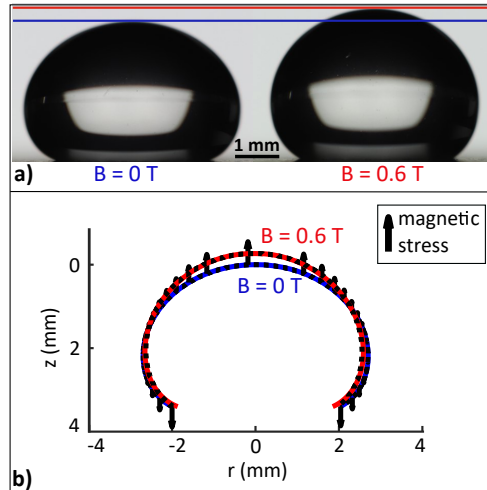FIG. 1. **(a)** Images of a 60 μl drop of an aqueous solution with 51.4% ppw $GdCl_3$ in the absence and in the presence of a magnetic field. The drop is elongated along the direction of the field lines. **(b)** The outlines (black dashed) of the drop in (a), and the corresponding numerical solutions of Eq. (7) with a parabolic fit in the region around the apex point where the numerical solution collapses. The black arrows show the variation of the relative magnitude of the magnetic stress along the outline of the drop.

-(1.6$\pm$0.2(SE))$\times 10^{-3}$ Jkg^{-1}.

Also presented by Fig. 1(b) is the magnetic stress acting on the outline of the drop. We observe that the stress is directed outwards from the drop along the magnetic field lines and its magnitude is proportional to the normal component of the magnetic flux density B_n^2. The magnetic stress is largest at the apex point, where the surface normal of the drop is parallel to the magnetic field lines, and diminishes at the outermost sides of the drop, before increasing again. At the solid-liquid interface, the surface vector of the drop is also parallel to the magnetic field lines, resulting in a magnetic stress and subsequent elongation of the drop towards the solid substrate which has not been studied here. This effect can be observed when suspending the droplet in a non-magnetizable medium [24]. Our investigation demonstrates the axisymmetric deformation of a paramagnetic drop through the application of a magnetic field that is axisymmetric with respect to the drop. A field that is not axisymmetric with respect to the drop, would cause a deformation towards the region of higher magnetic flux density.

Fig. 2 shows the change in characteristic geometric parameters of the drop presented by Fig. 1. As the
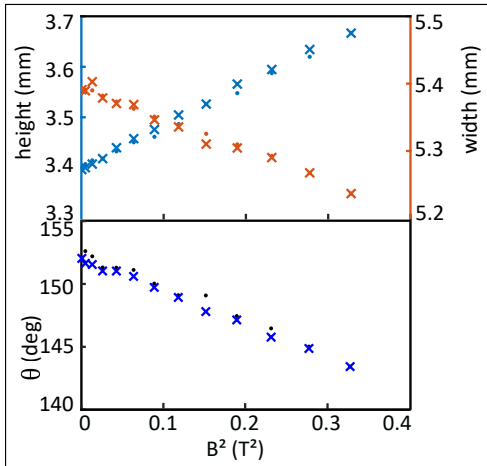
FIG. 2. Characteristic parameters of the shape of the drop presented by Fig. 1 as a function of the increasing (dots) and decreasing (x) applied field. (a) The height increases and the width decreases linearly with the square of the applied field. (b) The contact angle (θ) decreases linearly with the square of the applied field.

FIG. 3. The change in height (Δh) between 0 and 0.5 T applied field (B) of drops with different total magnetic moments (J). The change in height increases with total magnetic moment ($J = \chi V B \mu_0^{-1}$) of a drop with volume V and magnetic susceptibility χ. The three different markers represent the three salt solutions: 35.6% ppw MnCl$_2$ (crosses), 17.8% ppw MnCl$_2$ (circles), and 51.4% ppw GdCl$_3$ (dots) with $\chi = 2.55 \times 10^{-5}$, $\chi = 1.24 \times 10^{-5}$, and $\chi = 4.17 \times 10^{-5}$ respectively.

drop elongates along the field lines, the height increases from 3.4 to 3.7 mm, the width decreases from 5.39 to 5.24 mm, and the contact angle decreases from 152° to 143° between 0 T and 0.6 T applied field. The changes in height, width and contact angle are linear with B^2. The noise on the measurements originates from physical sources (vibrations induced in the drop from the laboratory environment), and from the grayscale to binary image conversion which introduces a random error caused by the background light and the pixel resolution of the camera. There is a small amount of hysteresis visible in the results shown by Fig. 2, which originates from the substrate properties (hysteresis in receding and advancing movement of the triple contact line). The deformation is fully reversible as long as the volume of the drop remains constant for the duration of the measurement.

Fig. 3 shows the change in height in the absence and presence of magnetic fields (B=0.5 T), of drops with a range of concentrations and volumes. The change in height increases with the drops total magnetic moment. Due to the linear relation between applied and induced field, the total magnetic moment of the drop increases proportionally with applied field. The proportionality constant between the total magnetic moment per unit volume and the applied field is the magnetic susceptibility. This result clearly illustrates the underlying electromagnetic theory presented in Eq. 1,
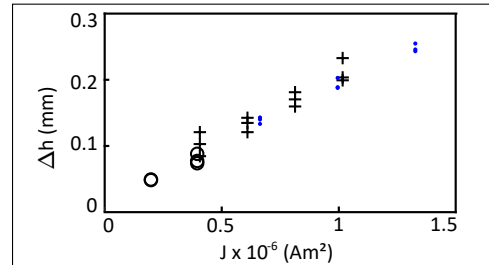
where the stress acting on the drop, and therefore the shape of the drop, is directly dependent on the exchange of momentum between matter and electromagnetic fields.

In conclusion, we have derived an expression for the shape of a magnetic drop in a magnetic field and validated this expression experimentally by analysing the shape of a paramagnetic drop in a homogeneous magnetic field. We have highlighted with this work that the fundamental symmetry of electric and magnetic phenomena in the electromagnetic stress tensor carries through to practical applications such as shape control of drops. This insight opens a whole range of applications to magnetic phenomena, such as display technologies, liquid lenses, and chemical mixing of drops in microfluidics.

* corresponding author: adam.stokes@ed.ac.uk

[1] K. Mishra, D. van den Ende, and F. Mugele, Micromachines **7** (2016), 10.3390/mi7060102.

[2] M. J. Jebrail and A. R. Wheeler, Current Opinion in Chemical Biology **14**, 574 (2010).

[3] R. Seemann, M. Brinkmann, T. Pfohl, and S. Herminghaus, Reports on Progress in Physics **75**, 016601 (2011).

[4] E. Samiei, M. Tabrizian, and M. Hoorfar, Lab on a Chip **16**, 2376 (2016).

[5] G. Chen, B. Ji, Y. Gao, C. Wang, J. Wu, B. Zhou, and W. Wen, Sensors and Actuators, B: Chemical **286**, 181 (2019).

[6] K. Stierstadt and M. Liu, ZAMM Zeitschrift fur Angewandte Mathematik und Mechanik **95**, 4

[7] F. Mugele and J.-C. Baret, Journal of Physics: Condensed Matter **17**, R705 (2005).

[8] T. B. Jones, J. D. Fowler, Y. S. Chang, and C. J. Kim, Langmuir **19**, 7646 (2003).

[9] K. H. Kang, Langmuir **18**, 10318 (2002).

[10] G. McHale, C. V. Brown, M. I. Newton, G. G. Wells, and N. Sampara, Physical Review Letters **107**, 1 (2011).

[11] C. V. Brown, G. G. Wells, M. I. Newton, and G. McHale, Nature Photonics **3**, 403 (2009).

[12] H. Geng, J. Feng, L. M. Stabryla, and S. K. Cho, Lab on a Chip **17**, 1060 (2017).

[13] Y. Zhang and N.-T. Nguyen, Lab Chip **17**, 994 (2017).

[14] N. Pamme, Lab Chip **6**, 24 (2006).

[15] A. Egatz-Gómez, S. Melle, A. A. García, S. A. Lindsay, M. Márquez, P. Domínguez-García, M. A. Rubio, S. T. Picraux, J. L. Taraci, T. Clement, D. Yang, M. A. Hayes, and D. Gust, Applied Physics Letters **89** (2006), 10.1063/1.2227517.

[16] L. Mats, F. Logue, and R. D. Oleschuk, Analytical Chemistry **88**, 9486 (2016).

[17] C. A. Miller and P. Neogi, *Interfacial phenomena : equilibrium and dynamic effects*, 2nd ed., Surfactant science series ; v. 139 (CRC Press, London, 2008) pp. 1–29.

[18] V. A. Lubarda and K. A. Talke, Langmuir **27**, 10705 (2011).

[19] A. W. Adamson, *Physical chemistry of surfaces*, fifth edit ed. (New York : John Wiley & Sons, Inc., New York, 1990).

[20] L. T. Corson, C. Tsakonas, B. R. Duffy, N. J. Mottram, I. C. Sage, C. V. Brown, and S. K. Wilson, Physics of Fluids **26**, 122106 (2014).

[21] I. S. Bayer, V. Caramia, D. Fragouli, F. Spano, R. Cingolani, and A. Athanassiou, Journal of Materials Chemistry **22**, 2057 (2012).

[22] We calculate χ for the salt solution using: $\chi = (\chi_s^m C_s M_s^{-1} + \chi_w^m (1 - C_s) M_w^{-1})\rho$, where $M_s = 197.9 \times 10^{-3}$ kg mol^{-1} for MnCl$_2$, and $M_s = 371.7 \times 10^{-3}$ kg mol^{-1} for GdCl$_3$, and $M_w = 18.02 \times 10^{-3}$ kg mol^{-1} are the molecular masses, and $\chi_s^m = 14350 \times 10^{-12}$ m^{3}mol^{-1} for MnCl$_2$, and $\chi_s^m = 27930 \times 10^{-12}$ m^{3}mol^{-1} for GdCl$_3$, and $\chi_w^m = -12.63 \times 10^{-12}$ m^{3}mol^{-1} are the literature values for the molar magnetic susceptibilities of the paramagnetic salts and water respectively [25]. C_s and ρ are the weight concentration of the salt in the solution and the density of the solution respectively.

[23] S. M. Saad and A. W. Neumann, Advances in Colloid and Interface Science **238**, 62 (2016).

[24] S. Afkhami, A. J. Tyler, Y. Renardy, M. Renardy, T. G. St. Pierre, R. C. Woodward, and J. S. Riffle, Journal of Fluid Mechanics **663**, 358 (2010).

[25] J. R. Rumble, in *CRC Handbook of Chemistry and Physics, 99th Edition (Internet Version 2018)* (CRC Press/Taylor & Francis, Boca Raton, FL).

Appendix C

Journal publication 2

Journal: Biomicrofluidics

Status: accepted for publication

Authors: Jennifer Dodoo and Adam A. Stokes

Title: Shaping and transporting diamagnetic sessile drops

Declaration: This journal publication is jointly authored by myself and Adam A. Stokes. I was responsible for the experimental and analytical work and the interpretation of the results. I was responsible for the writing and prepared all figures. Adam A. Stokes provided project supervision and suggestions to the manuscript.

Permission: Reproduced from Jennifer Dodoo and Adam A. Stokes, Shaping and transporting diamagnetic sessile drops, *Biomicrofluidics*, vol. 13, pp. 064110-1-064110-6, 2019., with the permission of AIP Publishing.

Biomicrofluidics

Shaping and transporting diamagnetic sessile drops

Jennifer Dodoo (iD), and Adam A. Stokes (iD)

View Online   Export Citation   CrossMark

Shaping and transporting diamagnetic sessile drops

View Online   Export Citation   CrossMark
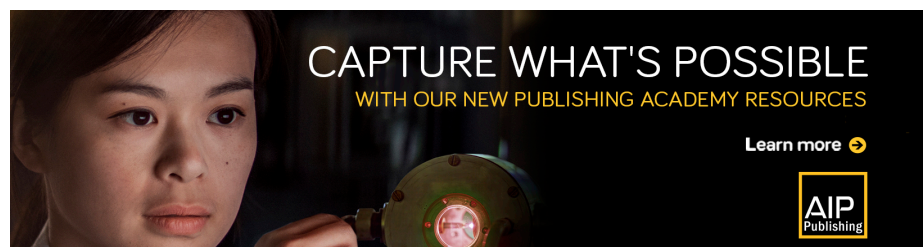
Jennifer Dodoo [iD] and Adam A. Stokes[a)] [iD]

AFFILIATIONS

School of Engineering, Institute for Integrated Micro and Nano Systems, The University of Edinburgh, Edinburgh EH9 3LJ,
United Kingdom

Note: This article is part of the special topic, Festschrift for Professor Hsueh-Chia Chang.
[a)]**Author to whom correspondence should be addressed:** adam.stokes@ed.ac.uk

ABSTRACT

Electromagnetic fields are commonly used to control small quantities of fluids in microfluidics and digital microfluidics. Magnetic control techniques are less well studied than their electric counterparts, with only a few investigations into liquid diamagnetism. The ratio of magnetic to surface energy (magnetic Bond number B_m) is an order of magnitude smaller for diamagnetic drops ($B_m \approx -0.3$ at 1.2 T applied field) than for paramagnetic drops ($B_m \approx 9.0$ at 1.2 T applied field). This weaker interaction between the magnetic field and the diamagnetic drop has led to the phenomenon being overlooked in digital microfluidics. Here, we investigate shaping and transport of diamagnetic drops using magnetostatic fields. Our findings highlight how diamagnetic fluids can be used as a novel tool in the toolbox of microfluidics and digital microfluidics.

I. INTRODUCTION

The control of small quantities of fluids is important in microfluidics[1] and digital microfluidics (DMF),[2–4] where drops are manipulated. DMF has strong biomedical applications, such as proteomics, imunoassays, and the study of cells.[5–7] While the electromagnetic control of fluids, particularly for biomedical applications, is dominated by electric phenomena, research into magnetic phenomena is much less common and their capabilities have not been fully realized. Magnetic actuation techniques are highly suitable for biomedical applications due to the biocompatibility of many magnetic fluids and the possibility to apply large magnetic fields to the human body—as routinely done in magnetic resonance imaging—where contrasting agents contain gadolinium chloride, a paramagnetic salt.

Electromagnetic fields exert forces on ions and electric and magnetic dipoles in the fluid. The potential of controlling fluids with electromagnetic fields has already been recognized in the late 19th century. Important examples include the works on bulk electrowetting by Lippmann[8]—where the interface between a mercury electrode and an electrolyte solution is shaped by an applied voltage; and on bulk dielectrophoresis by Pellat[9]—where the height-of-rise of a column of dielectric liquid (nonvolatile oil) is controlled by an alternating (at a frequency of 260 Hz) electric field, as illustrated in Fig. 1(a).

Electrowetting-on-dielectric (EWOD) includes a thin layer of dielectric between the electrode and the liquid to reduce the effects of electrolysis and was first introduced by Berge.[10] EWOD[11–13] and liquid dielectrophoresis[14–17] are common control techniques in DMF, where they are used for drop generation, transportation, splitting, and merging.[2–7]

Dielectrophoresis of suspended particles [see Fig. 1(b)] has found many biomedical applications,[18,19] including sorting of cells as demonstrated by Pohl.[20]

Liquid magnetophoresis—where fluids containing magnetic dipoles are manipulated by an applied magnetic field—has found wide ranging applications in magnetic DMF.[21,22] Drops of ferrofluids are commonly used in DMF,[21–23] and their shape in magnetic fields has been extensively studied.[24–26]

An alternative to ferrofluids are solutions of paramagnetic salts—which contain randomly oriented magnetic dipoles. Transportation of paramagnetic drops has first been reported by Egatz-Gomez *et al.*[27] and was studied more recently by Mats *et al.*[28] We have recently studied the shaping of paramagnetic drops in homogeneous magnetic fields and found an elongation of the drops along the field lines,[29] as illustrated in Fig. 1(c).

Magnetic fluids that are seldomly studied are diamagnetic liquids ($\chi^m < 0$), such as water or aqueous solutions of diamagnetic
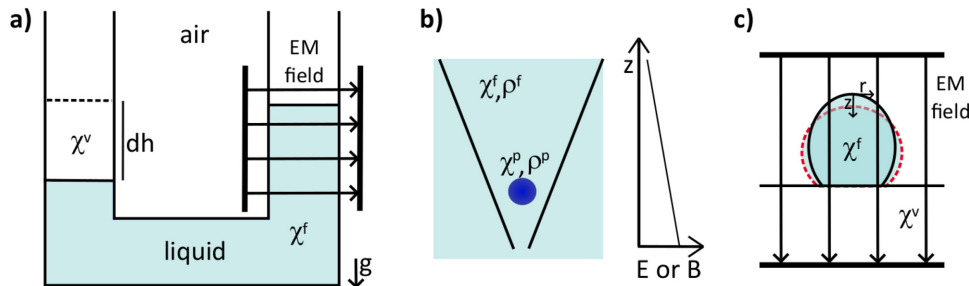
FIG. 1. Illustrations of common electrostatic and magnetostatic fluidic experiments. (a) The height of a liquid column in air is raised in an electric or a magnetic field, where the electric or magnetic susceptibility of the fluid is $\chi^f > 0$, and χ^v is the susceptibility of air. (b) A particle with magnetic susceptibility χ^p and density ρ^p is suspended in a liquid with χ^f and density ρ^f. In a nonuniform electrostatic or magnetostatic field, the electromagnetic force acting on the particle experiences depends on $\chi^p - \chi^f$. (c) A drop of a fluid with χ^f in air with χ^v in a uniform electrostatic or magnetostatic field is elongated for $\chi^f > 0$.

salts. A recent review by Bormashenko,[30] however, highlights the scientific interest and applications of bulk diamagnetism. In particular, recent publications on this topic include work on the magnetic deformation of diamagnetic liquid-air interfaces ("Moses effect")[31] and on floating diamagnetic bodies.[32,33] While these investigations were performed in bulk fluids, to the best of our knowledge, there are no studies on the shaping and control of diamagnetic drops.

In this work, we demonstrate and analyze the shaping of a diamagnetic drop in a homogeneous magnetic field. We find a reverse effect to the shaping of paramagnetic drops in homogeneous magnetic fields, namely, that diamagnetic drops shorten along the direction of the field lines. We also explore the transport of diamagnetic and paramagnetic drops due to magnetic field gradients. The capabilities of diamagnetic fluids have long been overlooked, and investigations into this field provide a wealth of opportunities for scientific studies and applications.

II. THEORETICAL BACKGROUND

The stress on a volume due to electromagnetic fields is captured in the Maxwell stress tensor (MST), which is valid in vacuum. The MST has been used to describe electrohydrodynamic and magnetohydrodynamic phenomena, such as dielectrophoresis[34–36] and electrowetting,[35,37] highlighting the frequency-dependence between electrowetting and DEP; and the deformation of ferrofluidic drops in magnetic fields.[25,38,39] The MST is a reduced version of the electromagnetic stress tensor (EMST), which is valid for quasistatic, nondissipative processes,[40]

$$\sigma_{ik} = (U - TS - \xi_\alpha \rho_\alpha - \mathbf{E} \cdot \mathbf{D} - \mathbf{H} \cdot \mathbf{B})\delta_{ik} + E_i D_k + H_i B_k, \quad (1)$$

where i is the direction of force, k is the direction normal to the surface to which the force is applied, U is the total energy density of matter and field ($\mathrm{J\,m^{-3}}$), T is the temperature (K), S is the entropy density of matter and field ($\mathrm{J\,m^{-3}\,K^{-1}}$), ξ_α is the mass density of the

chemical potential ($\mathrm{J\,kg^{-1}}$) of the material component α, ρ_α is the partial density of the material component α (the total density is $\rho^{tot} = \Sigma_\alpha \rho_\alpha$), $\mathbf{E}$ is the electric field, $\mathbf{D}$ is the electric displacement field, $\mathbf{H}$ is the applied (auxiliary) field, $\mathbf{B}$ is the magnetic flux density, and δ_{ik} is the Kronecker-Delta function.

Using Eq. (1), we have previously shown that, in a closed thermodynamic system with thermodynamic potential $a^t = a_0 + a_{em}$, where a_0 and a_{em} are field-independent and field-dependent terms, at constant temperature and volume ($U = a^t + TS$), in the absence of electric fields ($\mathbf{E}=\mathbf{D}=0$), and with $\xi_\alpha = \delta a^t/\delta\rho_\alpha$, the stress difference across a liquid-air boundary is[29]

$$\Delta\sigma_{nn}^M = a_0^l - a_0^v - \xi_0\rho_\alpha - \frac{1}{2}\mu_0 H^2\left(\chi + \rho_\alpha\frac{\delta\chi}{\delta\rho_\alpha}\right) + \mu_0\chi H_n^2. \quad (2)$$

The magnetic field is the vector sum of its normal and tangential components with respect to the surface over which $\Delta\sigma_{nn}^{EM}$ is resolved, $H^2 = H_n^2 + H_t^2$.

We can conclude from Eq. (2) that the magnetic stress difference depends on the shape of the interface and its orientation with respect to the applied magnetic field, as well as the magnetic properties of the liquid (χ); the direction of the magnetic stress is independent of the sign of the magnetic field but is instead determined by the sign of χ; and in a nonuniform magnetic field, the magnitude of $\Delta\sigma_{nn}^{EM}$ varies along the liquid-vapor interface, causing a stronger deformation of the interface in regions of higher magnetic field strength.

To determine the shape of a liquid-vapor interface, the electromagnetic stress needs to be balanced with other stresses such as gravitational and surface stress. Stierstadt and Liu[40] have used the EMST to find an expression for the height-of-rise of a liquid in a magnetic field and for the force on a particle in a fluid. We have previously used the EMST to describe the shape of sessile drops in magnetic fields.[29] The expressions for key parameters of these phenomena are summarized in Table I.

TABLE I. Expressions of key observables of some magnetostatic phenomena in fluids, derived using the electromagnetic stress tensor [Eq. (1)].[40]

Phenomenon	Characteristic expression
Change in height (Δh) of a liquid column in air[a]	$\Delta h = \mu_0 \chi_m (2\rho g)^{-1} H_t^2$ (3)
Force ($\mathbf{F}$) on a particle (p) of volume V_p in a fluid (f)[a]	$\mathbf{F} = \mu_0 (\chi_m^p - \chi_m^f) V_p \mathbf{H} \cdot \nabla \mathbf{H}$ (4)
Shape of a sessile drop in air[b]	$\gamma(R_1^{-1} + R_2^{-1}) = -g\Delta\rho z + a_0^l - a_0^v - \xi_0 \rho_\alpha + \mu_0 \chi (H_n^2 - H^2)$ (5)

[a]Adapted from Ref. 40.
[b]For an axisymmetric drop of a one-component fluid with $\chi \ll 1$, $\rho(\delta\chi/\delta\rho) = \chi(\chi/3 + 1) \approx \chi$, and $a_0^l - a_0^v = 2\gamma b^{-1}$, where γ is the surface tension (N m^{-1}) and b is the radius of curvature at the apex point (m) of the drop.[41–43] We use the following definition of the principle radii of curvature, R_1 and R_1, taken from Ref. 42: $(R_1^{-1} + R_2^{-1}) = r''(1 + r'^2)^{-3/2} - r(1 + r'^2)^{-1/2}$, where $r(z)$ is the drop outline, originating from the apex point, r' and r'' are the first and second derivatives of r with respect to z, respectively, and $r(z)$ and r' vanish at the apex point where $z = 0$.

The magnetic stress difference expressed in Eq. (2) can easily be transformed to an electric stress difference,[40]

$$
\begin{aligned}
\mathbf{H} &\rightarrow \mathbf{E}, \\
\mathbf{B} &\rightarrow \mathbf{D}, \\
\mu_0 &\rightarrow \epsilon_0, \\
\chi_m &\rightarrow \chi_e.
\end{aligned}
\tag{6}
$$

This means that the extensive body of work on electrostatic phenomena can be transferred to magnetostatic phenomena with some key differences: charge induced fluid circulations limit the validity of a static stress balance in dielectrics[44,45]—these circulations are not present in magnetic fluids;[46] natural materials may have a negative magnetic but not a negative electric susceptibility. These phenomenological differences make the study of magnetostatic phenomena particularly attractive. Here, we exploit the fact that diamagnetic fluids have a negative magnetic susceptibility to demonstrate the reverse effect to the elongation along the field lines of paramagnetic drops in uniform magnetostatic fields[29] and conducting drops in electrostatic fields.[47]

III. EXPERIMENTAL DEMONSTRATION: DEFORMATION AND TRANSPORT OF DIAMAGNETIC SESSILE DROPS

To confirm our predictions on the shape of diamagnetic drops from Sec. II, we (1) measure the shape of diamagnetic drops in a homogeneous magnetic field directed along the symmetry axis of the drops [Fig. 1(c)] and (2) demonstrate the transport of diamagnetic drops in a nonuniform magnetic field.

A. Experimental method

For the actuation of the magnetic drops, we use a C-frame adjustable electromagnet containing iron cores with tips of 8 mm diameter. The coils are connected in-series to a programmable power supply (72-2540, Digital-Control and Programmable DC Power Supply 30V 3A, Tenma). The magnetic field is approximately uniform over the width of the core tips, with a $\approx$20% reduction in field strength over a 10 mm distance to the center of the core tips at an air-gap of 7 mm. The substrates are microscope glass slides which we coated with superhydrophobic composite films from colloidal graphite.[49]

The drops are aqueous solutions of the diamagnetic salts: calcium bromide hydrate ($Br_2Ca \cdot xH_2O$, CAS-No.: 71626-99-8) and sodium sulfate ($NaSO_4$, CAS-No.: 7757-82-6). For the transport measurements, we also use the paramagnetic salt manganese chloride tetrahydrate ($MnCl_2 \cdot 4H_2O$, CAS-No.: 13446-34-9). The salts were sourced from Sigma-Aldrich (Sigma-Aldrich Company Ltd., U.K.) and their properties are summarized in Table II. The de-ionized water has a molecular weight of $M_w = 18.02$ g mol^{-1} and a molar magnetic susceptibility of $\chi_w^m = -12.63 \times 10^{-6}$ cm^3 mol^{-1}. To generalize the present study, we define the dimensionless magnetic bond number from the properties of the drop and applied field, which is the ratio of the magnetic to surface energy[50] of the

TABLE II. List of properties of the diamagnetic salts and their solutions used in this work.

Solution name	Salt formula	M_S (g mol^{-1})	χ_m[a] (cm^3 mol^{-1})	C_S (%ppw)	χ[b]	B_m at $B = 1.2$ T
Calcium bromide	$Br_2Ca \cdot xH_2O$	199.89	-73.8×10^{-6}	55.8	-7.8×10^{-6}	-0.3
Sodium sulfate	$NaSO_4$	142.04	-52×10^{-6}	15.7	-8.3×10^{-6}	-0.3
Manganese chloride	$MnCl_2 \cdot 4H_2O$	197.9	$14\,350 \times 10^{-6}$	27.4	245.0×10^{-6}	8.8

[a]Taken from Ref. 48.
[b]To calculate the magnetic susceptibility of the drop, we use $\chi = \rho(\chi_s^m C_s M_s^{-1} + \chi_w^m (1 - C_s)M_w^{-1})$, where M_s and M_w (g mol^{-1}) are the molar masses and χ_s^m (cm^3 mol^{-1}) and χ_w^m (cm^3 mol^{-1}) are the molar magnetic susceptibilities of the diamagnetic salt and water, respectively. C_s is the weight concentration of salt in the solution and ρ is the density of the solution. We assume that the densities of the salt solutions are 1.2, 1.0, and 1.0 times the density of water (990 g l^{-1}) for the CaBr$_2$, NaSO$_4$, and MnCl$_2$ solutions, respectively.

drops,

$$B_m = \frac{\chi B^2 V^{1/3}}{2\mu_0 \gamma}. \quad (7)$$

The values of B_m for each drop are listed in Table II.

We analyze the shape of the diamagnetic drop using the same methodology as used in Ref. 29 for paramagnetic drops: we image the side-profile of the drop using a digital DSLR-camera and determine the drop outline $r(z)$ using computational image analysis; using a standard least-square method (Levenberg-Marquardt), we iteratively fit the numerically solutions of Eq. (5) to the left and right sides of the drop outline independently. To account for the uncertainty in our estimates of the surface tension and density of the drops, we optimize the numerical value of the surface tension for each drop in the absence of magnetic fields. For drops in the presence of magnetic fields, we optimize the value of the field-independent chemical potential, which also accounts for small deviations of a nonaxisymmetric drop deformation, caused by inhomogeneities in the roughness of the substrates, manual leveling of the substrate and magnet, and manual positioning of the drop in the center of the magnetic field. To measure the radius of curvature at the apex point of the drop, we fit a parabolic function to $r(z)$ in the range where Eq. (5) vanishes. We measure the left and right contact angles of the drop by fitting second-order polynomials to the section of the outline close to the triple contact line.

We quantify the transport of a drop in a nonuniform magnetic field by measuring the translocation of the projection of the center-of-mass onto the substrate. We determine the position of the center-of-mass as the point along the symmetry axis of the drop that splits the drop into two regions with equal volume, assuming that the density of the drop is uniform.

B. Results: Shape of a diamagnetic drop

An example of a result of this methodology is shown in Fig. 2. A $100\,\mu l$ drop of the calcium bromide solution (see Table II) is imaged in the absence of a magnetic field [Fig. 2(a)]. The numerical

solution of Eq. (5) fits well to the outline of the drop. Upon application of a magnetic field, the drop is shortened along the direction of the field lines, as shown in Fig. 2(b), which shows an enlarged view of the outline of the drop at the apex point. The height and width of the drop as a function of applied magnetic field are presented in Fig. 2(c). As the applied field is increased from 0 to 1.2 T, the height reduces from 3.73 to 3.69 mm, and the width increases from 6.69 to 6.71 mm. The change in the shape is proportional to the square of the applied field.

We find this deformation to be repeatable and present the mean and standard error of a measurement set. We find a change in the height of $(-13 \pm 2)\,\mu m$ and $(-25 \pm 2)\,\mu m$ for $100\,\mu l$ drops of the calcium bromide and sodium sulfate solutions, respectively, when changing the applied field from 0 to 0.9 T. The contact angles of the drops in the absence of magnetic fields are $151.6° \pm 1°$ and $151.7° \pm 1°$ for the calcium bromide and sodium sulfate solutions, respectively, agreeing with the expected contact angle of water on these substrates.[49] Upon the application of 0.9 T, the contact angles of the drops increase to $152.2° \pm 1°$ and $152.2° \pm 1°$, respectively. The numerically optimized parameters of the calcium bromide and sodium sulfate solutions, respectively, are the surface tensions $(70.7 \pm 1)\,m\,N\,m^{-1}$ and $(73.5 \pm 1)\,m\,N\,m^{-1}$, values that are within two standard errors of the surface tension of water $(72.8\,m\,N\,m^{-1})$, and the field-independent chemical potential $(1.8 \pm 1) \times 10^{-4}\,J\,kg^{-1}$ and $(0.7 \pm 1) \times 10^{-4}\,J\,kg^{-1}$.

These results are in agreement with the predictions made in Sec. II, namely, that drops with a higher magnitude of magnetic susceptibility deform more strongly in a magnetic field, and that a negative susceptibility causes a magnetic stress directed into the liquid phase, leading to a shortening of the drop along the field lines.

C. Results: Transport measurements

Example results of the transport measurements of diamagnetic and paramagnetic drops in a nonuniform magnetic field are shown in Fig. 3. The magnetic field decays along the x axis from a maximum value of B_m as illustrated in Fig. 3(a). A $300\,\mu l$ drop of
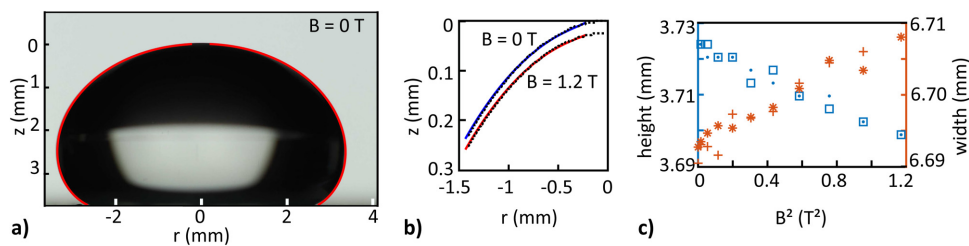

FIG. 2. Deformation of a $100\,\mu l$ drop of an aqueous solution of calcium bromide (see Table II). (a) The numerical solutions of Eq. (5) (blue) and image of the drop in the absence of a magnetic field. (b) Enlarged view of the outline close to the apex point (black, dashed) with the numerical solutions of Eq. (5) in the absence of a magnetic field (blue) and with 1.2 T applied field (red). (c) The height decreases (dots), while the width increases (asterisks) with the applied field. As the field is decreased, the height increases (squares) and the width decreases (crosses) to their initial values.
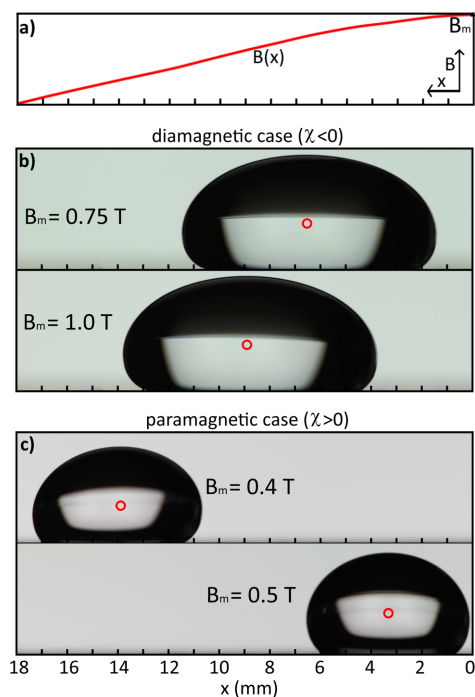
FIG. 3. Transport of dia- and paramagnetic drops in a nonuniform magnetic field. (a) Illustration of the profile of the magnetic field, which decays along the x axis from its maximum value B_m. As B_m is increased, a $300\,\mu l$ drop of sodium sulfate solution is pushed away from the region of the highest field strength (b), while a $100\,\mu l$ of manganese chloride is pulled toward the region of the highest field strength (c). The positions of the center-of-masses are indicated as red circles. The properties of the salt solutions are summarized in Table II.

the sodium sulfate solution is shown in Fig. 3(b) to lean away from the region of high magnetic flux density, where $B_m = 0.75\,T$. Upon increasing B_m, the drop is pushed over a distance of approximately 3 mm away from the region of highest magnetic flux density. In contrast to this diamagnetic drop being pushed out of the magnetic field, a drop of $100\,\mu l$ manganese chloride solution is shown in Fig. 3(c) to lean toward the region of highest magnetic flux density, where $B_m = 0.4\,T$. Upon increasing B_m, the drop is pulled over a distance of approximately 12 mm toward the region of the highest magnetic field strength.

We found the translocation of the center-of-mass in these experiments repeatable, with drops of $300\,\mu l$ sodium sulfate solution pushed over a distance of $(3.0 \pm 0.3)\,mm$ and the drops of $100\,\mu l$ manganese chloride solutions pulled over a distance of $(10.4 \pm 0.3)\,mm$.

Consistent with our predictions made in Sec. II, the transport direction is determined by the sign of χ, while the transport distance is determined by the value χ, the size of the drop, and the field gradient. Due to the field gradient, the drop deforms asymmetrically, causing it to lean into ($\chi > 0$) or out of ($\chi < 0$) the region of higher field strength. The static frictional forces between the substrate and the drop determine how much the drop leans before sliding.

Our results demonstrate that, though the stress acting on diamagnetic drops is several orders of magnitude smaller than that on paramagnetic drops, it is nevertheless sufficient to achieve transport even in a simple experimental design as we have employed here. Diamagnetic solutions enable the reversal of the transport direction, compared to paramagnetic solutions or ferrofluids, without the need to alter the actuation mechanism.

IV. SUMMARY AND CONCLUSION

In summary, we have used the EMST to describe the shape of diamagnetic drops in magnetic fields. We found a shortening of the drops along the direction of magnetic field lines, which stands in contrast to the elongation along the field lines of drops with a positive magnetic susceptibility, such as paramagnetic or ferrofluidic drops. The strength of the deformation scales with the total magnetic moment induced in the drop, which is proportional to the volume and magnetic susceptibility of the drop. We demonstrated that diamagnetic drops in nonuniform magnetic fields are transported away from the region of the highest magnetic field strength. This stands in contrast to the transport of paramagnetic drops, which is directed toward the region of highest magnetic field strength. Though the presented solutions have a too high osmolality to contain mammalian cells (2 osm/kg and 8 osm/kg for the sodium sulfate and calcium bromide solutions, respectively), further dilution and usage of stronger magnetic fields may permit suspension and transport of mammalian or plant cells. This technique may also be applied to suspension and transport of DNA or other macromolecules such as proteins.

In conclusion, our work demonstrates that the EMST captures the magnetic forces acting on fluids due to magnetostatic fields and electrostatic fields. This tool aids the study of bulk diamagnetism, and our findings highlight the natural place of diamagnetic fluids among the tools of microfluidics and DMF.

REFERENCES

[1]G. M. Whitesides, Nature **442**, 368 (2006).
[2]S.-Y. Teh, R. Lin, L.-H. Hung, and A. P. Lee, Lab Chip **8**, 198 (2008).
[3]R. Seemann, M. Brinkmann, T. Pfohl, and S. Herminghaus, Rep. Prog. Phys. **75**, 016601 (2012).
[4]K. Choi, A. H. Ng, R. Fobel, and A. R. Wheeler, Annu. Rev. Anal. Chem. **5**, 413 (2012).
[5]E. M. Miller and A. R. Wheeler, Anal. Bioanal. Chem. **393**, 419 (2009).
[6]M. J. Jebrail and A. R. Wheeler, Curr. Opin. Chem. Biol. **14**, 574 (2010).
[7]S. L. S. Freire, Sens. Actuators A **250**, 15 (2016).

[8]M. G. Lippmann, Ann. Chim. Phys. **5**, 494 (1875).

[9]H. Pellat, C. R. Hebd. Séances Acad. Sci. B **123**, 123 (1896).

[10]B. Berge, C. R. Acad. Sci. Paris II **317**, 157 (1993).

[11]S. K. Cho, H. Moon, and C. J. Kim, J. Microelectromech. Syst. **12**, 70 (2003).

[12]F. Mugele and J.-C. Baret, J. Phys.: Condens. Matter **17**, R705 (2005).

[13]W. C. Nelson and C. J. C. Kim, J. Adhes. Sci. Technol. **26**, 1747 (2012).

[14]T. B. Jones, J. Electrostat. **51–52**, 290 (2001).

[15]P. R. Gascoyne, J. V. Vykoukal, J. A. Schwartz, T. J. Anderson, D. M. Vykoukal, K. W. Current, C. McConaghy, F. F. Becker, and C. Andrews, Lab Chip **4**, 299 (2004).

[16]G. McHale, C. V. Brown, M. I. Newton, G. G. Wells, and N. Sampara, Phys. Rev. Lett. **107**, 186101 (2011).

[17]H. Geng, J. Feng, L. M. Stabryla, and S. K. Cho, Lab Chip **17**, 1060 (2017).

[18]R. Pethig, J. Electrochem. Soc. **164**, 3049 (2017).

[19]M. P. Hughes, Biomicrofluidics **10**, 032801 (2016).

[20]H. A. Pohl and I. Hawk, Science **152**, 647 (1966).

[21]N. Pamme, Lab Chip **6**, 24 (2006).

[22]Y. Zhang and N.-T. Nguyen, Lab Chip **17**, 994 (2017).

[23]M. Latikka, M. Backholm, J. V. Timonen, and R. H. Ras, Curr. Opinion Colloid Interface Sci. **36**, 118 (2018).

[24]O. E. Séro-Guillaume, D. Zouaoui, D. Bernardin, and J. P. Brancher, J. Fluid Mech. **241**, 215 (1992).

[25]S. Afkhami, A. J. Tyler, Y. Renardy, M. Renardy, T. G. St. Pierre, R. C. Woodward, and J. S. Riffle, J. Fluid Mech. **663**, 358 (2010).

[26]P. Rowghanian, C. D. Meinhart, and O. Campàs, J. Fluid Mech. **802**, 245 (2016).

[27]A. Egatz-Gómez, S. Melle, A. A. García, S. A. Lindsay, M. Márquez, P. Domínguez-García, M. A. Rubio, S. T. Picraux, J. L. Taraci, T. Clement, D. Yang, M. A. Hayes, and D. Gust, Appl. Phys. Lett. **89**, 034106 (2006).

[28]L. Mats, R. Young, G. T. T. Gibson, and R. D. Oleschuk, Sens. Actuators B **220**, 5 (2015).

[29]J. Dodoo, G. McHale, and A. A. Stokes, e-print arXiv:1908.0519 (2019).

[30]E. Bormashenko, Adv. Colloid Interface Sci. **269**, 1 (2019).

[31]D. Laumann, Phys. Teacher **56**, 352 (2018).

[32]M. Frenkel, V. Danchuk, V. Multanen, I. Legchenkova, Y. Bormashenko, O. Gendelman, and E. Bormashenko, Langmuir **34**, 6388 (2018).

[33]O. Gendelman, M. Frenkel, V. Fliagin, N. Ivanova, V. Danchuk, I. Legchenkova, A. Vilk, and E. Bormashenko, Surf. Innov. **7**, 194 (2019).

[34]F. Sauer and R. Schlogel, in *Interactions Between Electromagnetic Fields and Cells*, edited by A. Chiabrera, C. Nicolini, and H. P. Schwan (Plenum Publishing Corporation, 1985), pp. 203–251.

[35]T. B. Jones, Langmuir **18**, 4437 (2002).

[36]X. Wang, X.-B. Wang, and P. R. Gascoyne, J. Electrostat. **39**, 277 (1997).

[37]T. B. Jones, K. L. Wang, and D. J. Yao, Langmuir **20**, 2813 (2004).

[38]J. C. Bacri and D. Salin, J. Phys. Lett. **43**, 649 (1982).

[39]H. A. Stone, J. R. Lister, and M. P. Brenner, Proc. R. Soc. Lond. A **455**, 329 (1999).

[40]K. Stierstadt and M. Liu, Z. Angew. Math. Mech. **95**, 4 (2015).

[41]C. A. Miller and P. Neogi, "Interfacial phenomena: Equilibrium and dynamic effects," in *Surfactant Science Series*, 2nd ed. (CRC Press, London, 2008), Vol. 139, pp. 1–29.

[42]V. A. Lubarda and K. A. Talke, Langmuir **27**, 10705 (2011).

[43]A. W. Adamson, *Physical Chemistry of Surfaces*, 5th ed. (John Wiley & Sons, Inc., New York, 1990).

[44]G. I. Taylor, Proc. R. Soc. Lond. A **291**, 159 (1966).

[45]J. R. Melcher and G. I. Taylor, Annu. Rev. Fluid Mech. **1**, 111 (1969).

[46]J. D. Sherwood, J. Fluid Mech. **188**, 133 (1988).

[47]L. T. Corson, C. Tsakonas, B. R. Duffy, N. J. Mottram, I. C. Sage, C. V. Brown, and S. K. Wilson, Phys. Fluids **26**, 122106 (2014).

[48]J. R. Rumble, in *CRC Handbook of Chemistry and Physics*, 99th ed. (CRC Press/Taylor & Francis, Boca Raton, FL, 2018) (Internet Version).

[49]I. S. Bayer, V. Caramia, D. Fragouli, F. Spano, R. Cingolani, and A. Athanassiou, J. Mater. Chem. **22**, 2057 (2012).

[50]G. P. Zhu, N. T. Nguyen, R. V. Ramanujan, and X. Y. Huang, Langmuir **27**, 14834 (2011).